Article:

Bowyer, FT, Zhuravlev, AY, Wood, R et al. (7 more authors) (2022) Calibrating the temporal and spatial dynamics of the Ediacaran - Cambrian radiation of animals. Earth-Science Reviews, 225. 103913. ISSN 0012-8252

https://doi.org/10.1016/j.earscirev.2021.103913

Calibrating the temporal and spatial dynamics of the Ediacaran - Cambrian radiation of animals

Fred T. Bowyer[1,2]*, Andrey Yu. Zhuravlev[3], Rachel Wood[2], Graham A. Shields[4], Ying Zhou[4], Andrew Curtis[2], Simon W. Poulton[1], Daniel J. Condon[5], Chuan Yang[5] and Maoyan Zhu[6,7]

[1]School of Earth and Environment, University of Leeds, Leeds LS2 9JT, UK.
[2]School of GeoSciences, University of Edinburgh, James Hutton Road, Edinburgh EH9 3FE, UK.
[3]Department of Biological Evolution, Faculty of Biology, Lomonosov Moscow State University Leninskie Gory 1(12), Moscow 119234, Russia.
[4]Department of Earth Sciences, University College London, Gower Street, London WC1E 6BT, UK.
[5]British Geological Survey, Keyworth, NG12 5GG, UK
[6]State Key Laboratory of Palaeobiology and Stratigraphy, Nanjing Institute of Geology and Palaeontology and Center for Excellence in Life and Palaeoenvironment, Chinese Academy of Sciences, Nanjing 210008, China.
[7]College of Earth and Planetary Sciences, University of Chinese Academy of Sciences, Beijing 10049, China.

*Corresponding author: Fred Bowyer (fred.bowyer@ed.ac.uk)

Abstract

The Ediacaran-Cambrian transition, which incorporates the radiation of animals, lacks a robust global temporal and spatial framework, resulting in major uncertainty in the evolutionary dynamics of this critical radiation and its relationship to changes in palaeoenvironmental geochemistry. We first present a new $\delta^{13}C_{carb}$ composite reference curve for the Ediacaran Nama Group of southern Namibia, and we then outline four new possible global age models (A to D) for the interval 551-517 million years ago (Ma). These models comprise composite carbonate-carbon isotope ($\delta^{13}C_{carb}$) curves, which are anchored to radiometric ages and consistent with strontium isotope chemostratigraphy, and are used to calibrate metazoan distribution in space and time. These models differ most prominently in the temporal position of the basal Cambrian negative $\delta^{13}C_{carb}$ excursion (BACE). Regions that host the most complete records show that the BACE nadir always predates the Ediacaran-Cambrian boundary as defined by the first appearance datum (FAD) of the ichnospecies *Treptichnus pedum.* Whilst treptichnid traces are present in the late Ediacaran fossil record, the FAD of the ichnospecies *T. pedum* appears to post-date the LAD of in situ *Cloudina* and *Namacalathus* in all environments with high-resolution $\delta^{13}C_{carb}$ data. Two age models (A and B) place the BACE within the Ediacaran, and yield an age of ~538.8 Ma for the Ediacaran-Cambrian boundary; however models C and D appear to be the most parsimonious and may support a recalibration of the boundary age by up to 3 Myr younger. All age models reveal a previously underappreciated degree of variability in the terminal Ediacaran, incorporating notable positive and negative excursions that precede the BACE. Nothwithstanding remaining uncertainties in chemostratigraphic correlation, all models support a pre-BACE first appearance of Cambrian-type shelly fossils in Siberia and possibly South China, and show that the Ediacaran-Cambrian transition was a protracted interval represented by a series of successive radiations.

The Ediacaran-Cambrian radiation occurred over a protracted interval without global mass extinctions and with generally diachronous metazoan appearances.

1. Introduction

The late Ediacaran to early Cambrian interval encompasses the Gaskiers glaciation (~580 Ma), the first appearance of complex macroscopic life (~575 Ma), mobile biota (≤560 Ma), skeletal metazoans (~550 Ma), and the origin of modern metazoan phyla (Wood et al., 2019). Understanding the temporal and spatial context of these events is currently limited due to the lack of high-resolution age models to allow correlation of key sections. The geological record throughout this interval also contains numerous unconformities and gaps of uncertain duration, a sparse global distribution of datable stratiform volcanic deposits, and diverse endemic biotas, resulting in loose chronostratigraphic and biostratigraphic control. As a result, no consistent global chronostratigraphic correlation exists, particularly for the critical late Ediacaran to lower Cambrian (Fortunian Stage) interval. Early metazoans evolved in a highly dynamic Earth system, and so without a high-resolution temporal and spatial framework we are unable to address many profound uncertainties, including the evolutionary dynamics of the Cambrian Explosion, the response of metazoans to local and global changes in oceanic redox conditions and nutrient availability, and whether one or more contemporaneous mass extinctions occurred.

The formal placement of the Ediacaran-Cambrian boundary in the Fortune Head section, Newfoundland, Canada, which is based on the first appearance datum (FAD) of *Treptichnus pedum* ichnospecies (Brasier et al., 1994), has been particularly problematic since it occurs in a section with few datable volcanics, sparse skeletal biota, and limited potential for chemostratigraphy (Babcock et al., 2014). Indeed, the choice of *T. pedum* as a marker fossil for the basal Cambrian has also been a source of contention given the strong environmental, lithological and facies dependency for preservation of this trace, resulting in a notable absence from carbonate-dominated successions (e.g. Babcock et al., 2014). A similar problem is encountered when attempting to define the basal Cambrian using the first appearance of 'Cambrian-type' small skeletal fossils, which are themselves absent or rare in siliciclastic-dominated successions, especially in environments that were not conducive to early phosphatization. To overcome this complication, a holistic integration of radiometric, chemostratigraphic and palaeontological data across this interval is crucial. At present, the age of the Ediacaran-Cambrian boundary is 541.0 ± 1.0 Ma (ICC 2021), however the radiometric age of a tuff deposit in the Nama Group, Namibia, on the Kalahari Craton, provides a current best estimate of 538.8 Ma for the maximum age of the first appearance of *T. pedum* (Linnemann et al., 2019; Xiao and Narbonne, 2020).

The carbon isotopic composition of marine carbonates ($\delta^{13}C_{carb}$) is most commonly considered to reflect secular changes in the ratio of ^{13}C to ^{12}C in seawater that are associated with changes in the relative export/burial rates of inorganic versus organic carbon (Kaufman et al., 1991; Keith and Weber, 1964; Veizer et al., 1980; Veizer and Hoefs, 1976). As a result, secular $\delta^{13}C_{carb}$ profiles have been used for regional and global correlation (Halverson et al., 2010; Macdonald et al., 2013; Maloof et al., 2010; Yang et al., n.d.; Zhu et al., 2007). However, a number of local effects have also been proposed that may partially decouple the local record of primary $\delta^{13}C_{carb}$ from the composition of dissolved inorganic carbon (DIC) in the open ocean. These include diurnal coupling between photosynthesis and carbonate saturation in shallow carbonate settings (Geyman and Maloof, 2019), local DIC pools of distinct isotopic composition (Cui et al., 2020b; Melim et al., 2002), and the possibility for water-column methanogenesis and carbonate recycling under low-sulfate conditions associated with restriction (Cui et al., 2020b). Additionally, facies-specific diagenetic regimes can yield distinct $\delta^{13}C_{carb}$ for time-equivalent sections in modern marine basins (Melim et al., 2002), and this has also been established in the Cryogenian interglacial ocean (Hoffman and Lamothe, 2019), and the Paleoproterozoic Lomagundi-Jatuli event (Prave et al., 2021). As a result, changes in $\delta^{13}C_{carb}$ may in fact archive contemporaneous pools of DIC from adjacent depositional settings with variable C isotope composition. The potential for both local water column DIC and the effects of carbonate diagenesis to result in significant deviation of $\delta^{13}C_{carb}$ from global seawater $\delta^{13}C$ may therefore be problematic when building $\delta^{13}C_{carb}$-based age frameworks.

Despite these potential complications, it is not clear why during certain intervals of geological history some depositional settings acquire $\delta^{13}C_{carb}$ values that deviate markedly from mean values (Hoffman and Lamothe, 2019). For example, integrated $\delta^{13}C_{carb}$, $\delta^{44}Ca$, $\delta^{26}Mg$ and sequence stratigraphic study of the Cryogenian interglacial Trezona $\delta^{13}C_{carb}$ excursion reveals that, whilst facies-specific trends in $\delta^{13}C_{carb}$ may correspond with fluid vs sediment buffered diagenesis, the excursion itself is of global significance and may correspond with global changes in siliciclastic vs carbonate sedimentation, nutrient delivery, and eustatic sea level (Ahm et al., 2021). Therefore, notwithstanding uncertainties in the driving mechansims for $\delta^{13}C_{carb}$ records and possible facies-related, diagenetic offsets, the secular trends represented by gradual unidirectional shifts in $\delta^{13}C_{carb}$ in multiple globally distributed and temporally equivalent open-marine sections may reflect changes to the carbon cycle that are of global significance, and hence are applicable for chemostratigraphic correlation.

To date, efforts to produce a global composite Ediacaran $\delta^{13}C_{carb}$ record (e.g. Macdonald et al., 2013; Yang et al., 2021) have revealed the middle Ediacaran Shuram negative anomaly at around <579 – >564 Ma (Rooney et al., 2020; Yang et al., 2021), followed by a positive shift from ca. 564-550 Ma. The sedimentary record from ca. 564-550 Ma is radiometrically well dated in Baltica (the East European Platform) (Yang et al., 2021) and Avalonia (Matthews et al., 2020; Noble et al., 2015); however, siliciclastic strata with poor $\delta^{13}C_{carb}$ resolution dominate these successions. A subsequent negative excursion with a recovery at ~550 Ma (Yang et al., 2021) is followed by a final late Ediacaran positive plateau (the EPIP, Zhu et al., 2017). This plateau appears to terminate with the onset of a globally widespread large magnitude (min $\delta^{13}C_{carb}$ of -10‰) negative excursion, termed '1n' in strata of the Siberian Platform, and in previous global compilations (Kouchinsky et al., 2007; Maloof et al., 2010). This excursion is considered to be approximately coincident with the Ediacaran-Cambrian boundary and has also previously been termed the 'Basal Cambrian negative $\delta^{13}C_{carb}$ excursion' (BACE); an acronym that is adopted herein. The age of the BACE is currently correlated with a radiometrically dated negative excursion in the A4 Member of the Ara Group, Oman at ~541 Ma (Bowring et al., 2007; Hodgin et al., 2020; Maloof et al., 2010; Smith et al., 2015). Possible mass extinctions have been suggested between the Ediacaran White Sea and Nama biotic assemblages, and again at the Ediacaran-Cambrian boundary, coincident with the BACE (e.g. Amthor et al., 2003; Darroch et al., 2018).

Determining the global nature and age of the BACE has been particularly problematic, but is critical for developing a robust biostratigraphic and chronostratigraphic framework across this interval. The BACE reaches a $\delta^{13}C_{carb}$ nadir of -10‰ and has been recorded in all fossiliferous successions with high-resolution $\delta^{13}C_{carb}$ data, except the Nama Group. The FAD of *T. pedum* occurs above the BACE in all regions that host both features (e.g. Smith et al., 2015, 2016; Hodgin et al., 2020). As a radiometric basis for the age of the Ediacaran-Cambrian boundary derives from the Nama Group (Linnemann et al., 2019; Xiao and Narbonne, 2020), the position of the BACE (if present) in the Nama succession must be determined. Recent high precision radiometric and $\delta^{13}C_{carb}$ data from Laurentia appear to constrain the age of the BACE nadir to $\leq$539.4 Ma, coincident with stable positive $\delta^{13}C_{carb}$ data on the Kalahari craton (Hodgin et al., 2020). It has therefore been suggested that the conflicting $\delta^{13}C_{carb}$ trends between the Laurentian and Kalahari datasets may result from local pools of dissolved inorganic carbon (DIC) with distinct isotopic compositions (Hodgin et al., 2020). In order to test whether these data are unrepresentative of global $\delta^{13}C_{carb}$, it is first necessary to discount all alternative possibilities associated with uncertainties in the $\delta^{13}C_{carb}$ age model framework.

Here, we present an updated $\delta^{13}C_{carb}$ framework for the Ediacaran Nama Group of southern Namibia. These data are first correlated regionally by combined litho-, chemo-, and sequence stratigraphy, then constrained in time using published high precision U-Pb ages determined via zircon chemical abrasion isotope dilution thermal ionization mass spectrometry (CA-ID-TIMS). We correlate trends in the resulting Nama reference curve with $\delta^{13}C_{carb}$ data from globally distributed sections that are well constrained by interbedded zircon U-Pb CA-ID-TIMS ages, and robust high-resolution regional section correlation, for the interval ~551 – 538.5 Ma. The $\delta^{13}C_{carb}$ record is then extended to 517 Ma in multiple regions with high resolution litho-, chemo-, and sequence stratigraphic records. Compiled data from sections that host the most robust radiometric constraints throughout this interval act as framework curves to reveal trends in the global data that can be confidently constrained in age. These curves are used to anchor a wider correlation in order to best fit high-resolution $\delta^{13}C_{carb}$ data from key sections that lack robust radiometric constraints.

This allows construction of four possible composite carbon isotope curves and age models, comprising 130 globally distributed sections (Australia, Brazil, Kazakhstan, Mongolia, Morocco, Namibia, Mexico, USA, Canada, Oman, Siberia and South China). These curves are consistent with all reliable radiometric age data and strontium isotope ($^{87}Sr/^{86}Sr$) records between ~551 – 517 Ma (Tables S1 and S2). All models reveal a previously underappreciated degree of variability in the EPIP, incorporating multiple positive and negative excursions preceding the BACE that are globally widespread. Differences between the four age models result from ongoing uncertainties which we review in detail. All FADs and, for Ediacaran taxa, Last Appearance Datums (LADs) of key fossil occurrences are calibrated within this framework (Tables S2 and S3). This provides the basis for biotic temporal and spatial distributions to be accurately constrained and visualized.

2. Constructing a $\delta^{13}C_{carb}$ reference curve for the Nama Group, Kalahari Craton

The Nama Group in Nambia and South Africa, comprises a richly-fossiliferous mixed carbonate-siliciclastic succession deposited in a foreland basin on the Kalahari Craton. The succession developed during flexural subsidence associated with two major orogenies; the Damara to the north, and the Gariep to the southwest (Germs, 1983; Germs and Gresse, 1991; Gresse and Germs, 1993) (Fig. 1). Near-complete exposure and minimal structural deformation across hundreds of square kilometers have inspired half a century of detailed sedimentological and palaeontological research, incorporating high resolution litho-, chemo- and sequence stratigraphy (Darroch et al., 2015, 2016, 2021; Jensen et al., 2000; Saylor, 2003; Saylor et al., 1998; Smith, 1998; Wood et al., 2015). These aspects, in combination with high-precision radiometric age calibration (Bowring et al., 2007; Grotzinger et al., 1995; Linnemann et al., 2019), make the Nama

Group the best candidate succession globally for construction of a terminal Ediacaran $\delta^{13}C_{carb}$ reference curve. This is especially the case for the lower Nama Group (Kuibis Subgroup), where carbonate ramp deposits are ubiquitous throughout the northern (Zaris) sub-basin.

$\delta^{13}C_{carb}$ data from fifteen sections of the Nama Group, Namibia (Saylor et al., 1995; Smith, 1998; Wood et al., 2015), compiled within a sequence stratigraphic framework and calibrated to dated volcanic tuff interbeds, result in a composite Ediacaran Nama $\delta^{13}C_{carb}$ reference curve (Fig. 1). Gaps in the $\delta^{13}C_{carb}$ record of individual sections are permitted at exposure or erosion surfaces, or during significant intervals of siliciclastic deposition. Below, we explore implications for global correlation of the $\delta^{13}C_{carb}$ reference curve derived for the Kuibis (ca. 551 – 546 Ma) and Schwarzrand (<546 – 538 Ma) subgroups.

2.1 The Kuibis Subgroup

In the Kuibis Subgroup succession, positive, laterally consistent $\delta^{13}C_{carb}$ values in the lower Hoogland Member (Zaris Formation) of the Zaris sub-basin are constrained by a zircon U-Pb CA-ID-TIMS age of 547.36 ± 0.23 Ma (Bowring et al., 2007) (Fig. 1). Carbonate strata in multiple sections below this ash bed record a gradual recovery from a negative $\delta^{13}C_{carb}$ excursion. This can be readily correlated with the $\delta^{13}C_{carb}$ trend expressed in strata of the lower Dengying Formation, South China. Recovery from this negative $\delta^{13}C_{carb}$ excursion in the lower Dengying Formation is constrained by a zircon U-Pb CA-ID-TIMS age of 550.1 ± 0.6 Ma (Yang et al., 2021, updated from 551.09 ± 1.02 Ma, Condon et al., 2005) from an ash bed in the underlying Miaohe Member at Jijiawan (/Jiuqunao) section (Table S1). The age of the 0‰ crossing point in the lower Kuibis Subgroup can therefore be anchored to ~550 Ma. The preceding negative excursion (≥550 Ma),

Figure 1

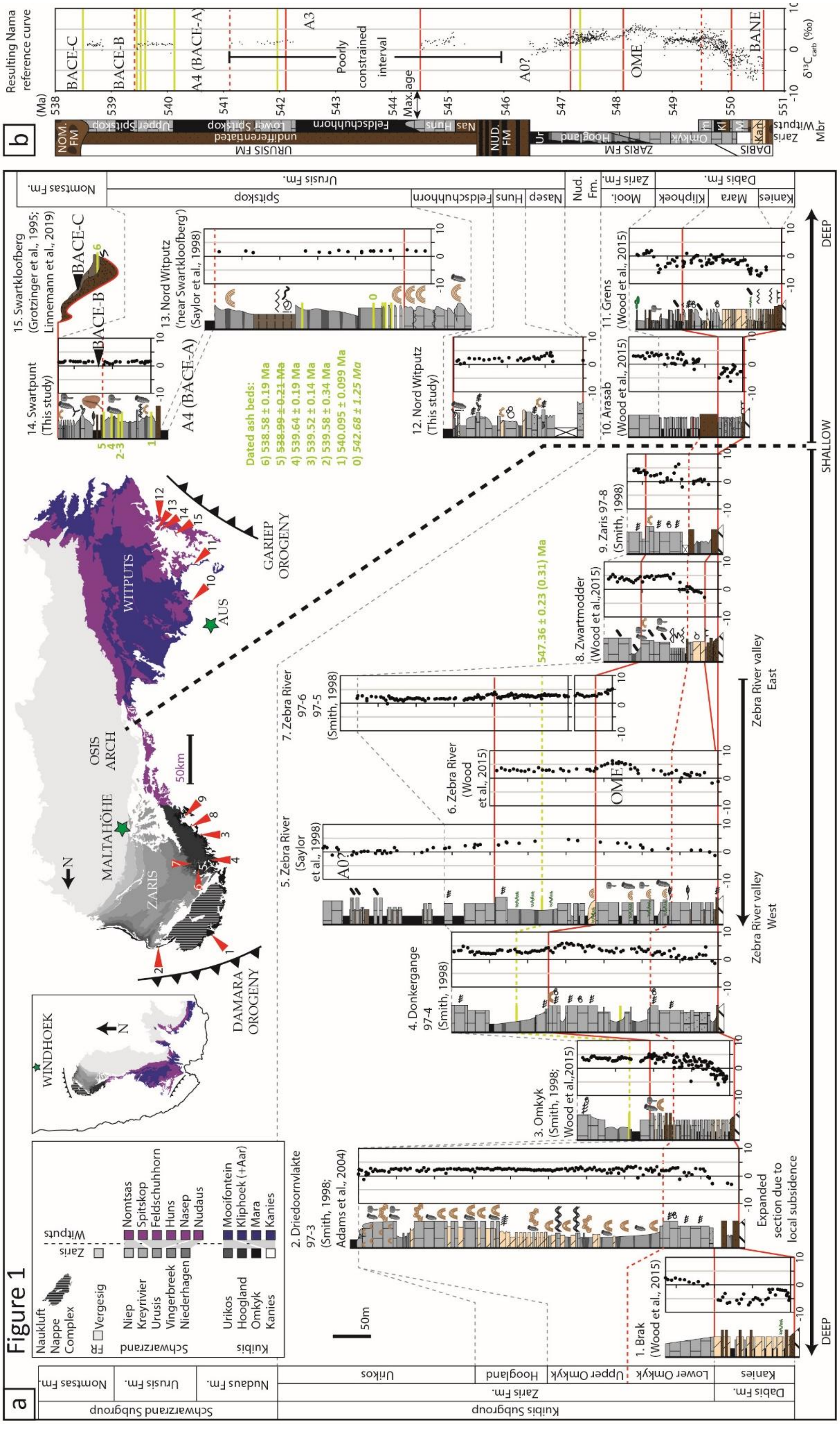
a
b
Naukluft Nappe Complex
Vergesig
Zaris
Witputs
Niep
Kreyrivier
Urusis
Vingerbreek
Niederhagen
Nomtsas
Spitskop
Feldschuhhorn
Huns
Nasep
Nudaus
Urikos
Hoogland
Omkyk
Kanies
Mooifontein
Kliphoek (+Aar)
Mara
Kanies
Schwarzrand
Kuibis
Schwarzrand Subgroup
Kuibis Subgroup
Nomtsas Fm.
Urusis Fm.
Nudaus Fm.
Zaris Fm.
Dabis Fm.
Urikos
Hoogland
Upper Omkyk
Lower Omkyk
Kanies
WINDHOEK
N
DAMARA OROGENY
MALTAHÖHE
ZARIS
OSIS ARCH
50km
WITPUTS
AUS
GARIEP OROGENY
50m
1. Brak (Wood et al., 2015)
2. Driedoornvlakte 97-3 (Smith, 1998; Adams et al., 2004)
Expanded section due to local subsidence
3. Omkyk (Smith, 1998; Wood et al.,2015)
4. Donkergange 97-4 (Smith, 1998)
5. Zebra River (Saylor et al., 1998)
A0?
6. Zebra River (Wood et al., 2015)
OME
7. Zebra River 97-6 97-5 (Smith, 1998)
547.36 ± 0.23 (0.31) Ma
8. Zwartmodder (Wood et al.,2015)
9. Zaris 97-8 (Smith, 1998)
10. Arasab (Wood et al., 2015)
11. Grens (Wood et al., 2015)
12. Nord Witputz (This study)
13. Nord Witputz ('near Swartkloofberg') (Saylor et al., 1998)
14. Swartpunt (This study)
15. Swartkloofberg (Grotzinger et al., 1995; Linnemann et al., 2019)
A4 (BACE-A)
BACE-B
BACE-C
Dated ash beds:
6) 538.58 ± 0.19 Ma
5) ~~538.99 ± 0.21 Ma~~
4) 539.64 ± 0.19 Ma
3) 539.52 ± 0.14 Ma
2) 539.58 ± 0.34 Ma
1) 540.095 ± 0.099 Ma
0) 542.68 ± 1.25 Ma
Zebra River valley West
Zebra River valley East
DEEP
SHALLOW
DEEP
-10
0
10
Spitskop
Feldschuhhorn
Huns
Nasep
Nud. Fm.
Mooi.
Kliphoek
Mara
Kanies
Zaris Fm.
NOM. FM
URUSIS FM
NUD. FM
ZARIS FM
DABIS
Upper Spitskop
Lower Spitskop
Feldschuhhorn
Nas Huns
undifferentiated
Ur
Hoogland
Omkyk
Kl
M
Kan
Zaris Mbr
Witputs Mbr
(Ma)
538
539
540
541
542
543
544
545
546
547
548
549
550
551
Max. age
Resulting Nama reference curve
BACE-C
BACE-B
A4 (BACE-A)
A3
Poorly constrained interval
A0?
OME
BANE
$\delta^{13}C_{carb}$ (‰)
-10
0
10

Fig. 1. Sequence stratigraphic and carbon isotope chemostratigraphic correlation of the Nama Group, Namibia with resulting reference curve for the Kalahari craton for the interval ~550 – 538.5 Ma (Saylor et al., 1998; Smith, 1998; Wood et al., 2015)**. (a)** Litho-, chemo- and sequence stratigraphic correlation for sections of the Zaris sub-basin after Smith (1998) and Wood et al. (2015). New data for sections 12 and 14. **(b)** Resulting Nama $\delta^{13}C_{carb}$ reference curve showing position of tuff bed age constraints and sequence boundaries. Note that age model between ca. 547 Ma and 540 Ma remains poorly constrained. BANE: Basal Nama Excursion, OME: Omkyk Excursion, A0, A3 and A4 named after tentative correlation with radiometrically dated excursions in the A0, A3 and A4 members of the Ara Group, Oman (see text for details). BACE-A, B and C correlate to the positions of the 1n/BACE in models A, B and C, respectively (Table S2). See Fig. 2 for key to lithology and sequence stratigraphy. Radiometric data ($^{238}U/^{206}Pb$ CA-ID-TIMS) are from (Bowring et al., 2007; Linnemann et al., 2019) and italicized data (air abrasion ID-TIMS $^{207}Pb/^{206}Pb$) are from Grotzinger et al. (1995) recalculated in Schmitz (2012) (the age of tuff bed 5 is discounted; details in Table S1). See Fig. S1 for a high-resolution version of this figure.

whilst present and radiometrically calibrated in South China, is expressed most completely and with highest resolution in multiple sections by carbonates of the Dabis Formation in both the Zaris and Witputs sub-basins of the Nama Group. This is a recently recognized distinct negative $\delta^{13}C_{carb}$ excursion (Yang et al., 2021), herein termed the basal Nama excursion (BANE, Fig. 1b).

Subsequent to the BANE, peak $\delta^{13}C_{carb}$ values are reached within the upper Omkyk Member of the Zaris Formation, and lower members of the Dengying Formation. This $\delta^{13}C_{carb}$ peak is herein termed the Omkyk excursion (OME, Fig. 1b).

The onset of a gradual decline prior to 547.32 ± 0.31 Ma (Bowring et al., 2007) is constrained by a tuff bed within the lower Hoogland Member of the upper Zaris Formation and correlative intervals of the lower Dengying Formation (Table S2). Declining $\delta^{13}C_{carb}$ values culminate in a short-lived (<0.5 Ma) negative excursion, with a recovery to ~0‰ recorded at 546.72 ± 0.21 Ma by a tuff bed in the middle A0 Member of the Ara Group, Oman (see section 5.5, Bowring et al., 2007; Schmitz, 2012). This minor negative excursion is expressed in carbonate interbeds of the Urikos Member of the Zaris Formation, Namibia, and the A0 Member of the Ara Group, Oman (Bowring et al., 2007; Saylor et al., 1998). It may also correspond with a minor negative excursion recorded in the lower Khatyspyt Fm of the northern Siberian Platform (Cui et al., 2016; Knoll et al., 1995), although this remains uncertain (see section 5.3).

Based on the interbasinal $\delta^{13}C_{carb}$ correlation herein (Fig. 1) and published palaeontological information, carbonates in the lower Kuibis Subgroup (Mara Member of the Dabis Fm) of the Witputs sub-basin host the earliest FAD of *Cloudina* (Germs, 1983). This FAD may predate the 0‰ recovery from the BANE, however the precise location of the section that hosts the Mara Member cloudinids and associated $\delta^{13}C_{carb}$ data is undocumented. In the Zaris sub-basin, the earliest recorded appearance of cloudinids occurs immediately above the 0‰ recovery from the BANE (~550 Ma) within the lowermost upper Omkyk Member (Fig. 1). Siliciclastics in the lower Kuibis Subgroup (Kliphoek Member of the Dabis Formation) of the Witputs sub-basin, deposited immediately below the 0‰ recovery from the BANE, contain a rich fossil archive of soft-bodied biota (Maloney et al., 2020). The majority of the soft-bodied fossils in this interval correspond to the Nama assemblage, however this level may also host the regional last appearance of elements of the White Sea assemblage, including *Ausia fenestrata* (Hahn and Pflug, 1985; Pickford, 1995). Fossil impressions interpreted as *Ausia* have previously been noted from the middle Verkhovka

Formation of the White Sea area (Grazhdankin, 2004), below a volcanic tuff in the overlying lower Zimnie Gory Formation recently redated to 552.96 ± 0.19 (Yang et al., 2021) (Table S1).

2.2 The Schwarzrand Subgroup

During deposition of the Schwarzrand Subgroup the locus of carbonate sedimentation shifted to the Witputs sub-basin, and siliciclastic deposits of the Zaris sub-basin record gradual basin infill (Germs, 1983; Gresse and Germs, 1993). The existing $\delta^{13}C_{carb}$ record of the Schwarzrand Subgroup consists of a low resolution $\delta^{13}C_{carb}$ dataset from the Huns and lower Spitskop members of the Urusis Formation, and multiple datasets of varying resolution from the upper Spitskop Member at Farm Swartpunt (Linnemann et al., 2019; Saylor et al., 1998; Wood et al., 2015). We present new $\delta^{13}C_{carb}$ data for two sections from the Urusis Fm (Nord Witputz and Swartpunt), and construct a composite lithostratigraphic and chemostratigraphic column incorporating available data from the lower Spitskop Member (Saylor et al., 1998) (Fig. 2).

Shallow marine facies of the lower Huns Member at Nord Witputz show initially high $\delta^{13}C_{carb}$ values (max = 4.24‰) that gradually decrease to reach 0.08‰ near the top of the section (Fig. 2). Higher order variability in the $\delta^{13}C_{carb}$ data of the lower Huns Member may be associated with a series of parasequences, where lower $\delta^{13}C_{carb}$ reflects deepening of the depositional environment. Samples of both shallow and marginally deeper facies show pronounced and simultaneous decreases in their mean $\delta^{13}C_{carb}$ composition up-section, which may reflect a gradual trend in seawater $\delta^{13}C_{carb}$ overprinted by minor perturbations associated with regional facies. Based on regional stratigraphic correlation, the Urusis Fm of the Witputs sub-basin was deposited equivalent to siliciclastic deposits of the Schwarzrand Subgroup in the Zaris sub-basin (Germs, 1983), and is therefore likely to be younger than ~546 Ma (Fig. 1).

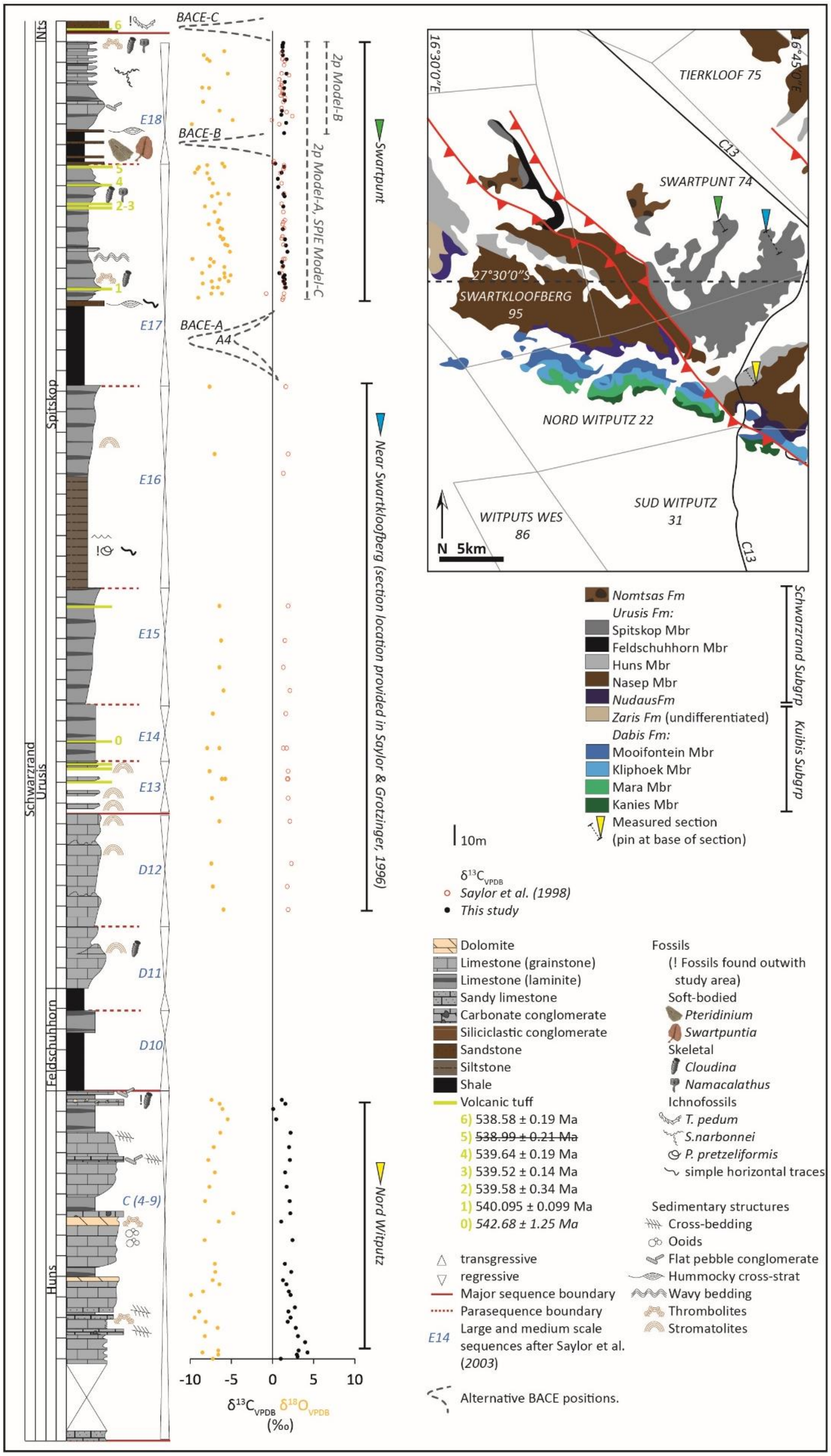
Nts
Spitskop
Schwarzrand
Urusis
Feldschuhhorn
Huns
BACE-C
BACE-B
BACE-A
A4
2p Model-B
2p Model-A, SPIE Model-C
Swartpunt
Near Swartkloofberg (section location provided in Saylor & Grotzinger, 1996)
Nord Witputz
E18
E17
E16
E15
E14
E13
D12
D11
D10
C (4-9)
6
5
4
2-3
1
0
-10
-5
0
5
10
δ13CVPDB δ18OVPDB
(‰)
16°30'0"E
16°45'0"E
TIERKLOOF 75
C13
SWARTPUNT 74
27°30'0"S
SWARTKLOOFBERG 95
NORD WITPUTZ 22
WITPUTS WES 86
SUD WITPUTZ 31
N
5km
Nomtsas Fm
Urusis Fm:
Spitskop Mbr
Feldschuhhorn Mbr
Huns Mbr
Nasep Mbr
NudausFm
Zaris Fm (undifferentiated)
Dabis Fm:
Mooifontein Mbr
Kliphoek Mbr
Mara Mbr
Kanies Mbr
Measured section (pin at base of section)
Schwarzrand Subgrp
Kuibis Subgrp
10m
δ13CVPDB
Saylor et al. (1998)
This study
Dolomite
Limestone (grainstone)
Limestone (laminite)
Sandy limestone
Carbonate conglomerate
Siliciclastic conglomerate
Sandstone
Siltstone
Shale
Volcanic tuff
6) 538.58 ± 0.19 Ma
5) ~~538.99 ± 0.21 Ma~~
4) 539.64 ± 0.19 Ma
3) 539.52 ± 0.14 Ma
2) 539.58 ± 0.34 Ma
1) 540.095 ± 0.099 Ma
0) 542.68 ± 1.25 Ma
transgressive
regressive
Major sequence boundary
Parasequence boundary
E14 Large and medium scale sequences after Saylor et al. (2003)
Alternative BACE positions.
Fossils
(! Fossils found outwith study area)
Soft-bodied
Pteridinium
Swartpuntia
Skeletal
Cloudina
Namacalathus
Ichnofossils
T. pedum
S.narbonnei
P. pretzeliformis
simple horizontal traces
Sedimentary structures
Cross-bedding
Ooids
Flat pebble conglomerate
Hummocky cross-strat
Wavy bedding
Thrombolites
Stromatolites

Fig. 2. Geological map and sampled sections of the Urusis Formation, Nama Group, southern Namibia. Composite section after (Saylor, 2003). Geological map shows relative positions of measured sections. Map redrawn from Saylor and Grotzinger (1996) using the 1:250000 map of Ai-Ais (2716), Geological Survey of Namibia, Ministry of Mines and Energy. Radiometric data (^{238}U/^{206}Pb CA-ID-TIMS) are from Linnemann et al. (2019) and italicized data (air abrasion ID-TIMS ^{207}Pb/^{206}Pb) are from Grotzinger et al. (1995) recalculated in Schmitz (2012) (the age of tuff bed 5 is discounted; details in Table S1). BACE-A, B and C correlate to the positions of the 1n/BACE in models A, B and C, respectively (Table S2).

The lower Spitskop Member contains a volcanic tuff deposit with a ^{207}Pb/^{206}Pb age of 542.68 ± 1.25 Ma (Grotzinger et al., 1995, recalculated in Schmitz, 2012) (Table S1). Carbon isotope data of relatively low resolution have previously been presented for the lower Spitskop Member from the lower part of a composite section described as ‘near Swartkloofberg’ (Saylor et al., 1998) (Fig. 2). The lower part of this section (corresponding to medium scale sequences D11 – E16 of Saylor, 2003) lies to the north of our Huns Member section, and the upper part (medium scale sequences E17 and E18 of Saylor, 2003) corresponds to the Swartpunt section (Fig. 2, and see Fig. 1 of Saylor and Grotzinger, 1996). According to Saylor (2003), a total thickness of ~370 m of interbedded shale and carbonate, for which only 18 data points are currently published, separates the Huns Member at Nord Witputz from the upper Spitskop Member at Swartpunt (Fig. 2) (Saylor et al., 1998). However, an alternative correlation for the relative position of the lower Spitskop Member data is discussed in the Supplementary Information. Future high resolution resampling for $\delta^{13}C_{carb}$, in addition to re-dating of ash beds throughout the lower Spitskop Member southeast of Swartpunt using the updated CA-ID-TIMS methodology, should yield valuable information to better constrain this interval in the global age model.

3. Developing Age Models and the stratigraphic position of the BACE in Namibia

3.1 The terminal Ediacaran (546–541 Ma)

The $\delta^{13}C_{carb}$ record between 546 Ma and 543 Ma remains poorly constrained globally due to a dearth of $\delta^{13}C_{carb}$ data interbedded with tuff beds dated by reliable radiometric methods (Fig. 3a). However, when the new $\delta^{13}C_{carb}$ data of the Huns Member are compared to other $\delta^{13}C_{carb}$ profiles from ca. 546-543 Ma from other cratons (e.g. Yangtze Block, Laurentia, Amazonia and Siberia, Fig. 3), the magnitude and overall trend in the data are consistent with a temporal position coincident with the initial downturn from positive values of up to 5‰ recorded in the middle Member of the Dengying Formation (Gaojiashan Member and equivalent units). We stress that this is a maximum age estimate based on the assumption that the age constraint from the overlying lower Spitskop Member (542.68 ± 1.25 Ma, Grotzinger et al., 1995, updated in Schmitz, 2012) approximates the true age of the lower Spitskop Member (see Supplementary Text for further discussion). A subsequent recovery to a positive $\delta^{13}C_{carb}$ peak is well constrained by 5 radiometric ages; 543.40 ± 3.5 Ma from the Baimatuo Member of the Yangtze Platform (Huang et al., 2020), 542.90 ± 0.12 Ma and 542.33 ± 0.11 Ma from the lower and upper A3 Member of the Ara Group (Bowring et al., 2007), and 542.37 ± 0.28 Ma and 541.85 ± 0.75 Ma from the upper Tamengo Formation, Brazil (Parry et al., 2017). Here, $\delta^{13}C_{carb}$ values increase once more to 3–5.6‰ (herein termed the 'A3' anomaly, Fig. 3) and then decline to a plateau of 0–2‰ prior to 541 Ma (Tables

S1 and S2). The available data from the lower Spitskop Member, though sparse, correlate with predominantly positive $\delta^{13}C_{carb}$ values that precede the negative excursion recorded in the A4 Member of the Ara Group (Fig. 3).

There are three possible positions for the BACE in the Nama Group, all of which are consistent with available radiometrically-dated tuff deposits and occur in siliciclastic units without $\delta^{13}C_{carb}$ data (Fig. 2). These give rise to three alternative age models A, B and C (Fig. 3). In each, we assume that the age of the A4 Member accurately constrains the $\delta^{13}C_{carb}$ excursion recorded in the A4 Member, as shown by Bowring et al. (2007) (see section 5.5 for further discussion of the Ara Group age model). For ease of distinction, the excursion in the A4 Member is herein termed the 'A4 anomaly'. The position of the BACE in relation to the Spitskop Member is inferred either within the shale interval of medium scale sequence E17, stratigraphically beneath the ca. 540 Ma tuff bed at the base of the Swartpunt section (Model A), within the shale interval of medium scale sequence E18 above the well dated horizon constrained by multiple tuff deposits at ca. 539.6 Ma (Linnemann et al., 2019) (Model B), or in strata younger than the Swartpunt section (<538 Ma, Model C) (Figs. 2, 3).

Models A and B are consistent with a recent radiometric constraint from the La Ciénega Formation, Mexico (Hodgin et al., 2020). However, models B and C imply that the A4 anomaly does not correspond to the BACE, but rather to an earlier negative excursion with a recovery at or before ca. 540 Ma (Figs. 3c and d). In models A and B, the apparent absence of the BACE nadir in the Nama Group is interpreted simply as a function of coincident deposition of outer shelf shale for which $\delta^{13}C_{carb}$ data are lacking (Fig. 2). Indeed, if the A4 anomaly is of global significance and

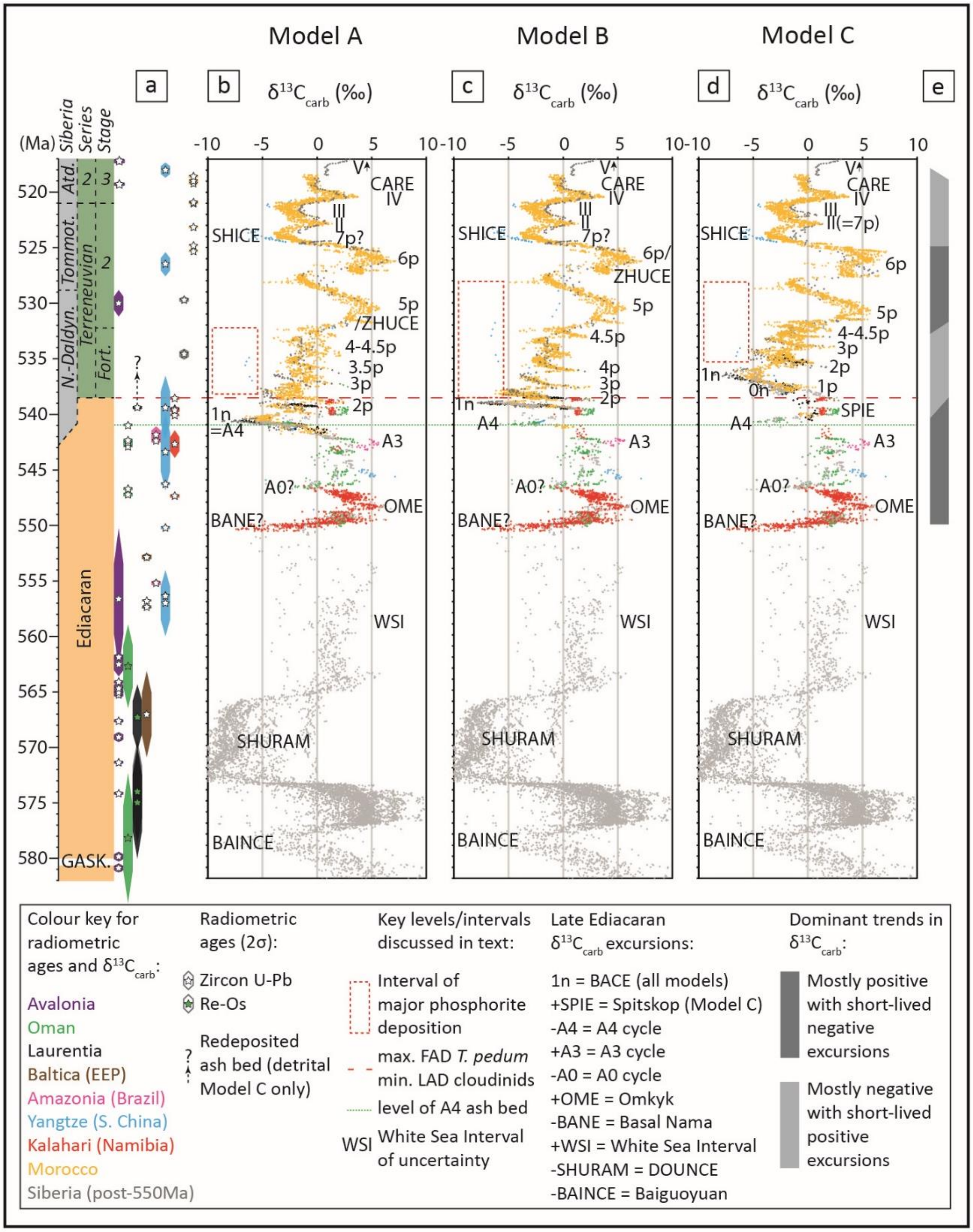

Fig. 3. Carbon isotope chemostratigraphic correlation models A–C. Ediacaran $\delta^{13}C_{carb}$ data are only presented for sections that are anchored by associated radiometric ages (e.g. Swartpunt), or where high resolution $\delta^{13}C_{carb}$ data are confidently correlated regionally to sections that contain radiometrically dated beds (e.g. La Ciénega Fm and Kuibis Subgroup sections). All data are

coloured by craton (or region). Age model for 582–550 Ma interval in grey after Yang et al. (2021). **(a)** Available radiometric ages with associated internal/analytical uncertainty. See Supplementary Materials (Tables S1 and S2) for references to radiometric and $\delta^{13}C_{carb}$ data, in addition to biostratigraphic and section information. BANE marks the basal Nama negative $\delta^{13}C_{carb}$ excursion, OME marks the positive $\delta^{13}C_{carb}$ peak recorded in the Omkyk Member of the Zaris Formation of the Nama Group, Namibia. A0, A3 and A4 mark the relative positions of $\delta^{13}C_{carb}$ excursions with radiometric ages in the Ara Group, Oman. $\delta^{13}C_{carb}$ peaks 1p–6p, and II–V are labelled after direct correlation with the Sukharikha River section and Lena River sections of Siberia (e.g. Kouchinsky et al., 2007). 1n is equivalent to the BACE in all models.

correctly constrained in time (see section 5.5), it is sequestered within a shale interval stratigraphically beneath the Swartpunt section in all models.

3.2 $^{87}Sr/^{86}Sr$ chemostratigraphy of the Ediacaran-Cambrian transition

Matching $\delta^{13}C_{carb}$ excursions in fossiliferous Ediacaran sections that display one or more $\delta^{13}C_{carb}$ excursions but lack radiometric ages is complicated by the finding here of multiple global late Ediacaran $\delta^{13}C_{carb}$ excursions. This is equally problematic for the multiple excursions present in the Fortunian Stage of the lower Cambrian. In an attempt to address this issue, we compile a further database of published $^{87}Sr/^{86}Sr$ data as an independent chronostratigraphic test (Table S2, Fig. 4). These $^{87}Sr/^{86}Sr$ data have been screened on a case-by-case basis using available geochemical data to account for modification of the Sr isotope composition associated with diagenetic alteration or common Rb (see Supplementary Text, Table S2). Reliable $^{87}Sr/^{86}Sr$ data

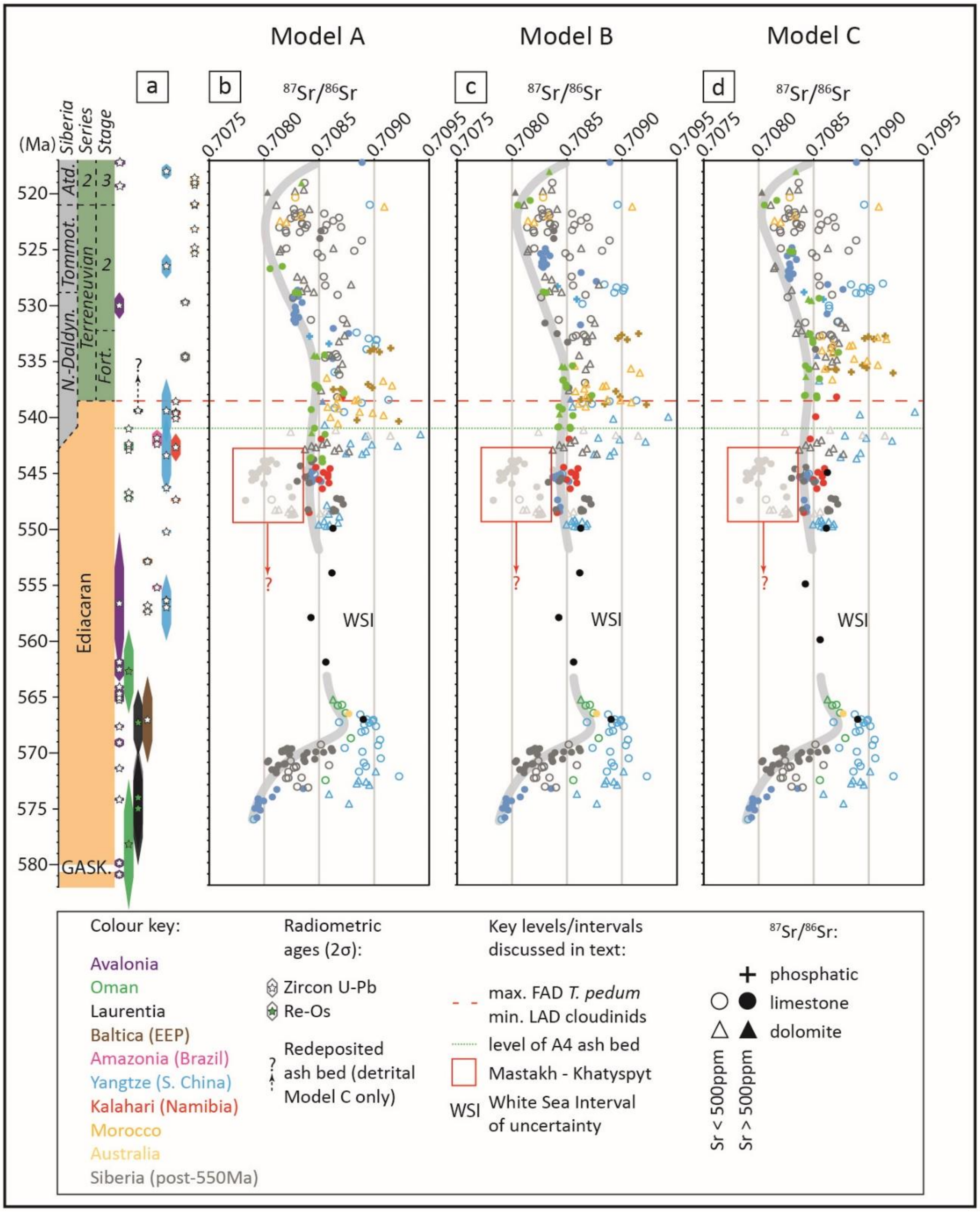

Fig. 4. Sr isotope chemostratigraphy with associated radiometric ages (a) resulting from carbon isotope chemostratigraphy after Model A (b), Model B (c) and Model C (d) for the

interval ~576–517 Ma. Red boxes highlight unusually depleted values of the Mastakh and Khatyspyt formations. Data coloured according to craton (or region).

are anchored directly to the prescribed age of the corresponding $\delta^{13}C_{carb}$ value in the same sample. In this way, we are able to constrain trends that we consider the most robust estimate of seawater $^{87}Sr/^{86}Sr$ composition, and use $^{87}Sr/^{86}Sr$ as an independent chronostratigraphic indicator for age models A, B and C for sections that lack radiometric ages (Fig. 4).

Revision of the age of the Shuram excursion after Rooney et al. (2020) and Yang et al. (2021) results in a highly uncertain interval ('WSI' in Figs. 3, 4) where $^{87}Sr/^{86}Sr$ data are largely unconstrained with the possible exception of values corresponding to the Blueflower Formation of NW Canada (Narbonne et al., 1994). The resulting late Ediacaran $^{87}Sr/^{86}Sr$ record (~551 – 538 Ma) is characterized by values that are relatively invariant about 0.70842–0.70846, and these values are consistent between Namibia, South China, Mongolia and southeastern Siberia (Table S2). The Khatyspyt Formation yields inconsistent outlier values down to 0.70784 (boxed data in Fig. 4b-d), accompanied by a high degree of scatter in $\delta^{13}C_{carb}$. The position of the Khatyspyt Formation remains problematic due to uncertainties in the nature of the boundary with the overlying Turkut Formation (see section 5.3). However, we consider the correlation proposed herein to be a reasonable estimate based on consistent $\delta^{13}C_{carb}$ trends between the Khatyspyt Formation and globally distributed sections throughout this interval. $^{87}Sr/^{86}Sr$ values remain constant throughout much of the Fortunian, but begin to decline approximately coincident with rising $\delta^{13}C_{carb}$ values in Cambrian Stage 2, reaching a nadir of ~0.70805 near the boundary between stages 2 and 3, prior to gradual recovery during upper Stage 3.

3.3 Incorporating additional section data

In order to test the validity of our Nama reference curve for global $\delta^{13}C_{carb}$ correlation, and to explore the three alternative age models, we expand our dataset to incorporate published data from correlative strata into the early Cambrian from other cratons and regions (e.g. Yangtze Block, Oman, Laurentia, Amazonia, Morocco, Siberia, Mongolia, Fig. 3). We first prioritise sections with $\delta^{13}C_{carb}$ data and interbedded volcanic deposits dated via zircon U-Pb CA-ID-TIMS. Values of $\delta^{13}C_{carb}$, anchored by the age of interbedded tuff deposits (within internal/analytical uncertainty) provide the scaffold for wider correlation, and intervals that lack constraint from radiometric ages are considered to be the most uncertain (Tables S1 and S2). Within this framework, we utilize regional sequence stratigraphic models that incorporate gaps in the carbon isotope record of individual sections, due to unconformities or intervals of siliciclastic deposition, while excluding unreasonable sedimentation rates for given tectonic settings (Table S2). Individual sections are subdivided into units of consistent lithofacies, and relative sedimentation rates are permitted to vary accordingly (Table S2). Deeper marine carbonate facies (e.g. organic-rich thinly bedded limestone laminae) and intervals of phosphorite deposition typically exhibit lower rates of deposition than shallow marine carbonate facies (e.g. dolostone and oolitic limestone deposited above fair weather wave base) within each region (Table S2).

Several high resolution $\delta^{13}C_{carb}$ correlation frameworks have been assembled for the lower Cambrian (e.g. Brasier et al., 1994; Knoll et al., 1995; Kouchinsky et al., 2017, 2007, 2005; Maloof et al., 2010; Smith et al., 2015, Table S2). Our new framework is consistent with that derived by Maloof et al., (2010), but updates their model through incorporation of more recent high resolution $\delta^{13}C_{carb}$ datasets (e.g. Kouchinsky et al., 2017; Smith et al., 2015) and radiometric constraints (e.g.

Hodgin et al., 2020; Landing et al., 2020; Linnemann et al., 2019). We also consider updated biostratigraphic information integrated with $\delta^{13}C_{carb}$ from sections in South China (Steiner et al., 2020), Australia (Betts et al., 2018) and Laurentia (Dilliard et al., 2007).

All global $\delta^{13}C_{carb}$ correlation models reveal widespread, but short-lived, negative excursions in an interval dominated by positive $\delta^{13}C_{carb}$ values in the terminal Ediacaran ~551–538 Ma (Fig. 3e). These models differ most prominently in their correlation of the BACE nadir, either within the latest Ediacaran (models A and B) or within the lowermost Cambrian (Model C), as defined by its position relative to the radiometric age that currently constrains the FAD of *T. pedum* in Namibia (Fig. 3). However, *T. pedum* has not been reported in strata older than the BACE nadir in any region that hosts the BACE, and so the BACE nadir may in fact be older than the Ediacaran-Cambrian boundary in all models (discussed further below). Models B and C offer valid alternatives to the generally accepted Model A that are consistent with radiometric (models B and C) and stratigraphic (Model C) information in all regions. The relative likelihood of each of these three models, and their biostratigraphic implications, are further discussed below.

4. Implications for the age of the BACE and the Ediacaran-Cambrian boundary

The A4 anomaly records minimum $\delta^{13}C_{carb}$ values of -5‰ and one outlier value of -6.7‰ (Amthor et al., 2003; Bowring et al., 2007) (Figs. 3 and 5). The onset of this negative excursion is anchored by an age of 541.00 ± 0.13 Ma (Bowring et al., 2007). The overlying A5 Member of the Ara Group records stable positive values of 2-3‰, prior to the onset of another negative excursion (Amthor et al., 2003). The radiometric age of the A4 Member has been used to constrain an onset age for the BACE of ~541 Ma (Model A, e.g. Bowring et al., 2007; Hodgin et al., 2020; Linnemann et al., 2019; Maloof et al., 2010). As previously noted, the BACE reaches a nadir of -10‰ and is recorded in all fossiliferous successions with high-resolution $\delta^{13}C_{carb}$ data, except the Nama Group, Namibia (Figs. 3 and 5, Table S2). A maximum age of 539.40 ± 0.23 Ma derives from a sandy dolostone bed in the La Ciénega Formation, Mexico, which lies within negative $\delta^{13}C_{carb}$ values inferred to correspond to the BACE interval (Tables S1 and S2, Hodgin et al., 2020). However, strata of the upper Spitskop Member of the Urusis Formation (Nama Group, southern Namibia) at the Swartpunt section record relatively stable positive $\delta^{13}C_{carb}$ values about 1‰ that are consistent with values from the A5 Member and constrained by 4 high resolution tuff bed ages between ca. 540 Ma and 539.5 Ma (Figs. 2, 3, 5, Table S1) (Linnemann et al., 2019).

In Model A (Fig. 3b), the A4 anomaly and BACE are equivalent and constrained below the Swartpunt section in the shale interval of medium scale sequence E17 (Fig. 2). In this model, the BACE onset is at ca. 541 Ma, constrained in the A4 Member, and the recovery occurs at or before 540 Ma, constrained at the base of Swartpunt section. This is also consistent with the interpreted depositional age being close to the radiometric age determined for the sandy dolostone bed in the La Ciénega Fm, Mexico (Hodgin et al., 2020). However, this implies that 1) the clastic unit that hosts the sandy dolostone bed was deposited at a slower depositional rate above the BACE nadir, 2) the BACE recovery and plateau recorded at Swartpunt are constrained within the clastic horizon of the La Ciénega Fm and are therefore not recorded, and 3) a second more minor negative excursion is recorded above the level of the dolostone bed (possibly equivalent to the onset of 2n or a preceding minor negative excursion).

In Model A, positive $\delta^{13}C_{carb}$ values in the uppermost Spitskop Member at Swartpunt may correlate with the 2p interval in Siberia (Kouchinsky et al., 2007), Mongolia (Smith et al., 2015) and possibly Morocco (Maloof et al., 2010), all of which postdate the BACE nadir (Fig. 3b). However, in all areas that host high-resolution Fortunian $\delta^{13}C_{carb}$ records, peaks 2p-4.5p appear to be short-lived positive excursions in an interval dominated by negative mean $\delta^{13}C_{carb}$ values (Fig. 3e). The duration of the 2p interval implied by the Swartpunt radiometric data therefore appears to contradict the best-fit $\delta^{13}C_{carb}$ correlations of Fortunian sections (Maloof et al., 2010), notwithstanding the possibility for stratigraphic condensation in other regions at the 2p level (Figs. 3b and e). We consider the caveats associated with the La Ciénega Fm correlation and inconsistencies relating to inferred peak duration between Swartpunt and 2p to make Model A less likely than models B or C for the BACE position, although it remains possible.

By contrast, models B and C imply that the A4 anomaly and BACE are two distinct excursions, with nadirs that are separated from one another by up to 5 million years (Figs. 3-5). In Model B (Fig. 3c) a return to positive $\delta^{13}C_{carb}$ values following the A4 anomaly is constrained by the age of 540.095 ± 0.099 Ma at the base of the Swartpunt section, Namibia (Fig. 2) (Linnemann et al., 2019). The BACE onset occurred after ~539.6 Ma, as constrained by three radiometric ages from the Swartpunt section immediately below carbonates that record a decrease in $\delta^{13}C_{carb}$ to 0‰ (Figs. 2 and 3c, Table S1, Linnemann et al., 2019), which is consistent with the aforementioned radiometric constraint of 539.4 Ma from the La Ciénega Formation, Mexico (Hodgin et al., 2020). In this model, recovery from the BACE in Namibia occurred prior to ~538.6 Ma, consistent with a likely minimum age for the uppermost Spitskop Member at Swartpunt, as constrained by an ash bed age within the overlying Nomtsas Formation at a neighboring section (Linnemann et al., 2019) (Figs. 1 and 2). Although this model is consistent with all radiometric constraints, it implies that the BACE was a very short-lived event on the order of 1 Myr. This model demands that some sections (e.g. Sukharikha River) exhibited significantly higher sedimentation rates during the

BACE (1n) interval than the overlying 2p-5p interval, which appears inconsistent with the relatively monotonous lithofacies documented throughout.

Figure 5 presents age Model C for selected successions that host the highest resolution $\delta^{13}C_{carb}$ data for the critical late Ediacaran to Cambrian Stage 3 (Atdabanian) interval, in regions without significant Fortunian phosphorite deposition. Sections in Morocco, the Zavkhan terrane of Mongolia, and the Siberian Platform have limited Ediacaran-Fortunian radiometric ages, and therefore rely upon best-fit $\delta^{13}C_{carb}$ correlation throughout this interval. In Model C (Figs. 3d and 5), the onset of the BACE is inferred to post-date the Swartpunt section (<538.5 Ma). Stable positive $\delta^{13}C_{carb}$ values in the interval ~540 – 539.5 Ma, as constrained at Swartpunt, separate the A4 anomaly from the BACE with the resulting peak herein termed the Spitskop excursion (SPIE, Figs. 3d and 5). Model C implies that 1) the A4 anomaly is distinct from the BACE, and 2) the age derived from the La Ciénega Formation (Hodgin et al., 2020) is best interpreted as detrital (Fig. 5). In this model, the sandy dolostone bed in the La Ciénega Formation was deposited up to 3 Myr after eruption of the incorporated tuffaceous material based on best fit with the $\delta^{13}C_{carb}$ curve and constant average rates of sedimentation.

Figure 5 also shows that age-calibrated stratigraphy in many successions record a striking regional lithostratigraphic transition across the Ediacaran-Cambrian boundary interval. In many regions, the transition is marked by a widespread erosive unconformity or exposure surface (e.g. Namibia, NE Siberia), and/or a subsequent change in dominant lithofacies which may reflect changes in global sea level. Whilst invoking a eustatic driver for combined litho- and chemostratigraphic variability across this transitional interval is complicated by regional tectonics, this may have significant biostratigraphic implications that warrant future consideration.

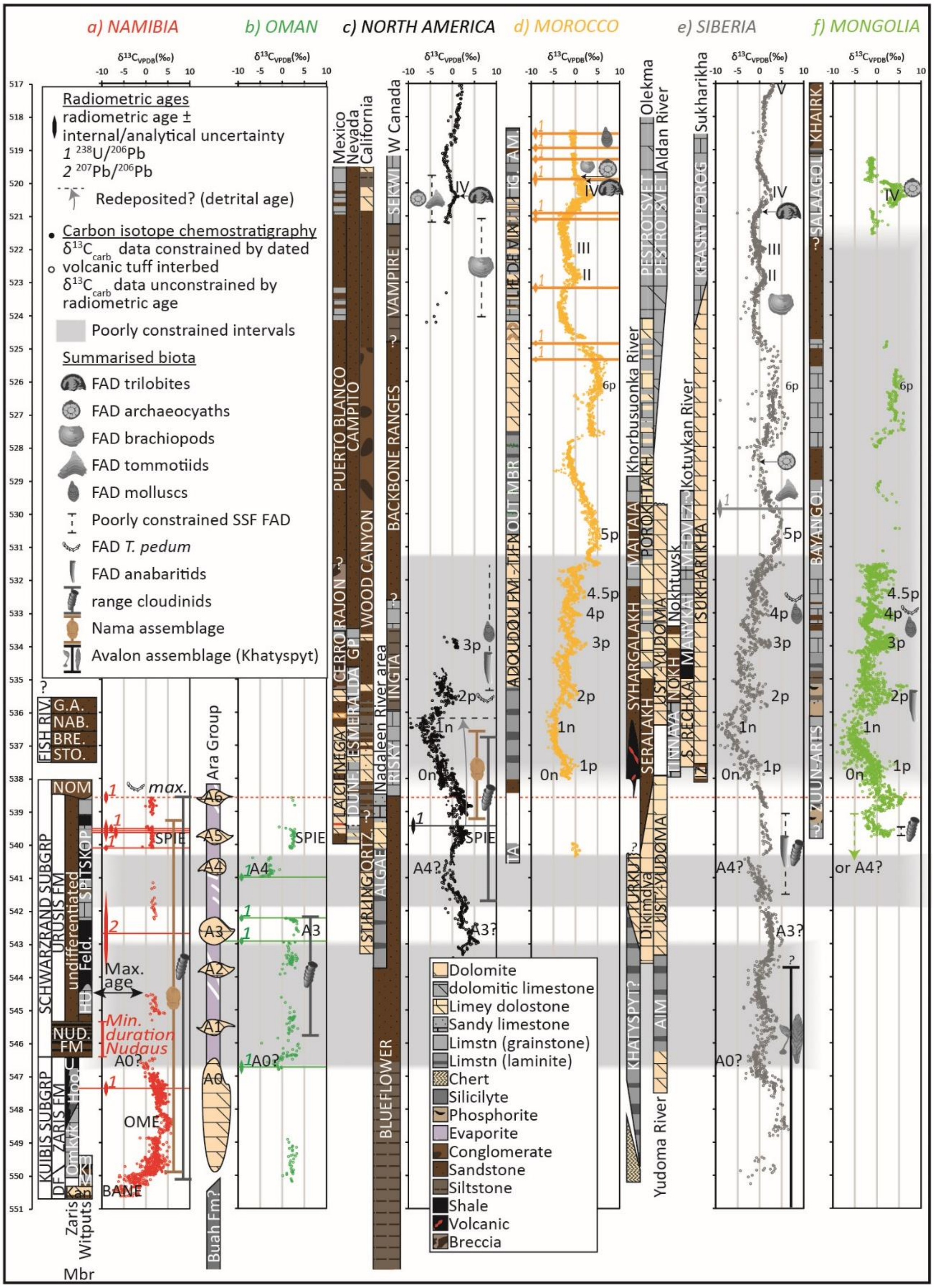
a) NAMIBIA
b) OMAN
c) NORTH AMERICA
d) MOROCCO
e) SIBERIA
f) MONGOLIA
$\delta^{13}C_{VPDB}$(‰)
-10 -5 0 5 10
517 518 519 520 521 522 523 524 525 526 527 528 529 530 531 532 533 534 535 536 537 538 539 540 541 542 543 544 545 546 547 548 549 550 551
Radiometric ages
radiometric age ± internal/analytical uncertainty
1 $^{238}U/^{206}Pb$
2 $^{207}Pb/^{206}Pb$
Redeposited? (detrital age)
Carbon isotope chemostratigraphy
$\delta^{13}C_{carb}$ data constrained by dated volcanic tuff interbed
$\delta^{13}C_{carb}$ data unconstrained by radiometric age
Poorly constrained intervals
Summarised biota
FAD trilobites
FAD archaeocyaths
FAD brachiopods
FAD tommotiids
FAD molluscs
Poorly constrained SSF FAD
FAD T. pedum
FAD anabaritids
range cloudinids
Nama assemblage
Avalon assemblage (Khatyspyt)
Dolomite
dolomitic limestone
Limey dolostone
Sandy limestone
Limstn (grainstone)
Limstn (laminite)
Chert
Silicilyte
Phosphorite
Evaporite
Conglomerate
Sandstone
Siltstone
Shale
Volcanic
Breccia
FISH RIV.
G.A.
NAB.
BRE.
STO.
NOM
SCHWARZRAND SUBGRP
URUSIS FM
SPITSKOP
undifferentiated
Feld.
HU.
NUD. FM
KUIBIS SUBGRP
ZARIS FM
Hoo.
Omkyk
Kl.
M.
DF
Kan
Zaris
Witputs
Mbr
max.
Max. age
Min. duration Nudaus
SPIE
A0?
OME
BANE
Ara Group
A6 A5 A4 A3 A2 A1 A0
Buah Fm?
A4
A3
A0?
Mexico
Nevada
California
W Canada
PUERTO BLANCO
CERRO RAJON
LA CIENEGA
CAMPITO
DUNFEE
ESMERALDA GP
STIRLING QRTZ.
WOOD CANYON
SEKWI
VAMPIRE
BACKBONE RANGES
INGTA
RISKY
Nadaleen River area
ALGAE
BLUEFLOWER
IV
3p
2p
1n
0n
A4?
A3?
ADOUDOU FM - TIFNOUT MBR
LIE DE VIN
IGL
TAM
TA
III
II
6p
5p
4.5p
4p
Olekma
Aldan River
Khorbusuonka River
Kotuykan River
Sukharikha
Yudoma River
PESTROTSVET
PEROKHTAKH
MATTAIA
SYHARGALAKH
SERALAKH
TURKUT
Dikimdya
UST-YUDOMA
AIM
KHATYSPYT?
NOKH
Nokhtuysk
LINNAYA
MEDVEZH.
MANYKAI
S. RECHKA
KRASNY POROG
SUKHARIKHA
V
IV
III
II
6p
5p
4p
3p
2p
1n
1p
0n
A4?
A3?
A0?
KHAIRK.
SALAAGOL
BAYANGOL
ZUUN-ARTS
or A4?

Fig. 5. High-resolution age model correlation by region for Model C only. Grey shading represents intervals of greatest uncertainty (see text for details). As in Fig. 3, the excursion marked as 1n represents the BACE. See Fig. S2 for a high resolution version of this figure.

Model C is our preferred correlation when considering best fit between sections that host continuous Fortunian $\delta^{13}C_{carb}$ data, whereby dominantly negative $\delta^{13}C_{carb}$ values are interrupted by short-lived positive excursions (Kouchinsky et al., 2007; Maloof et al., 2010) (e.g. Morocco, Siberia, Figs. 3d, e and 6). This model also permits a short-lived pre-BACE excursion (herein termed 0n) which is recorded in sections with high-resolution $\delta^{13}C_{carb}$ data from Morocco (e.g. Oued Sdas and Oued n'Oulili sections, Maloof et al., 2005), Siberia (Sukharikha and Nokhtuysk sections, Kouchinsky et al., 2007; Pelechaty, 1998), Mongolia (Zavkhan terrane, Smith et al., 2015), and possibly Laurentia (Hodgin et al., 2020; Smith et al., 2016) (Figs. 5 and 6).

Model C also maintains near constant sedimentation rates in multiple Fortunian – Stage 2 sections (Table S2). Taking two of the most continuous carbonate successions known with limited facies variation**,** Sukharikha River, Siberian Platform, and Zawyat n'Bougzoul, Morocco, we show that while Models A and B both show markedly declining sedimentation rates in both successions, Model C maintains a constant sedimentation rate (Fig. 6). At the resolution of lithostratigraphic detail afforded for each of these sections in the published literature, Model C appears to be the simplest and most parsimonious solution.

The maximum age for the regional FAD of *T. pedum* on the Kalahari Craton is associated with the radiometric age of the lower Nomtsas Formation, Namibia (Linnemann et al., 2019). We note,

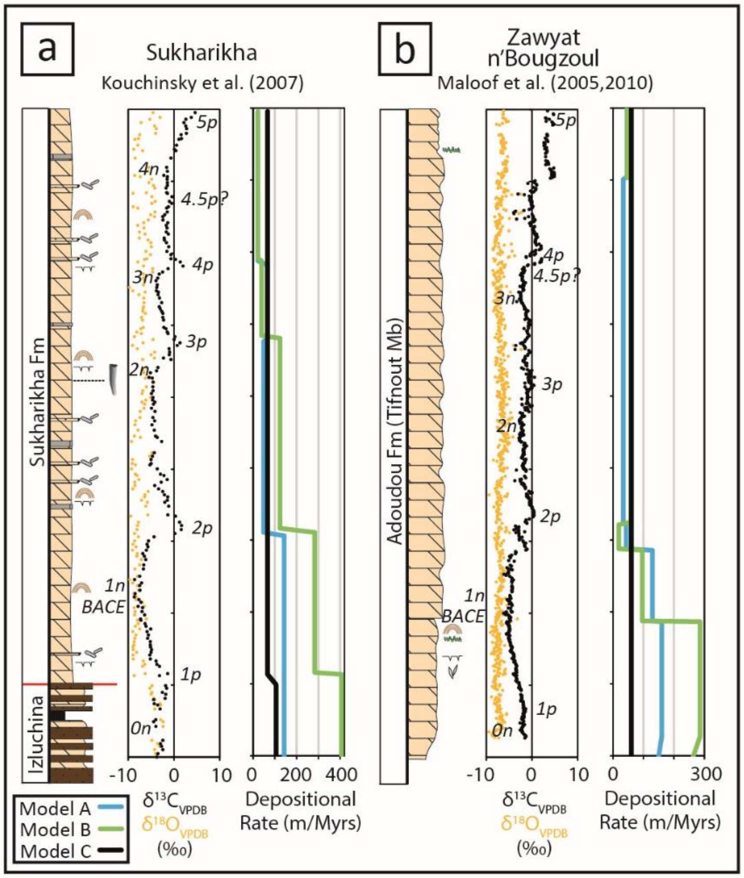

Fig. 6. Changes in sedimentation rate implied by models A to C for selected sections that capture the BACE and show limited facies variation through continuous carbonate successions. (a) Sukharikha River section (Igarka-Norilsk Uplift, Siberian Platform) and **(b)** Zawyat n'Bougzoul section (Anti-Atlas, Morocco), with lithostratigraphy and $\delta^{13}C_{carb}$ after Kouchinsky et al. (2007) and Maloof et al. (2005), respectively. See Fig. 2 for key to lithology and sequence stratigraphy.

however, that *T. pedum* has not been reported from the section (Farm Swartkloofberg, Linnemann et al., 2019) from which this radiometric age is derived. Instead, the FAD of *T. pedum* is reported from entirely siliciclastic valley fill deposits of the Nomtsas Formation on Farms Sonntagsbrunn and Vergelee, >100 km to the east of Farm Swartkloofberg (Table S3). By contrast, the FAD of *T. pedum* in Laurentia is well constrained above the nadir of the BACE recorded in carbonate interbeds of the Esmeralda Member of the Deep Spring Formation, Nevada (Fig. 5c, Smith et al., 2016). If Model C is correct, then the integrated $\delta^{13}C_{carb}$ chemostratigraphy and biostratigraphy of the Mount Dunfee section may imply a far younger age for the FAD of *T. pedum* (~535.5 Ma), and by extension the Ediacaran-Cambrian boundary, than currently defined (Fig. 5). This may therefore also support a case for repositioning the Ediacaran-Cambrian GSSP to the Mount Dunfee section based on the best-fit calibration of the FAD of *T. pedum*.

5. Ongoing uncertainties and biostratigraphic constraints

The process of constructing these age models has exposed the largest remaining uncertainties in late Ediacaran – early Cambrian stratigraphic correlation, which occur mainly due to insufficient radiometric control. Despite these uncertainties, we build on the biostratigraphic framework of Maloof et al. (2010) and constrain the FADs of key Cambrian-type small skeletal fossil groups within each age model (Table S2).

5.1 The possibility for a multimodal $\delta^{13}C_{carb}$ record

High resolution $\delta^{13}C_{carb}$ and sequence stratigraphic assessment of Cryogenian and early Ediacaran carbonates of the Congo Craton has revealed significant facies-dependency in the expression of presumed-global $\delta^{13}C_{carb}$ excursions (Hoffman and Lamothe, 2019). In their model, Hoffman & Lamothe (2019) propose that the observed multimodal $\delta^{13}C_{carb}$ expression between inner platform, basin margin and upper foreslope carbonates may be associated with significant facies-dependent distinction relating to seawater vs sediment-buffered diagenesis. They note that this may significantly complicate the utility of $\delta^{13}C_{carb}$ chemostratigraphic studies throughout geological time, especially where radiometric anchor-points are absent or sparse. Anomalously positive $\delta^{13}C_{carb}$ values of the middle Bambuí Group of Brazil, stratigraphically above *Cloudina*-bearing carbonates, also clearly demonstrate offset from global seawater composition (Uhlein et al., 2019). This offset is interpreted to reflect local effects of unusual water column chemistry that likely result from partial restriction (Cui et al., 2020b; Uhlein et al., 2019).

In our models, a number of regions show a degree of scatter in $\delta^{13}C_{carb}$, with possible evidence for deviation from the idealized seawater $\delta^{13}C_{carb}$ curve. Examples include the Zuun-Arts and Salaany Gol formations (Mongolia), and potential $\delta^{13}C_{carb}$ bimodality between different facies across the Yangtze Block (South China). In particular, the negative excursions at ca. 546.5 Ma (A0) and 541 Ma (A4), which may be globally widespread, are significantly muted in sections of the Yangtze Block. Whether the excursions themselves, or the muted record in South China, best reflect true changes in seawater composition as opposed to degrees of diagenetic alteration or restriction, remains uncertain.

Resolving the possible multimodal nature of Ediacaran and lower Cambrian $\delta^{13}C_{carb}$ records will benefit from future radiometric calibration, in addition to high-resolution studies of integrated stratigraphic, petrographic, $\delta^{44/40}Ca$ and $\delta^{26}Mg$ analyses (e.g. Ahm et al., 2021; Bold et al., 2020). Whilst this frustrates the utility of the proposed global $\delta^{13}C_{carb}$ correlation for regional chemostratigraphic studies of unfossiliferous strata with limited radiometric constraints throughout this time interval, we note that it does not alter proposed FADs and LADs of key taxa. We tentatively suggest that the broad trends observed in $\delta^{13}C_{carb}$ represented by gradual, unidirectional shifts in $\delta^{13}C_{carb}$, are consistent between sections but that the absolute magnitude of positive and negative excursions may differ depending on the specifics of local diagenetic alteration and/or steepness of the local isotopic gradient of seawater during organic carbon remineralisation. We note that this assumption holds true even for the Cryogenian interglacial interval, with the possible exception of the interval recording the Taishir anomaly (Hoffman and Lamothe, 2019). In this regard, and given the stratigraphic alternatives considered herein (Fig. 2), we do not consider the stable, positive $\delta^{13}C_{carb}$ data of the Swartpunt section to necessarily correlate with the nadir of the BACE, as has previously been suggested (e.g. Hodgin et al., 2020).

5.2 Age of the base of the Dengying Formation

In models A to C, the shape of the global composite $\delta^{13}C_{carb}$ curve between ~547 Ma and 543 Ma is dictated in large part by the age of the base of the Dengying Fm of the Yangtze Platform, South China, and the shape of the Dengying Fm $\delta^{13}C_{carb}$ profile. Detailed litho-, chemo-, and sequence stratigraphic studies of the Ediacaran Yangtze Platform are numerous (e.g. An et al., 2015; Condon et al., 2005; Cui et al., 2016; Cui et al., 2019; Ishikawa et al., 2008; Li et al., 2013; Lu et al., 2013; Tahata et al., 2013; Wang et al., 2014, 2017; Yang et al., 2021; C. Zhou et al., 2017b; Zhu et al., 2007, 2013). A summary description of the Dengying Fm, and detailed section correlation figures (Figs. S3 and S4) are provided herein for reference.

The Dengying Fm is lithostratigraphically subdivided into three members, each of which have differing names that correspond to geographic position on the Yangtze Platform (Fig. S3). The lower Member is dominated by dolostone that was deposited during a sea level highstand atop black shale of Member IV of the Doushantuo Formation (Zhu et al., 2007). This unit corresponds to the Algal Dolomite and Donglongtan members on the shallow Yangtze platform to the north and west, respectively, where it reaches thicknesses of >280m. In the Yangtze Gorges area to the east, the equivalent Hamajing Member ranges in thickness from 3-60m in sections measured for

$\delta^{13}C_{carb}$ (Fig. S3), but may reach a maximum thickness of 200m (Jiang et al., 2007; Zhu et al., 2007).

A sequence boundary separates dolostone of the lower Dengying Fm from overlying fossiliferous deeper marine deposits of the middle Dengying Fm across the Yangtze Platform (Zhu et al., 2007). In the north, this unit corresponds to fossiliferous transgressive siliciclastics and limestones of the Gaojiashan Member (20-45m) (Cui et al., 2016; Cui et al., 2019; Zhu et al., 2007). Equivalent transgressive deposits of the middle Dengying Fm correspond to shale of the Jiucheng Member (20-45m) in the west, and bituminous limestone of the richly fossiliferous Shibantan Member (up to >100m) in the Yangtze Gorges area to the east (Duda et al., 2016; Xiao et al., 2020; Zhu et al., 2007).

The third and topmost Member of the Dengying Fm is composed of highstand systems tract dolostones, which are frequently capped by a sequence boundary that shows evidence for exposure. In the north and west, this unit corresponds to the Beiwan (25-370m) and Baiyanshao (≤120m) members, respectively, which correlate with the Baimatuo Member (≤400m) in the Yangtze Gorges area (Zhu et al., 2007). Zircons within an ash layer 45m above the base of the Baimatuo Member at the Zhoujiaao section (central south Huangling anticline, Fig. S1) have been dated by U-Pb SIMS to 543.40 ± 3.5 Ma (Huang et al., 2020).

A zircon U-Pb CA-ID-TIMS age of 550.14 ± 0.63 Ma (Yang et al., 2021) from an ash bed at the top of Member IV (Miaohe Member) of the Doushantuo Fm at Jiuqunao section of the western Huangling anticline (Fig. S3) is classically considered to constrain a maximum age for the base of the Dengying Fm (Condon et al., 2005). The Dengying Fm in the Jiuqunao section records recovery from a negative $\delta^{13}C_{carb}$ excursion characterised by increasing $\delta^{13}C_{carb}$ from -4.05‰ to +3.56‰ in <3m of dolostone (Fig. S3) (Condon et al., 2005; Yang et al., 2021; Zhu et al., 2007).

Unfortunately, lithostratigraphic and chemostratigraphic correlation between sections of the western Huangling anticline at the boundary between the Doushantuo and Dengying formations is complicated by slumping and associated stratigraphic repetition (Fig. S3) (An et al., 2015; Vernhet, 2007; Yang et al., 2021; Zhou et al., 2017b). Furthermore, the ~550 Ma ash layer at Jiuqunao section has not been reported at the top of Doushantuo Member IV, or elsewhere, from any other section on the Yangtze Platform to date.

Here we consider a further alternative model (Model D) that explores the implications of correlating the $\delta^{13}C_{carb}$ data above the 550 Ma ash bed at Jiuqunao with the upper Hamajing Mb, rather than the basal Hamajing Mb (Fig. S4). In this model, the 550 Ma ash layer represents the age of slumping in the western Huangling anticline, and was deposited at the top of the disrupted unit, thereby permitting a conformable contact between the ash horizon and the overlying Dengying Fm at Jiuqunao section. The sequence stratigraphic framework for the entire Dengying Fm in sections across the Yangtze Platform and slope presented by Zhu et al. (2007) is maintained in Model D. However, this model implies that the thick Algal Dolomite and Donglongtan members, and the Hamajing Mb in many sections of the central and eastern Huangling anticline, were deposited between ≤565 Ma and ~550 Ma, rather than <550 Ma.

The alternative correlation presented in Model D greatly simplifies the global $\delta^{13}C_{carb}$ curve between 546 Ma and 543 Ma and, by extension, between 550 Ma and 541 Ma (Fig. 7). In models A-C, the $\delta^{13}C_{carb}$ profile from the (e.g.) Gaojiashan Member occupies the interval from 546 Ma to 543 Ma, however in Model D the middle Member of the Dengying Fm across the Yangtze Platform correlates well with the $\delta^{13}C_{carb}$ profile of the Kuibis Subgroup of the Nama Group, between 550

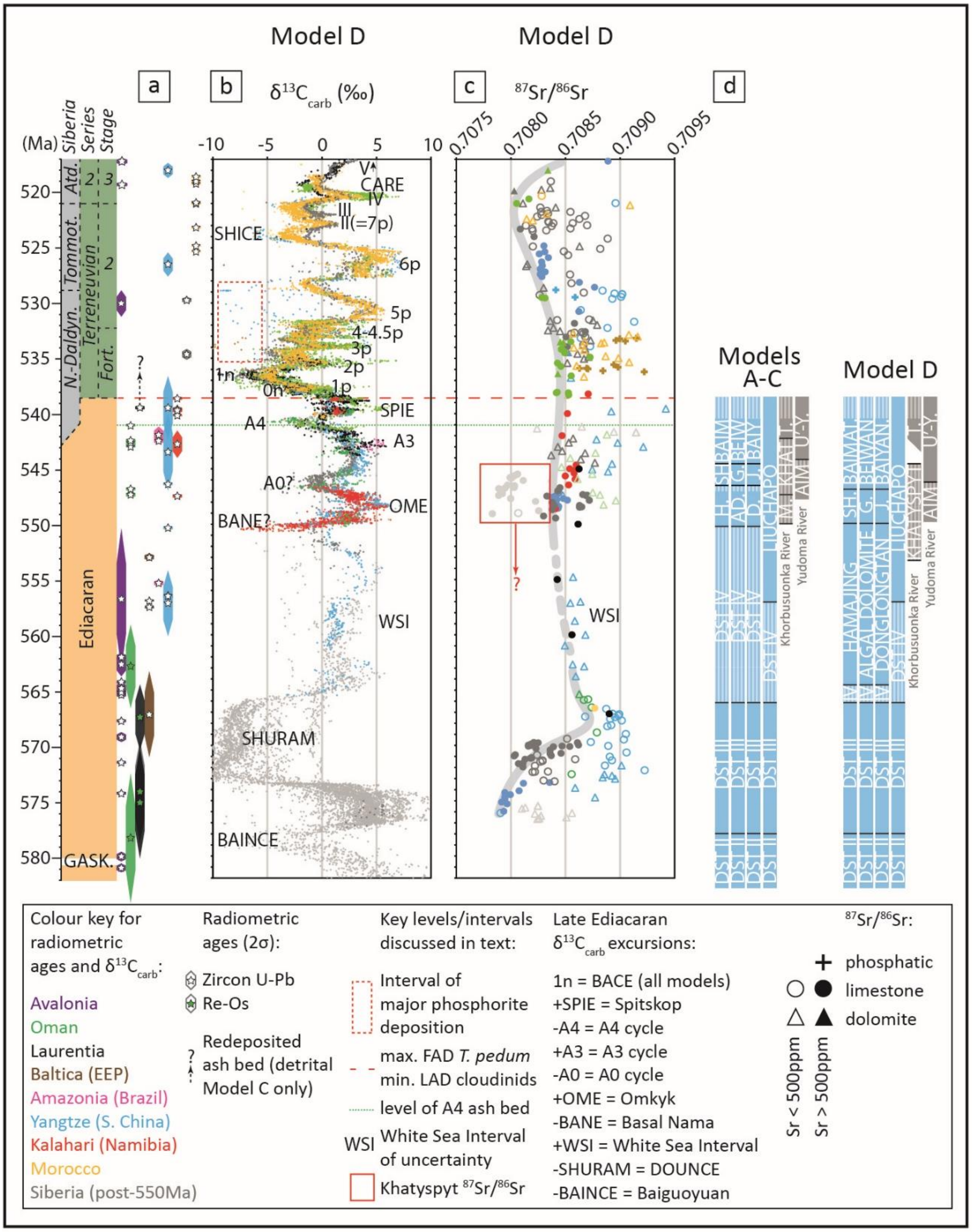

Fig. 7. Model D output resulting from correlation of the ~550 Ma ash layer at the Jiuqunao section with the upper Hamajing Mb and equivalent units of the lower Dengying Fm (see Fig. S4). Age model from 541-517 Ma is consistent with Model C, and age model for 582–550

Ma interval in grey after Yang et al. (2021). A) Radiometric ages with associated 2σ uncertainty, **B)** Global $\delta^{13}C_{carb}$ profile resulting from Model D correlation, **C)** Global $^{87}Sr/^{86}Sr$ profile resulting from Model D correlation, **D)** Summary of differences in stratigraphic correlation between models A-C and Model D for stratigraphy of South China (blue) and Siberia (grey). SH = Shibantan, G = Gaojiashan, J = Jiucheng, BAIMAT = Baimatuo, BAIYAN = Baiyanshao, M = Mastakh, T = Turkut, U'-Y = Ust'-Yudoma.

Ma and 546 Ma. Model D also implies that the Aim and Khatyspyt formations of the Siberian Platform may similarly occupy the interval from 550 Ma to 546 Ma based on best fit with the resulting global $\delta^{13}C_{carb}$ curve (Fig. 7d). In Model D, the global $\delta^{13}C_{carb}$ curve between 546.5 Ma and 541 Ma is characterised by a simple increase and decrease (Fig. 7b), from A0 to A3 and culminating in the A4 excursion (which may or may not correspond with the BACE).

5.3 Age of the Khatyspyt Formation

The temporal placement of the Khatyspyt Formation of the Olenek Uplift is key to understanding the degree of assemblage overlap between the Avalon, White Sea and Nama assemblages, as it contains typical Avalon assemblage fossils including the rangeomorphs *Charnia masoni* and *Khatyspytia grandis* (e.g. Cui et al., 2016). The age of the Khatyspyt Formation also has significant implications for the evolution and morphological changes in macroalgae during the late Ediacaran (Bykova et al., 2020). The Khatyspyt Formation has long been assumed to record deposition between ca. 560 and 550 Ma, approximately contemporaneously with the Miaohe Member and fossiliferous deposits of the White Sea area (e.g. Cui et al., 2016). In fact, the only radiometric constraint available is a maximum age for intrusion of the volcanic breccia of the Tas-

Yuryakh volcanic complex within the lower part of the Syhargalakh Formation (lower Kessyusa Group), which unconformably overlies the Khatyspyt and overlying Turkut formations. The maximum age for intrusion of this unit is 542.8±1.30 Ma, provided by zircon U-Pb air abrasion ID-TIMS (Table S1) (Bowring et al., 1993; Maloof et al., 2010; Rogov et al., 2015). Notwithstanding uncertainties in this age (Table S1), the Turkut Formation, which overlies the Khatyspyt Formation, contains the local FAD of the anabaritid *Cambrotubulus decurvatus* and the onset of a negative excursion which may be equivalent either to the A4 anomaly or the BACE (depending on the preferred model, Figs. 3 and 4). Screened $^{87}Sr/^{86}Sr$ data for the Khatyspyt Formation (boxed data in Fig. 4b-d) are notably depleted (mean = 0.708038, n = 19, Cui et al., 2016; Vishnevskaya et al., 2017, 2013) relative to all screened data prior to the nadir in upper Cambrian Stage 2 (Table S2). Recent efforts to produce a global late Ediacaran $^{87}Sr/^{86}Sr$ compilation suggest that the low $^{87}Sr/^{86}Sr$ data recorded by the Khatyspyt Formation are supportive of a temporal placement approximately coincident with and postdating data from the Nama Group (Cui et al., 2020a). Potential issues with this correlation are outlined below.

Carbon isotope data from the Nama Group are anchored at various levels to high precision radiometric ages (e.g. Bowring et al., 2007; Linnemann et al., 2019), and reveal trends in $\delta^{13}C_{carb}$ that are correlatable in other, globally distributed and similarly temporally well-constrained sections (e.g. Ara Group, Oman, Amthor et al., 2003; Bowring et al., 2007). Robust $^{87}Sr/^{86}Sr$ data from the Nama Group are recorded from samples spanning the Omkyk Member (Zaris Formation) to the Nomtsas Formation, with relatively invariable $^{87}Sr/^{86}Sr$ values (mean = 0.708538, n = 11) (Kaufman et al., 1993). Furthermore, high Sr limestones from the Shibantan Member, South China and the Zuun-Arts and overlying Bayan-Gol formations of the Zavkhan Terrane, Mongolia, show robust $^{87}Sr/^{86}Sr$ values and $\delta^{13}C_{carb}$ trends consistent with the record from the Nama Group, with the latter extending relatively stable values of ~0.708500 into the lower Fortunian (Fig. 4b-d, Table S2, Brasier et al., 1996). In light of available robust $\delta^{13}C_{carb}$ and $^{87}Sr/^{86}Sr$ data from radiometrically well-constrained sections, our compilation suggests either: 1) that low $^{87}Sr/^{86}Sr$ values and an Avalon-type biotic assemblage support an older temporal placement for the Khatyspyt Formation than that shown in our compilation (>551 Ma and possibly as old as ~575 Ma), or 2) that the $^{87}Sr/^{86}Sr$ data recorded by the Khatyspyt Formation are not representative of global seawater composition. The nature of the contact between the Khatypsyt and Turkut formations along the Khorbusuonka River is key to determining the true placement of the Khatyspyt Formation, and reports vary considerably. For example, Cui et al. (2016) report that the boundary between the Khatyspyt and Turkut formations is conformable, whereas Vishnevskaya et al. (2017) suggest that this is an unconformable contact. However, neither publication provides figured evidence of the nature of the contact.

In our correlation, we tentatively assume that the hiatus (if any) at the boundary between these two formations along the Khorbusuonka River is relatively minor (<500 kyrs). This is justified in part by the consistency in $\delta^{13}C_{carb}$ and lithostratigraphy between late Ediacaran sections of the Olenek uplift and the Nama and Ara groups (Figs. 3 and 5). However, we stress that this requires future clarification due to the unusually low $^{87}Sr/^{86}Sr$ data of the Khatyspyt Formation in this time interval. If the boundary is conformable, the presence of Avalon-type fossils in the Khatyspyt Formation, in addition to *Charniodiscus* noted from the Shibantan Member (Chen et al., 2014), together suggest that rare remnants of the Avalon assemblage remained until possibly as late as ca. 545.5 Ma. It is noteworthy that ordination plots of the overall late Ediacaran fossil assemblages have not placed the Khatyspyt assemblage within the Avalon-type biotas and instead place it with the younger White Sea biota (Boag et al., 2016). The temporal overlap between the Avalon and

Nama assemblages also holds true regardless of the age of the Khatyspyt Formation, as the age of the Shibantan Member is confidently constrained (< ca. 551 Ma) by the aforementioned radiometric age of the volcanic tuff deposit in the underlying upper Miaohe Member (Condon et al., 2005; Schmitz, 2012; Yang et al., 2021).

5.4 Age of the Turkut Formation:

A maximum age for intrusion of the Tas-Yuryakh volcanic breccia within the lower Syhargalakh Formation (lower Kessyusa Group) along the Khorbusuonka River is suggested by a zircon U-Pb air abrasion ID-TIMS age of 542.8 ± 1.30 Ma (Table S1) (Bowring et al., 1993; Maloof et al., 2010; Rogov et al., 2015). The intrusive Tas-Yuryakh volcanic breccia unconformably overlies the Turkut Formation. The FAD of the anabaritid *Cambrotubulus decurvatus* is recorded from the lower Turkut Formation in this section (Rogov et al., 2015), which supports a late Ediacaran lower boundary for the regional Nemakit-Daldynian Stage of Siberia, consistent with biostratigraphy and $\delta^{13}C_{carb}$ chemostratigraphy in sections along the Yudoma River of SE Siberia (Zhu et al., 2017). $\delta^{13}C_{carb}$ chemostratigraphic and sequence stratigraphic studies support temporal placement of the Turkut Formation of the Khorbusuonka River correlative with the middle – upper Ust'-Yudoma Formation in sections along the Yudoma River (Knoll et al., 1995; Pelechaty, 1998; Pelechaty et al., 1996b, 1996a; Zhu et al., 2017). Indeed, if the age of the Tas-Yuryakh volcanic breccia is close to the minimum age within analytical uncertainty, then the negative excursion recorded at the top of the Turkut Formation (Knoll et al., 1995) is equivalent to the A4 anomaly, and either corresponds with (Model A) or precedes (models B and C) the BACE. In both scenarios, the lower Turkut Formation and middle Ust'-Yudoma Formation at Kyra-Ytyga contain the earliest known FADs of anabaritids globally (≥541 Ma, Fig. 8). It is likely that future high precision CA-ID-TIMS analyses significantly alter the temporal position of the Tas-Yuryakh volcanic breccia, and by extension the minimum age of the underlying Turkut Formation. In the age models presented herein, a maximum age for the FAD of SSFs of the *Anabarites trisulcatus – Protohertzina anabarica* Zone (and by extension the Nemakit-Daldynian lower boundary) is therefore set at ca. 541–542 Ma across the Siberian Platform (Fig. 8). This temporal placement is most consistent with the dominant $\delta^{13}C_{carb}$ trends observed pre-BACE, whereby positive $\delta^{13}C_{carb}$ values are interrupted by short-lived negative excursions (Fig. 3e).

5.5 Integrated geochronology of the Ara Group

A complication inherent in the chemostratigraphic assessment of the Ara Group is the nature of the carbonate units themselves, which are found as ‘stringers’, frequently interbedded by evaporite (Amthor et al., 2003; Bowring et al., 2007). We note that whilst the high precision radiometric ages provided by Bowring et al. (2007) confidently place these carbonate units in relative stratigraphic order, the analysed tuffaceous material and $\delta^{13}C_{carb}$ datasets do not always derive from the same core. For example, the A0 $\delta^{13}C_{carb}$ excursion is recorded within the Sabsab-1 well, whereas the radiometric constraint of ~546.72 Ma derives from a tuff bed in the Asala-1 well. $\delta^{13}C_{carb}$ data for the Asala-1 well remain unpublished, precluding confident calibration of this $\delta^{13}C_{carb}$ excursion. Indeed, the only two wells for which both radiometric and $\delta^{13}C_{carb}$ data are available are BB-5 and Minha-1. Whilst BB-5 constrains the A4 anomaly, Minha-1 captures positive $\delta^{13}C_{carb}$ values in the A3 Member that are in agreement with radiometrically constrained $\delta^{13}C_{carb}$ data from Brazil (Parry et al., 2017) and South China (Huang et al., 2020).

We note that some other globally-distributed sections record an excursion that is demonstrably pre-BACE (e.g. Zuun-Arts Formation), which may be more consistent with an earlier, distinct 'A4' anomaly. The A5 Member of the Ara Group also records a $\delta^{13}C_{carb}$ plateau of similar magnitude to that recorded at Swartpunt (Figs. 5a, b), followed by a gradual decrease in $\delta^{13}C_{carb}$ that mirrors the decrease seen above the level of the ca. 539.6 Ma horizon at Swartpunt (Figs. 2 and 5a, b). These features may add credence to a pre-BACE 'A4' anomaly (models B and C).

5.6 $\delta^{13}C_{carb}$ correlation of the lower Fortunian

Recent biostratigraphic and $\delta^{13}C_{carb}$ chemostratigraphic assessment of Ediacaran – Cambrian transitional strata of the Yangtze Platform, South China have shown a previously underappreciated level of $\delta^{13}C_{carb}$ variability in the post-BACE, pre-ZHUCE (Zhujiaqing positive $\delta^{13}C_{carb}$ excursion) interval (Steiner et al., 2020). In age models A and B, the BACE is constrained to be late Ediacaran in age, with a nadir either at ca. 541 (Model A) or ca. 539 Ma (Model B, Figs. 3 and 9, Table S2). In Model C, the BACE is within the basal Cambrian based on correlation with the radiometric age and inferred maximum FAD of *T. pedum* in the Nomtsas Fm (Fig. 10). However, as noted above, the FAD of *T. pedum* is constrained to be post-BACE in all successions that host the BACE, which may also support an Ediacaran age for the BACE in Model C. The BACE is well-recorded in sections across the Yangtze Platform, South China, in the lower Zhujiaqing Formation (Daibu Member) and Yanjiahe Formation, and is commonly overlain by phosphorus-rich carbonates of the middle Zhujiaqing Formation (Zhongyicun Member) and equivalent units (Brasier et al., 1990; Steiner et al., 2020). Phosphorite deposition is globally widespread in lower Fortunian strata (e.g. Tarim, Yangtze Platform, Malyi Karatau of Kazakhstan, northern Mongolia, some sections of Laurentia), with carbonate substituted in the phosphorite lattice commonly recording very negative, or highly variable $\delta^{13}C_{carb}$ values that diverge from global seawater composition. The upper Yanjiahe Formation, above the level of the BACE, yields highly variable $\delta^{13}C_{carb}$ values alongside SSFs of the *A. trisulcatus – P. anabarica* assemblage Zone (Steiner et al., 2020). The Kuanchuanpu Formation yields similarly variable $\delta^{13}C_{carb}$ values and SSFs (Steiner et al., 2020; B. Yang et al., 2016). Crucially, the lower Kuanchuanpu Formation records the co-occurrence of *Cloudina* with SSFs of the *A. trisulcatus – P. anabarica* Zone (B. Yang et al., 2016), however the exact position of this mixed assemblage relative to the BACE nadir remains uncertain.

In areas where phosphorite deposition is limited, the $\delta^{13}C_{carb}$ composition of Fortunian-age global seawater is more faithfully recorded (e.g. Siberia, Morocco, Mongolia), and appears to show high frequency excursions (including peaks 2p-4p) that record a gradual increase in $\delta^{13}C_{carb}$ towards a large positive excursion (5p) (Figs. 3b-d, 5d-f) (Kouchinsky et al., 2007; Maloof et al., 2010; Smith et al., 2015). Crucially, however, this interval of high frequency $\delta^{13}C_{carb}$ variability suffers from a significant dearth of radiometric anchor-points, robust differentiation in SSF zonation, or differentiation of $\delta^{13}C_{carb}$ peaks of distinct magnitude. Sections of the Anti-Atlas Mountains in Morocco and along the Sukharikha River of northwest Siberia have been proposed as continuous reference sections for correlative trends in Fortunian global seawater $\delta^{13}C$ (Kouchinsky et al., 2007; Maloof et al., 2010). However, the absolute magnitude and number of peaks are thought to vary between and within regions (e.g. Smith et al., 2015). At present, the published section information in both of these areas is insufficiently detailed to accurately constrain the position of individual exposure surfaces. We note that the Fortunian remains the interval of greatest uncertainty in our correlation and demands future targeted study, integrating high resolution chemostratigraphic data with detailed sedimentological, biostratigraphic and sequence stratigraphic information and, where possible, high resolution radiometric age constraints. Higher resolution $\delta^{13}C_{carb}$ datasets may also permit more statistically significant peak correlation through use of dynamic programming algorithms, as has been demonstrated for Atdabanian successions of Morocco (Hay et al., 2019).

5.7 The position of the ZHUCE relative to peaks 5p and 6p

Below we consider alternative temporal positions for the ZHUCE and the excursion recorded in the Salaany Gol Formation. For ease of reference, alternative correlations are incorporated into Model A relative to models B and C, however their relative positions and uncertainties should be considered in isolation.

The upper Zhujiaqing Formation (Dahai Member) of the Yangtze Platform records a prominent positive $\delta^{13}C_{carb}$ excursion with an onset approximately coincident with the FADs of the mollusks *Aldanella attleborensis* and *Watsonella crosbyi* (Figs. 8-10, Table S3, Li et al., 2011; Parkhaev and Karlova, 2011; Steiner et al., 2020). The FAD of *Watsonella crosbyi* occurs prior to the apex of 5p, or immediately following recovery from 5p in sections of the western Anabar Shield, and may be approximately contemporaneous in the Bayangol Fm of the Zavkhan Terrane, Mongolia (Kouchinsky et al., 2017; Smith et al., 2015) (but see section 5.8). Peak 5p is followed by 6p in Cambrian Stage 2 strata of Siberia and Morocco, but the relative position of the singular excursion recorded in the Dahai Member has been problematic (Steiner et al., 2020). Possible regional variability in the magnitude of the ZHUCE in South China, in addition to widespread phosphorite deposition of the underlying Zhongyicun Member in some areas of the Yangtze Platform, complicates the utility of $\delta^{13}C_{carb}$ chemostratigraphy for accurately determining the correct correlation of the peak recorded in the Dahai Member (Steiner et al., 2020).

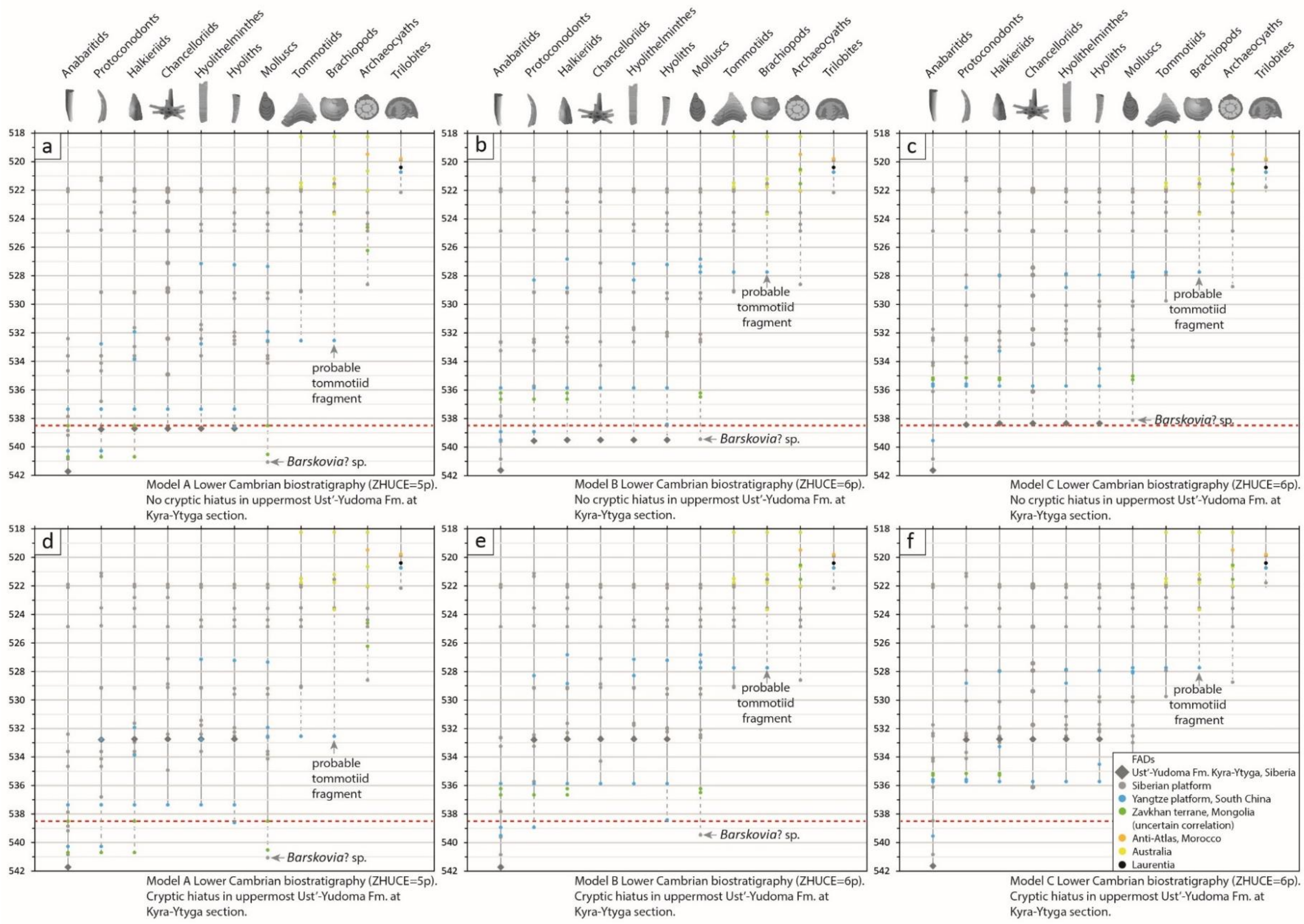

Model A Lower Cambrian biostratigraphy (ZHUCE=5p). No cryptic hiatus in uppermost Ust'-Yudoma Fm. at Kyra-Ytyga section.

Model B Lower Cambrian biostratigraphy (ZHUCE=6p). No cryptic hiatus in uppermost Ust'-Yudoma Fm. at Kyra-Ytyga section.

Model C Lower Cambrian biostratigraphy (ZHUCE=6p). No cryptic hiatus in uppermost Ust'-Yudoma Fm. at Kyra-Ytyga section.

Model A Lower Cambrian biostratigraphy (ZHUCE=5p). Cryptic hiatus in uppermost Ust'-Yudoma Fm. at Kyra-Ytyga section.

Model B Lower Cambrian biostratigraphy (ZHUCE=6p). Cryptic hiatus in uppermost Ust'-Yudoma Fm. at Kyra-Ytyga section.

Model C Lower Cambrian biostratigraphy (ZHUCE=6p). Cryptic hiatus in uppermost Ust'-Yudoma Fm. at Kyra-Ytyga section.

Fig. 8. High-resolution Cambrian biostratigraphy resulting from models A to C. Note that first occurrences are pinned only within sections that have high-resolution $\delta^{13}C_{carb}$ data. As such, first appearances within siliciclastic-dominated successions remain uncalibrated. The single specimen of *Aldanotreta* sp. (brachiopod) reported from the upper Zhongyicun Member (Table S2) may instead represent a tommotiid fragment; however, this cannot be confirmed due to the poor quality of the specimen.

Model A (Figs. 3b, 8a, 9b,c) shows the result of correlating the ZHUCE with 5p, which may be more consistent with a depositional hiatus of longer duration that separates the Dahai Member from the overlying Shiyantou Formation. In this correlation, the FAD of tommotiids in South China significantly predates Siberia (Fig. 8a), and maximum $\delta^{13}C_{carb}$ values of the Dahai Member are greater than 5p in the Siberian and Moroccan profiles. However, Model A results in a relatively consistent (possibly slightly earlier) FAD of the mollusks *Watsonella* and *Aldanella* relative to Siberia (Fig. 9c), whereas Model B results in a slightly delayed FAD of these genera in South China (Figs. 8b and 9f). The correlation of ZHUCE with 5p is also supported by SSF biostratigraphy of the Yanjiahe Fm, where peak values in Unit 3 occur within the SSF Zone 2 (*Purella antiqua*), which would be consistent with a pre-5p excursion in other localities.

In models B and C, the ZHUCE is correlated with peak 6p (Figs. 3c,d, 8b,c, 9f, 10c) and negative $\delta^{13}C_{carb}$ values associated with phosphatic lithologies of the Zhongyicun Member are not considered useful for global chemostratigraphic correlation. Correlation of the ZHUCE with 6p may be justified by the best fit of $\delta^{13}C_{carb}$ data (particularly maximum values at Xiaotan section), but also by recognition of the more consistent age for the resulting FAD of tommotiids in South

China relative to Siberia (Fig. 8b,c). In Model B, positive $\delta^{13}C_{carb}$ in Yanjiahe Unit 3 are correlated with peak 5p, and peak 6p is absent from this formation in recognition of the depositional hiatus separating the Yanjiahe Formation from the overlying Shuijingtuo Formation (Steiner et al., 2020). Robust differentiation between these correlations is currently hampered by a lack of radiometric data and discontinuous carbonate sections from this interval in South China.

5.8 Correlation of the Salaany Gol Formation (Zavkhan Terrane, Mongolia) with peak 6p vs peak IV

A basal Tommotian (Stage 2) age for the lower Salaany Gol (Salaagol) Formation of SW Mongolia was justified by Smith et al. (2015) on the basis of an absence of trilobites in this unit, which in their view makes the excursion equivalent to positive peak 6p of the Siberian scale (shown in Model A of Figs 3a, 8a, 9b). However, the archaeocyathan assemblage of the lower Salaany Gol Formation includes approximately 30 distinct species (up to 16 species per single reef; Zhuravlev and Naimark, 2005), which are widespread throughout Mongolian, Altay-Sayan and Transbaikalian terranes and occur permanently below the first trilobites in each area (Debrenne et al., 2015; Dyatlova and Sycheva, 1999; Osadchaya and Kotel’nikov, 1998; Zhuravleva et al., 1997). In turn, this first trilobite species assemblage is also the same and belongs to the *Resimopsis* trilobite Zone, which contains species of the middle Atdabanian (Stage 3) *Repinaella* trilobite Zone of the Siberian Platform and lacks any earlier trilobite elements (Astashkin et al., 1995; Korobov, 1989, 1980). Landing and Kruse (2017) noted these inconsistencies and suggested that the positive $\delta^{13}C_{carb}$ excursion in the lower Salaany Gol Formation is rather an equivalent of the middle Atdabanian $\delta^{13}C_{carb}$ excursion IV of the Siberian Platform, which fits better to both archaeocyath and trilobite biostratigraphies. The other suggestion of Smith et al. (2015) concerning the absence

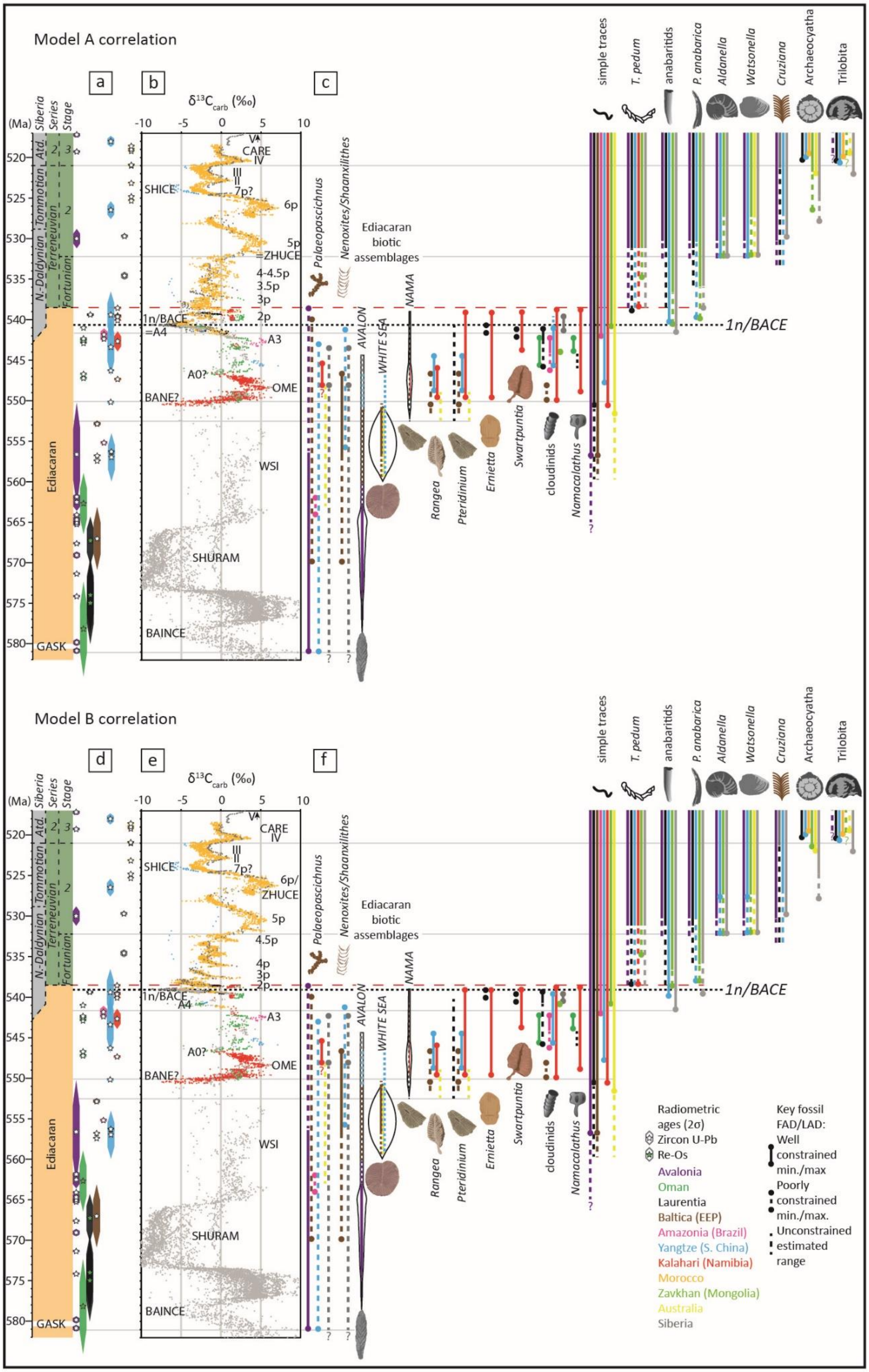
Model A correlation
a
b
c
(Ma)
Siberia
Series
Stage
δ13Ccarb (‰)
-10 -5 0 5 10
N.-Daldynian
Tommotian
Atd.
Terreneuvian
Fortunian
2
3
Ediacaran
GASK
V
CARE
IV
III
II
7p?
6p
SHICE
5p
=ZHUCE
4-4.5p
3.5p
3p
2p
1n/BACE
=A4
A3
A0?
OME
BANE?
WSI
SHURAM
BAINCE
Palaeopascichnus
Nenoxites/Shaanxilithes
Ediacaran biotic assemblages
AVALON
WHITE SEA
NAMA
Rangea
Pteridinium
Ernietta
Swartpuntia
cloudinids
Namacalathus
simple traces
T. pedum
anabaritids
P. anabarica
Aldanella
Watsonella
Cruziana
Archaeocyatha
Trilobita
1n/BACE
Model B correlation
d
e
f
6p/ZHUCE
4.5p
4p
A4
Radiometric ages (2σ)
Zircon U-Pb
Re-Os
Avalonia
Oman
Laurentia
Baltica (EEP)
Amazonia (Brazil)
Yangtze (S. China)
Kalahari (Namibia)
Morocco
Zavkhan (Mongolia)
Australia
Siberia
Key fossil FAD/LAD:
Well constrained min./max
Poorly constrained min./max.
Unconstrained estimated range

Fig. 9. Biostratigraphic output resulting from Model A (a–c) and Model B (d–f) for the interval ~551–517 Ma. Includes **(a,d)** radiometric constraints, **(b,e)** $\delta^{13}C_{carb}$, and **(c,f)** First Appearance Datum (FAD) and Last Appearance Datum (LAD) of key Ediacaran-Cambrian fossils (Table S3). Black dotted line marks the temporal position of the 1n/BACE nadir. Red dashed line marks the Ediacaran-Cambrian boundary as defined by the maximum age for the first appearance datum of *Treptichnus pedum*. Note that uncertainty remains in ichnofossil assignment of the traces in the Mistaken Point Formation of Avalonia (Warren et al., 2020).

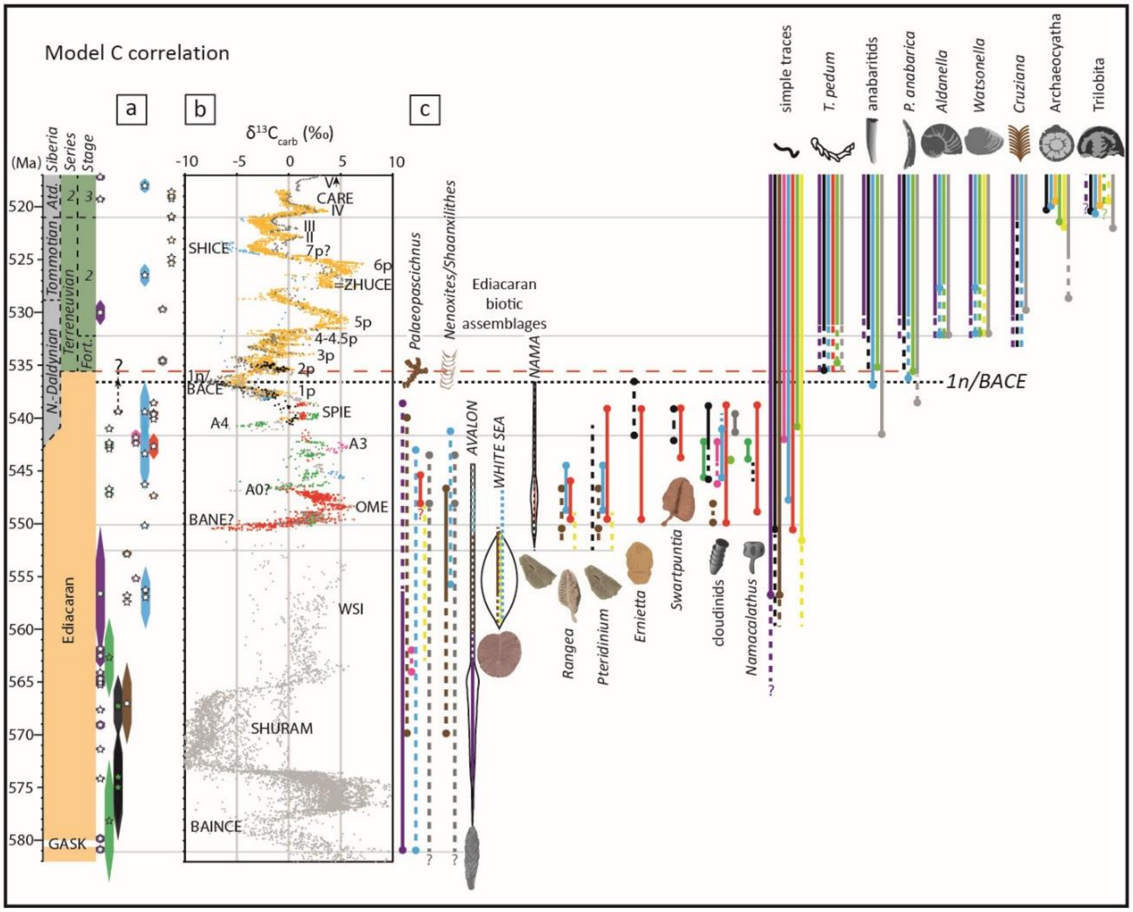

Fig. 10. Biostratigraphic output resulting from Model C (a–c) for the interval ~551–517 Ma. Includes **(a)** radiometric constraints, **(b)** $\delta^{13}C_{carb}$, and **(c)** First Appearance Datum (FAD) and Last Appearance Datum (LAD) of key Ediacaran-Cambrian fossils (Table S3). Black dotted line marks

the temporal position of the 1n/BACE nadir. Red dashed line marks the Ediacaran-Cambrian boundary as defined by the maximum age for the first appearance datum of *Treptichnus pedum*. In this figure, the FAD of *T. pedum* is interpreted to post-date the BACE nadir in all regions (max. FAD in upper Esmeralda Mb, Nevada, Fig. 5c), and the age of the lower Nomtsas Fm at Swartkloofberg section does not anchor the FAD of *T. pedum* in Namibia (see discussion in Section 4). Key provided in Fig. 9.

of upper Atdabanian and Botoman (stages 3 and 4) faunal elements from the Salaany Gol Formation is correct and supported by the restudy of archaeocyath species assemblage, which is the same through the entire formation (Cordie et al., 2019; Debrenne et al., 2015; Zhuravlev, 1998).

We agree with Smith et al. (2015) that the magnitude of the positive $\delta^{13}C_{carb}$ excursion reported from the Salaany Gol Formation fits well with peak 6p on the reference scale, but greatly exceeds the magnitude of peak IV (Figs. 3, 5f, Table S2). However, we also note that the regional $\delta^{13}C_{carb}$ record from the Zavkhan terrane throughout the underlying Zuun-Arts and Bayangol formations frequently exhibits more extreme values (positive and negative) relative to other late Ediacaran and lower Cambrian records from Siberia, Morocco and elsewhere. Models B and C (Figs. 3c,d, 8b,c, 9e,f, 10b,c) reposition the Salaany Gol Formation to the Atdabanian, with the uppermost Bayan Gol Formation occupying a position relative to peak 6p, and implies poor expression of peak 5p, possibly within lower Member BG5 of Smith et al. (2015) (Fig. 5f). We stress, however, that peak correlation throughout the Fortunian and Stage 2 of Mongolia, and globally, remains poorly constrained.

5.9 Age and correlation of Terreneuvian – Series 2 strata of Australia

The Arrowie and Stansbury basins contain a rich assemblage of lower Cambrian fossils, including the regional first appearance of archaeocyaths, trilobites, bradoriids and tommotiids. Betts et al. (2019, 2018, 2017a, 2017b, 2016) and Jago et al. (2020) refined the lower Cambrian biostratigraphy for South Australia developed by Daily (1990, 1972), Laurie (1986), Gravestock (1984), Bengtson et al. (1990), Zhuravlev and Gravestock (1994), and Gravestock et al. (2001) and added $\delta^{13}C_{carb}$ chemostratigraphy. Contrary to previous workers, Betts et al. (2019, 2018, 2017a, 2017b, 2016) and Jago et al. (2020) suggested that lower units of fossiliferous strata of the Arrowie and Stansbury basins be repositioned to stages 2 and 3 instead of stages 3 and 4, respectively. These justifications were mostly based on tommotiid biostratigraphy, with little reference to other biostratigraphic constraints. However, Australian tommotiids are highly endemic species and some genera are unknown even beyond the Australian-Antarctic faunal province of Gondwana, while other faunal elements, including archaeocyaths, trilobites, bradoriids, mollusks and brachiopods are much more widespread, although at the generic level (Bengtson et al., 1990; Betts et al., 2017b; Brock et al., 2000; Gravestock et al., 2001; Laurie, 1986). In dismissing the biostratigraphic value of archaeocyaths, for instance, these authors arrive at a correlation of their *Kulparina rostrata* tommotiid Zone and the regionally pre-trilobitic portion of their succeeding *Micrina etheridgei* Zone with the Cambrian Stage 2, even though these zones collectively coincide with the *Warriootacyathus wilkawillinensis*, *Spirillicyathus tenuis* and *Jugalicyathus tardus* archaeocyath zones (Zhuravlev and Gravestock, 1994), dated as Atdabanian in Siberian terms (Stage 3). Likewise, comparison of archaeocyath genera in common with South China indicates a correlation with trilobite-bearing upper Qiongzhusian-lower Canglangpuan (Stage 3) strata in that region (A. Yang et al., 2016). The same conclusions contradicting the correlations of Betts et al. (2018, 2017a) follow from analysis of the biostratigraphic distribution of any other fossil group present in these tommotiid-based zones, including bradoriids, brachiopods (Kruse et al., 2017) and mollusks (Parkhaev, 2019a). In general, tommotiids and coeval early small shelly fossils in South Australia are not indicative of the Terreneuvian because representatives of all other co-occurring fossil groups (archaeocyaths, bradoriids, brachiopods, mollusks) are restricted to post-Terreneuvian strata in Siberia, South China, Laurentia and other regions, and more precisely to global stages 3 and 4 (Kruse et al., 2017; Parkhaev, 2019a), which suggests different, younger ages for some of the $\delta^{13}C_{carb}$ peaks, rather than those accepted by Betts et al. (2018). In our correlation, we have repositioned some of these Australian $\delta^{13}C_{carb}$ data to maintain consistency with both the regional stratigraphic correlation of Betts et al. (2018) and biostratigraphic constraints that are more globally applicable (Figs. 9 and 10, Table S2).

6. Implications for macroevolutionary dynamics

Our revised correlations have important implications both for the late Ediacaran global $\delta^{13}C_{carb}$ profile and for macroevolutionary dynamics across the BACE interval. Combining the temporal and spatial distribution of major Ediacaran-Cambrian shelly and trace fossils into these new global $\delta^{13}C_{carb}$, $^{87}Sr/^{86}Sr$ and geochronological records, together with older Ediacaran radiometric dates, allows us to establish temporal and spatial paleobiogeographic trends that significantly diverge from the accepted consensus (Figs. 8-11; Table S3). These trends are robust despite remaining uncertainties, and crucially, all age models show the same macroevolutionary trends across the Ediacaran-Cambrian boundary interval (Figs. 8-10). Namely, that multiple negative $\delta^{13}C_{carb}$ excursions are present in the late Ediacaran record, which do not clearly correlate with extinction events and that SSFs of the *A. trisulcatus – P. anabarica* Zone appeared below the BACE.

The available radiometric age constraints for the interval of ~580–538 Ma confirm the temporal overlap of elements of the Avalon, White Sea and Nama assemblages of the Ediacaran biota, rather than forming discrete successive assemblages, with the White Sea assemblage being entirely transitional (Grazhdankin, 2014; Yang et al., 2021). Consistent with previous models, the Ediacaran biota show a marked decline in diversity ~550, and again ~545 Ma (Boag et al., 2016; Grazhdankin, 2014; Muscente et al., 2019). Elements of the Avalon and White Sea assemblages inhabited different basins contemporaneously in the White Sea and Podolia regions of Baltica, and Australia, until ~552 Ma (Gehling and Droser, 2013; Grazhdankin, 2014), although the age range of fossiliferous strata of the Ediacara Member remains poorly constrained. Both the Avalon and White Sea assemblages largely disappeared by ~550 Ma, however some elements of the Avalon assemblage (e.g. *Charniodiscus*) and White Sea assemblage (e.g. possible *Dickinsonia* sp.) were likely present until as late as ~545.5 Ma in South China and possibly northern Siberia (e.g. Xiao et al., 2020). After this time, taxa of the Nama assemblage remained present in the Nama Basin, Namibia, the Erga Formation of the White Sea region, the Shibantan Member of the Yangtze Block, South China, and the Wood Canyon Formation of Laurentia. Successions of Armorica (Spain) and SW Gondwana (Brazil and Paraguay) also host skeletal assemblages of *Cloudina*, *Namacalathus* and *Corumbella* (Adôrno et al., 2017; Cortijo et al., 2010; Warren et al., 2011), however these successions remain poorly constrained in time <550 Ma due to a dearth of high resolution $\delta^{13}C_{carb}$ data. Fossils of the *Palaeopascichnus* group may have extended below ~560 Ma in the Shuram-Wonoka negative excursion interval in South Australia. However, these taxa are known from ~547–545 Ma in Siberia (Aim Formation), South China (Gaojiashan and

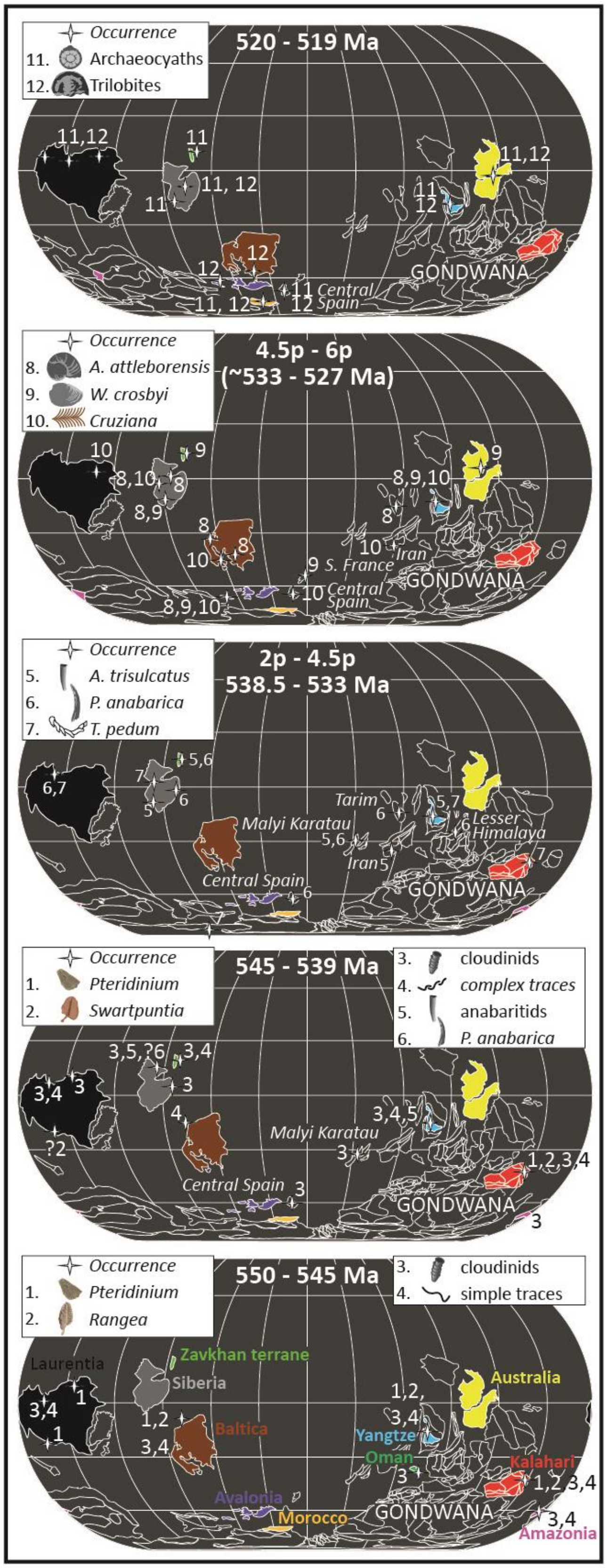

Fig. 11. Global paleobiogeography at intervals between ~551 and 517 Ma consistent with all age models with paleogeography after (Merdith et al., 2021)**.** Note that the positions of the Zavkhan terrane of Mongolia (bright green), Malyi Karatau of Kazakhstan, and Avalonian microcontinent in this interval remain uncertain (e.g. Landing et al., 2020). Craton coloring is consistent with stratigraphic and biostratigraphic ranges in Figs. 3-5, and 7-10.

Shibantan members, and Liuchapo Formation) and Namibia (Schwarzrand Subgroup), and may show their greatest range in eastern Newfoundland, where they are found below a Gaskiers age diamictite (>580 Ma) and even co-occur with *T. pedum* above the basal Cambrian GSSP (Table S3).

Treptichnid trace fossils pre-date the inferred nadir of the BACE in Namibia, and Cambrian-type shelly fossils of the *Anabarites trisulcatus – Protohertzina anabarica* Zone predate the nadir of the BACE in Siberia and predate or co-occur with the nadir of the BACE in South China (Cai et al., 2019; Jensen et al., 2000; Zhu et al., 2017). Diverse and complex ichnofossils also predate the *T. pedum* FAD in a number of sections (e.g. Chen et al., 2019; Gozalo et al., 2003; Jensen et al., 2000; Zhu et al., 2017). At least three soft-bodied genera of the Nama assemblage are present in the Nama Basin, Namibia, post-dating (Model A), coeval with (Model B), or pre-dating (Model C) the inferred position of the BACE, and both *Cloudina* and *Namacalathus* occur above the inferred recovery from the A4 anomaly in the same section in all models (Fig. 2, Darroch et al., 2015; Narbonne et al., 1997; Wood et al., 2015). There are currently no environments that show unequivocal co-occurrence of the Cambrian ichnospecies *T. pedum* and Ediacaran skeletal fossils *Cloudina* or *Namacalathus*. These taxa, as well as *Nenoxites* (= *Shaanxilithes* in South China) became extinct at or before the Ediacaran-Cambrian boundary, as defined by the FAD of *T. pedum*, but significantly these extinctions were regional, rather than global events (e.g. *Cloudina* LAD may be as early as ~542.3 Ma in Oman (Bowring et al., 2007), but occurred after ~539.6 Ma in Namibia (Linnemann et al., 2019)).

Model C may support a range extension for erniettomorphs in Laurentia associated with the BACE nadir, to an age that is within the lower Cambrian as presently defined (Figs. 5 and 10).

However, Model C may also imply a younger age for the FAD of *T. pedum* (and hence the Ediacaran-Cambrian boundary) if this ichnospecies is restricted to a position above the BACE recovery as suggested in multiple regions (Figs. 5 and 10, Table S3). The *T. pedum* FAD may show broadly synchronous origination at the boundary above recovery from the BACE, with a maximum radiometric age constraint of ~538.8 Ma (Linnemann et al., 2019). However, the first appearance of this ichnospecies is delayed in the Zavkhan terrane, and is not well constrained within the interval 538.8–532 Ma in Siberia, South China or the lower Cambrian boundary type section in Avalonia (Table S3). This pattern may be a consequence of local ecological, taphonomic and/or lithological controls.

The FADs of Ediacaran and Cambrian shelly fossils are also highly variable temporally and spatially (Figs. 8-10). The *Cloudina – Namacalathus* assemblage appeared ~550 Ma in the Nama Basin and became globally widespread, but asynchronously, thereafter. *Anabarites trisulcatus* and *Protohertzina anabarica* FADs, which are commonly recognized as the index fossils of the basal Cambrian strata, are in fact oldest in Siberia, where *Anabarites* co-occurs with *Cloudina* at a level below the BACE (Figs. 8-10) (Zhu et al., 2017), followed closely by the appearance of these taxa in South China (Cai et al., 2019). Cambrian-type skeletal fossils (halkieriids, chancelloriids, hyolithelminthes, hyoliths, archaeocyaths and many others) also appear highly asynchronously in different basins (Fig. 8).

By contrast, our compilation suggests that the appearance of *Watsonella* and *Aldanella* at ~532–531 Ma may have had a broadly synchronous appearance during the same interval on the global $\delta^{13}C_{carb}$ profile, however this remains dependent upon the correlation of the ZHUCE in South China (Figs. 8-10). The probability of a trilobite biomineralisation event at ~521–518 Ma is supported by the stratigraphic and paleogeographic distribution of arthropod scratch marks (e.g. *Rusophycus*, *Cruziana* and *Diplichnites*), which occur from ~531–525 Ma and pre-date the appearance of trilobites and other arthropods in almost every basin by several million years (Landing et al., 2020; Paterson et al., 2019). This biomineralisation event may have been driven by changing seawater chemistry (e.g. Mg/Ca ratios, $p\text{CO}_2$), causing a shift from aragonite to calcite seas (Porter, 2007).

These observations may imply two patterns of first appearance. In the first case, an animal or a group of animals appeared first in a single area and became globally widespread much later (e.g. Namibian shelly fossils including *Cloudina* and *Namacalathus*, Siberian archaeocyaths). The appearance of such organisms probably reflects local conditions most advantageous for their oxygen, calcium and other essential requirements. The second type of FADs embraces a broadly synchronous global appearance of the same group in remote regions (e.g. mollusks, trilobites). Such events can be attributed to global changes of environmental factors (e.g. $p\text{CO}_2$, Mg:Ca ion ratio) facilitating almost simultaneous biomineralisation of hitherto soft-bodied representatives of these groups in different basins, as noted in trilobites (Paterson et al., 2019).

We conclude that the Cambrian Explosion was in fact a protracted Ediacaran-Cambrian radiation. All models reveal widespread and correlatable late Ediacaran negative and positive $\delta^{13}C_{carb}$ excursions between ~550 Ma and the onset of the BACE. In contrast to previous studies (Amthor et al., 2003), our correlation demonstrates no significant extinction or faunal turnover coincident with the A4 anomaly, or any older negative carbon $\delta^{13}C_{carb}$ perturbation between 550 Ma and 540 Ma, but rather a series of successive, often regional, originations and minor extinctions. The canonical model (Model A) also implies that the disappearance of the Nama assemblage post-dated the BACE, whereas Model C may be compatible with a coincident disappearance of this assemblage with the BACE nadir. Regardless, the pre-BACE appearance of anabaritids and treptichnid traces in all models also argues against a mass extinction event coincident with the BACE.

While the near synchronous global appearance of trilobites may support a calcification (biomineralisation) event in this group (Landing et al., 2020; Paterson et al., 2019), the radiation of other skeletal biota was generally highly asynchronous, with varying tempos in different basins (Figs. 8-11). This may reflect both a diversity gradient formed by clade origination in low latitudinal basins (Siberia, Mongolia, Chinese and Namibian Gondwana) and then migration to higher latitudes (e.g. Avalonia, Morocco) (Fig. 11, e.g. Jablonski et al., 2006, but see Landing et al., 2020), and also a highly heterogeneous local landscape of redox and/or nutrient regimes. The origination of many skeletal groups, including cloudinids, mollusks and trilobites, as well as the Ediacaran-Cambrian boundary itself, all seem to coincide with the succession of marked positive $\delta^{13}C_{carb}$ excursions (Figs. 9 and 10). Peak $\delta^{13}C_{carb}$ values during positive excursions during Cambrian stages 2–4 on the Siberian Platform have been proposed to record pulses of nutrients and oxygen into shallow marine seas that promoted biodiversification (He et al., 2019). By contrast, global $\delta^{13}C_{carb}$ excursions of regionally variable magnitude, from the level of the BACE to 6p, may reflect a combination of changes in glacioeustatic sea level overprinted by regional palaeomarine redox and nutrient heterogeneity. The age model framework constructed herein provides a comprehensive and editable template by which the operation of these, and other driving forces, in shaping the Ediacaran-Cambrian radiation of early animals may be explored.

Acknowledgments

Funding: FB, RW, GS, SWP, YZ and MZ acknowledge funding from the joint NERC-NSFC Biosphere Evolution Transitions and Resilience (BETR) programme (NE/P013643/1, NSFC/41661134048), MZ from the Strategic Priority Research Program (B) of the Chinese Academy of Sciences (XDB18000000, XDB 26000000), FB, SWP and GS from NERC project NE/R010129/1, and RW, SWP and FB from NERC Project NE/T008458/1. SWP acknowledges support from a Royal Society Wolfson Research Merit Award. AZ from Scientific Project 04-1-21 of the State Order of the Government of the Russian Federation to the Lomonosov Moscow State University (No. 121031600198-2). We thank C. Chilcott for technical support. We are grateful to H. Mocke and C. Hoffmann of the Geological Survey of Namibia and the Ministry of Mines and Energy, Namibia. We thank B. Romer and L. Gessert for access to Farm Swartpunt. We thank Irene Gomez Perez for enlightening discussion regarding Ara Group stratigraphy. We thank Lucas Warren and one anonymous reviewer for constructive comments and suggestions that improved the paper. **Author contributions:** FB conceived the project, FB compiled all data with the help of AZ, GS, RW, CY and MZ. FB constructed the age model with insight from all authors. FB, AC, and RW collected and analyzed Namibian samples. All authors contributed to writing the paper. **Competing interests:** Authors declare no competing interests; **Data and materials availability:** All data, including expanded geological information and full age models are available in the Supplementary Information.

Supplementary Materials for

Calibrating the temporal and spatial dynamics of the Ediacaran - Cambrian radiation of animals

Fred T. Bowyer, Andrey Yu. Zhuravlev, Rachel A. Wood, Graham A. Shields, Ying Zhou,
Andrew Curtis, Simon W. Poulton, Daniel J. Condon, Chuan Yang, and Maoyan Zhu

Correspondence to: fred.bowyer@ed.ac.uk

This file includes:

Supplementary Text

Tables S1, S3

Other Supplementary Materials for this manuscript include the following:

Supplementary Figures S1 to S4 [separate pdf document: FigsS1-S4_high_resolution_section_correlation]

Data S2 [TableS2_AgeModels.xlsx]

Supplementary Text

Geological setting and sampling strategy of upper Nama Group sections, southern Namibia

Sampling was undertaken at two stratigraphic sections in southern Namibia in July 2018 by FB, AC and RW. Sampled sections are located on Farms Nord Witputz (base of section 27°34'3.66"S, 16°42'12.60"E, section measured due north) and Swartpunt (base of section 27°28'21.88"S, 16°41'46.37"E) (Fig. 2). These two sections constitute carbonate-dominated members of the Urusis Formation (Schwarzrand Subgroup) that are separated by approximately 50-60 m of transgressive outer ramp to slope, green and purple shale of the Feldschuhhorn Member, and interbedded carbonate-siliciclastic units of the lower and middle Spitskop Member (e.g. Saylor, 2003; Saylor and Grotzinger, 1996; Wood et al., 2015).

The Huns Member on Farm Nord Witputz overlies fossiliferous sandstone and siltstone of the Nasep Member and is composed of shallow marine limestone and subordinate dolostone. Here, strata of the Huns Member have an average dip of 20° to northwest, exposing a continuous section bounded by the conformably underlying Nasep Member to the southeast, and the conformably overlying Feldschuhhorn Member to the northwest. Packstones and ooid grainstones of the Huns Member at this locality contain occasional well-developed cross-bedding accentuated by floating grains of quartz sand indicating deposition in a high energy, shallow marine, inner to mid-ramp environment above fair weather wave base. Intervals of thinly-bedded limestone with little evidence for wave activity are interpreted as reflecting deposition in a mid-shelf environment and correspond to minor transgressive parasequences, consistent with the sequence stratigraphic model of Saylor (2003).

We also compile data from a composite section noted as ‘near Swartkloofberg’(Saylor et al., 1998) (Fig. 2). The ‘near Swartkloofberg’ section corresponds to a section incorporating the Feldschuhhorn and lower Spitskop members (medium scale sequences D11- E16 of Saylor, 2003) to the southeast of Swartpunt and the upper Spitskop Member at Swartpunt (section 14 of Saylor, 1996, position of section noted in Fig. 1 of Saylor and Grotzinger, 1996). An alternative stratigraphic correlation of the section incorporating the lower Spitskop Member would reject the lower Spitskop radiometric constraint of 542.68 ± 1.25 Ma (Grotzinger et al., 1995, recalculated in Schmitz, 2012), and directly correlate the lower Spitskop succession as an expanded shallow shelf equivalent to the Swartpunt section. This stratigraphic reassessment would significantly reduce the thickness of the Spitskop Member, constraining a maximum age for the Spitskop Member of ca. 540 Ma and repositioning the BACE/A4 to the siliciclastic Feldschuhhorn Member. It would also permit a longer duration for deposition of the underlying shale-dominated Nudaus Formation in the Witputs Sub-basin. In this alternative correlation, the downturn from positive values recorded in the Huns Member at Nord Witputz (this study) would correlate with the downturn from the A3 excursion. This alternative correlation is incorporated into Model D (Table S2).

The stratigraphy, sedimentology and palaeontology of the Swartpunt section have been described in detail in previous publications (e.g. Darroch et al., 2015; Linnemann et al., 2019; Narbonne et al., 1997; Saylor, 2003; Wood et al., 2015). Sampling began 1 m above the lowermost ash layer dated at 540.095 ± 0.099 Ma (Table S1) (Linnemann et al., 2019), and continued to the summit of the koppe.

Reviewing the co-occurrence of Cloudina, Namacalathus *and* T. pedum

According to published information, *T. pedum* and *Cloudina* sensu stricto do not occur at the same level, and the *T. pedum* FAD occurs after the BACE nadir. We review these occurrences briefly below:

Nama Group, southern Namibia: The published LAD of cloudinids and *Namacalathus* occurs in the uppermost beds of the Swartpunt section, dated by CA-ID-TIMS to between ~539.6 Ma and ~538.6 Ma. There is no evidence from $\delta^{13}C_{carb}$ for the BACE at Swartpunt, and this interval is therefore most parsimoniously interpreted to be immediately pre-BACE (Model C). Though simple ichnofossils, including treptichnids, appear lower in the Nama succession, the FAD of *T. pedum* occurs in siliciclastic valley fill deposits on farms Vergelee and Sonntagsbrunn, >100km to the east of farms Swartpunt and Swartkloofberg (Wilson et al., 2012; Darroch et al., 2021). The maximum age for the *T. pedum* FAD is currently very loosely constrained by inferred lateral equivalence between the Swartkloofberg section (basal Nomtsas maximum age of ~538.6 Ma, Linnemann et al., 2019) and the valley fill deposits on farms Vergelee and Sonntagsbrunn. However, it has been noted that the tuff bed from the Nomtsas Fm at Swartkloofberg may be reworked (Linnemann et al., 2019).

South China (please see Figs. S3 and S4): Both *Cloudina* and tubicolous calcifiers of 'Cambrian'-type are at inferred-pre-BACE levels in the Lijiagou section of the shallow Yangtze Platform (see Figs. S2 and S3, Cai et al., 2019). This is the lowest published occurrence of Cambrian-type small skeletal fossils (SSFs) in South China, however accurate correlation of the $\delta^{13}C_{carb}$ profile in this section remains problematic. In South China, the FAD of *T. pedum* occurs in the phosphatic Zhongyicun Mb of the Zhujiqing Fm in multiple sections of the shallow platform. The underlying (Daibu) Member and correlative units across the Yangtze Platform host the BACE nadir.

Kazakhstan: The FAD of protoconodonts occurs in the lower Aksai Mb of the Chulaktau Fm (Yang et al., 2016). The Aksai Mb is an extremely condensed phosphatic unit (~5m thick). The cloudinid *Rajatubulus* occurs in the overlying Karatau Mb (5-10m thick unit) (Yang et al., 2016), which is entirely phosphatic. It remains possible that these phosphatic units correspond to the Zhongyicun Mb, thereby implying a post-BACE LAD of cloudinids in the Maly Karatau of Kazakhstan. Given the uncertainty in accurate age determination of these members brought on by the unsuitable (phosphatic) lithology for robust $\delta^{13}C_{carb}$ chemostratigraphy, we do not place undue weight on these occurrences. However, we do note in Table S3 that the Chulaktau Fm may host the global LAD of cloudinids in the lowermost Fortunian (citing Yang et al., 2016). *T. pedum* has not been recovered from the Chulaktau Fm of underlying units, implying that the regional FAD of this ichnospecies is most likely post-BACE in age.

Siberia: The FAD of anabaritids occurs in the upper Ust'-Yudoma Fm at the Kyra-Ytyga section on the Yudoma River of SE Siberia (Zhu et al., 2017). In this section, anabaritids co-occur with cloudinids during a positive $\delta^{13}C_{carb}$ plateau and below a downturn that is inferred to be the BACE onset. Anabaritids also occur in a pre-BACE position in the lower Turkut Fm of the Khorbusuonka River of NE Siberia (Rogov et al., 2015; Knoll et al., 1995; Pelechaty et al., 1996). The LAD of cloudinids is also within this pre-BACE interval throughout sections of the Siberian Platform. The FAD of *T. pedum* occurs in the upper Syhargalakh Fm along the Khorbusuonka River of the Olenek Uplift. The Syhargalakh Fm is a condensed siliciclastic unit, and the *T. pedum* FAD occurs above a poorly calibrated maximum age derived from air-abrasion ID-TIMS U-Pb dating of the Tas-Yuryakh volcanic breccia (Bowring et al., 1993) (Table S1). The *T. pedum* FAD in this section occurs beneath carbonates of the Mattaia Fm that host *Aldanella* and a CA-ID-TIMS U-Pb age of ~529.70 Ma (Kaufman et al., 2012; Grazhdankin et al., 2019). In sections of the SW Siberian

Platform, *T. pedum* occurs within a bed with a maximum detrital zircon age of 531.1 ± 5.20 Ma (weighted mean 530.6 ± 5.30 Ma) in the Irkut Formation (Marusin et al., 2020, their Fig. 4e). However, this trace fossil does not display a clear regular probing pattern typical of *T. pedum* and can be rather interpreted as a treptichnid s.l. The FAD of *T. pedum* across the Siberian Platform therefore remains poorly constrained but most likely above the nadir of the BACE.

Spain: According to Álvaro et al. (2019), the lowest occurrence of *T. pedum* is within the lower Arrocampo Fm of the Ibor and Navalpino anticlines, below a regional unconformity. The LAD of in situ *Cloudina* is noted from the underlying Villarta Fm in the same succession. Allochthonous broken fragments of reworked *Cloudina* are noted from megabreccia blocks in the neighbouring Valdelacasa anticline. Given the absence of a robust $\delta^{13}C_{carb}$ framework and the complexity of the fragmentary record, it is not possible to assign the Valdelacasa cloudinids to the lower Cambrian.

Brazil: The Tamengo Fm hosts cloudinids from an interval with positive $\delta^{13}C_{carb}$ (Boggiani et al., 2010). High precision radiometric dating constrains this interval as Ediacaran (>541 Ma) (Parry et al., 2017). Unfortunately, the succession transitions to siliciclastics of the Guaicurus Fm, and the age of this transition is poorly constrained in time pre-BACE.

Paraguay: Cloudinids and other Ediacaran skeletal fossils in Paraguay occur in a positive $\delta^{13}C_{carb}$ plateau as demonstrated in numerous publications (e.g. Warren et al., 2019, 2017, 2011). These $\delta^{13}C_{carb}$ records, and an associated U-Pb SHRIMP age of 545 ± 4.5 Ma (Warren et al., 2019), correlate most readily with the late Ediacaran $\delta^{13}C_{carb}$ record. We are not familiar with any published reports that show *T. pedum* co-occurring with *Cloudina* in sections of the Itapucumi Group, and to our knowledge, the FAD of *T. pedum* is therefore most likely higher in the succession, in accordance with the global record.

Carbon isotope analyses

Carefully selected micritic carbonate was microdrilled from hand samples and simultaneously analysed for $\delta^{13}C_{carb}$ and $\delta^{18}O_{carb}$ on an Elementar PRECISION stable isotope ratio mass spectrometer following reaction with 100% orthophosphoric acid at 75°C, using an Elementar iso FLOW system at the Wolfson Laboratory, School of Geosciences, Grant Institute, University of Edinburgh. New $\delta^{13}C_{carb}$ data from the upper Nama Group are reported in per mil (‰) notation relative to the Vienna Pee Dee Belemnite standard (VPDB) alongside compiled global $\delta^{13}C_{carb}$ data for the interval ca. 551-517 Ma in Table S2 (Supplementary xlsx file). The standard deviation for replicate analyses (n=7) of an in-house coral standard (Reference COR1D) measured alongside samples (standard-sample bracketing) was better than ±0.02‰ for $\delta^{13}C_{carb}$ and ±0.08‰ for $\delta^{18}O_{carb}$.

Sr isotope screening criteria

The long mean residence time of Sr (3–5 Myrs) relative to the mixing time of the global ocean (~1500 yrs) results in a globally homogeneous seawater Sr isotopic composition (Elderfield, 1986). Long term changes in oceanic $^{87}Sr/^{86}Sr$ reflect the balance between radiogenic (high $^{87}Sr/^{86}Sr$) input derived from continental weathering versus non-radiogenic (low $^{87}Sr/^{86}Sr$) input from hydrothermal alteration of oceanic crust (Brass, 1976). Unlike the majority of Phanerozoic studies that benefit from targeted analyses of Sr retained with high fidelity in carbonate biominerals, strontium isotope stratigraphy in pre-Cambrian and lower Cambrian sections relies upon identifying primary marine Sr isotopic compositions from bulk (often micritic) carbonate (e.g. Halverson et al., 2007). Post-depositional diagenetic exchange and contamination of bulk carbonate by silicate-bound phases commonly result in deviation towards more radiogenic values (Veizer and Compston, 1976), however late diagenesis may also skew $^{87}Sr/^{86}Sr$ to lower values

(Brand et al., 2010). Furthermore, identifying the most robust estimates of seawater $^{87}Sr/^{86}Sr$ from legacy datasets is often hampered by the limited geochemical information necessary for adequate screening, and the lack of a standardized methodology for chemical pre-treatment and dissolution over the past 30 years of Sr isotope research.

Due to the specific complications noted above, in addition to sample-specific carbonate mineralogy and differential diagenesis, a universal screening procedure to determine primary seawater $^{87}Sr/^{86}Sr$ from bulk carbonate data has proven elusive. A number of criteria are classically used to identify the most isotopically altered samples, including Mn/Sr, Mg/Ca, $\delta^{18}O$ and $^{87}Rb/^{86}Sr$. However, applying cut-off values for these parameters to determine degrees of diagenetic alteration is often an unsuitable oversimplification, especially in the case of Mn/Sr, where some primary marine carbonates may have precipitated from manganous seawater (e.g. Halverson et al., 2007).

We compiled an updated dataset of published $^{87}Sr/^{86}Sr$ from stratigraphic sections covering the Ediacaran-Cambrian transition interval (Table S2), and employed a liberal screening procedure using available geochemical data in an attempt to filter out values considered least likely to represent seawater composition. Samples with $^{87}Sr/^{86}Sr > 0.7095$ and >20% insoluble residue (where this information is available) were automatically discounted, and the remaining data were screened on a section by section basis in order to identify trends suggestive of diagenetic alteration, including cross-plotting $^{87}Sr/^{86}Sr$ against Mn/Sr, [Sr], [Rb], and $\delta^{18}O$. In most cases, clear covariations between these parameters was not observed, with the exception of [Sr] (see Supplementary Information for details). We then discounted all data with Mn/Sr > 1 and [Rb] > 1ppm, as a final test. A critical evaluation of the screening criteria used, and implications for the resulting $^{87}Sr/^{86}Sr$ correlation, are provided in the supplementary information. All data were normalized to NIST SRM987 = 0.710250. The resulting compilation, including data that did not pass our screening procedure, is provided in Table S2, and shown graphically by lithology and [Sr] in Figure 4. We consider the lowest values throughout the studied interval to best represent seawater $^{87}Sr/^{86}Sr$, with the exception of the values reported from the Mastakh and Khatyspyt formations (red boxes in Fig 4c,g, see Supplementary Information).

Our screening procedure removed ~50% of the data compiled from the published literature, most of which tended towards radiogenic values. The remaining $^{87}Sr/^{86}Sr$ dataset (Fig 4) shows significant variability, likely due to the effects of diagenesis or contamination that are indecipherable using only the published geochemical information. We consider the lowest values throughout the studied interval to best represent seawater $^{87}Sr/^{86}Sr$, with the exception of the values reported from the Mastakh and Khatyspyt formations (red boxes in Fig. 4c and 4g, see below). Low $^{87}Sr/^{86}Sr$ values are commonly retained in high [Sr] (>500ppm) limestone and dolomite samples, whereas samples with low [Sr] tend to deviate towards more radiogenic values, consistent with the findings of Halverson et al. (2007). However, of the 208 samples that were removed by the final screening criteria (Mn/Sr > 1, [Rb] > 1ppm), 25 closely follow the trend captured by the 'most reliable' data, which attests to the complications inherent in assigning cut-off thresholds for sample screening of legacy datasets. The resulting seawater $^{87}Sr/^{86}Sr$ curves (grey lines in Fig. 4) show trends consistent with previous correlations (e.g. Halverson et al., 2007; Maloof et al., 2010), whereby latest Ediacaran to Fortunian values remain relatively constant in the range 0.70840 – 0.70850 before beginning to decrease in lower Cambrian Stage 2 and reaching a nadir of ~0.70806 at the boundary between stages 2 and 3, followed by increasing values during Stage 3.

Table S1.

Radiometric ages

Ages in red are not included in the compilation for the reasons provided.		
Age (Ma)	**Details**	**Reference**
515.56 ± 1.03 (1.16)	Zircon U-Pb age from the upper Lemdad Fm (equivalent to Lower Issafen Fm) of the Lemdad syncline, Morocco (section Le-XI). Five single grain analyses, originally processed via air abrasion in Landing et al. (1998), and recalculated by Maloof et al. (2010) using updated U decay constant (see Maloof et al. (2010) for details). Lower Botoman based on trilobite biostratigraphy. Marks onset of peak V? in Morocco.	(Landing et al., 1998; Maloof et al., 2010)
517.22 ± 0.31 (0.40) [0.66]	Zircon U-Pb CA-ID-TIMS age of bentonite 7m above the base of the Purley Shale Fm, Woodlands Quarry, Warwickshire, England (Avalon terrane). Five of nine single grain analyses (samples z1-4, z12), MSWD = 0.67.	(Williams et al., 2013)
518.03 ± 0.69 (0.71)	Youngest zircon U-Pb CA-ID-TIMS age (incorporating U-Pb tracer calibration uncertainty) of five single grain analyses of detrital zircons from the Maotianshan shale immediately underlying Chengjiang biota. Taken as maximum depositional age for the Chengjiang biota.	(Yang et al., 2018)
518.59 ± 0.20 (0.32) [0.63]	Zircon U-Pb CA-ID-TIMS age of tuff bed in the upper Amouslek Formation, Timoulaye Izder section, Morocco (sample Tim-269.5). (MSWD = 0.22, n = 3). Within the upper *Choubertella* or possibly lower *Daguinaspis* Zone.	(Landing et al., 2020)

518.99 ± 0.14 (0.20) [0.58]	Zircon U-Pb CA-ID-TIMS age of tuff bed in lower Amouslek Formation correlated to neighbouring section at Tazemmourt to upper *Choubertella* Zone. Sample Ti-Am-34.0 (MSWD = 0.38, n = 6).	(Landing et al., 2020)
519.30 ± 0.23 (0.57) [0.77]	Zircon U-Pb CA-ID-TIMS age of the Caerfai Bay Shales Fm at Cwm Bach, Pembrokeshire, South Wales (Avalon terrane). Six of seven fractions (single grains or fragments) from sample Cwm Bach 1 (MSWD = 1.1, n = 6).	(Harvey et al., 2011)
519.23 ± 0.14 (0.21) [0.58]	Zircon U-Pb CA-ID-TIMS age of tuff bed that rests unconformably atop the Tiout Member, in the basal Amouslek Formation (sample Ti-Am-0.0). Transition between upper *Fallotaspis plana* and lower *Choubertella* zones. Approximate zero-crossing point of recovery from peak IV.	(Landing et al., 2020)
519.87 ± 0.24 (0.35) [0.64]	Zircon U-Pb CA-ID-TIMS age of brown-weathering dolomitic feldspathic sandstone 8.5m below trilobite horizon T1 (sample Ti-I-neg8.5). Within lower member of the Igoudine Formation. Interpreted as a maximum depositional age. Large relative uncertainty (MSWD = 2.60, n = 2).	(Landing et al., 2020)
520.93 ± 0.14 (0.28) [0.61]	Zircon U-Pb CA-ID-TIMS age of tuff bed in the upper Lie de vin Formation, Tiout section, Anti Atlas Mountains, Morocco (sample M236). Six single grain analyses (MSWD = 0.42, n = 6). Ash bed at base of rising limb of peak IV.	(Maloof et al., 2010)
521.06 ± 0.12 (0.28) [0.61]	Zircon U-Pb CA-ID-TIMS age of tuff deposit 210m below top of Lie de vin Formation in the Tiout section, 500m below base of the Tiout Member, 310m below peak IV (sample	(Landing et al., 2020)

	Tiout-566). (MSWD = 0.61, n = 7)	
523.17 ± 0.16 (0.42) [1.0]	Zircon U-Pb CA-ID-TIMS age of tuff bed in the lower Lie de vin Formation at Oued Sdas section, Anti Atlas Mountains, Morocco (sample M234). Ten single grain analyses (MSWD = 1.2, n = 10) Ash bed at level immediately prior to peak II.	(Maloof et al., 2010)
524.837 ± 0.092 (0.35) [0.93]	Zircon U-Pb ID-TIMS age from tuff bed in the upper Tifnout Member (Adoudou Formation) at Oued Sdas section, Anti Atlas Mountains, Morocco (sample M231). Mixture of 5 air abraded and 3 chemically abraded single grain analyses (MSWD = 0.72, n = 8) Ash bed within falling limb of peak 6p.	(Maloof et al., 2010)
525.343 ± 0.088 (0.35) [0.93]	Zircon U-Pb ID-TIMS age from a tuff bed in the middle Tifnout Member (Adoudou Formation) at Oued Sdas section, Anti Atlas Mountains, Morocco (sample M223). Mixture of 6 air abraded and 6 chemically abraded single grain analyses (MSWD = 0.33, n = 11). Ash bed at/immediately after max values of peak 6p.	(Maloof et al., 2005), updated in (Maloof et al., 2010)
526.5 ± 1.1	SHRIMP U-Pb age of the base of the Badaowan (Shiyantou-equivalent) Formation, bed 9 at Meishucun section, Yunnan Province, South China. Note that the ZHUCE excursion in models B and C is curtailed early at Meishucun, consistent with this age. However, the ZHUCE excursion at Xiaotan section is considered to correlate with the entirety of 6p in these models.	(Compston et al., 2008)
530.02 ± 1.2	Zircon ID-TIMS (air abrasion) age for tuff bed 24.32 – 24.58m above the base of the Chapel Island Formation, Ratcliffe Brook Group, Somerset Street, Saint	(Isachsen et al., 1994), recalculated in (Schmitz, 2012)

	John, southern New Brunswick (sample SoS-24.4). Three multigrain fractions. Approximate age of the Chapel Island Formation lithofacies association (Member) 5 (Mystery Lake Member) after regional litho- and biostratigraphic correlation with sections in Saint John, New Brunswick(Landing, 1994, 1991). Middle part of trace fossil zone *Rusophycus avalonensis*, Placentian Series.	
529.7 ± 0.3	Zircon U-Pb CA-ID-TIMS age for tuff deposit in upper Mattaia Formation, Mattaia Creek mouth (above FAD *Aldanella attleborensis*). No detailed information available on the number of single grain analyses, concordance or MSWD for this age, as it was published in abstract form only. However, if correct, this places a minimum age constraint on the FAD of *A. attleborensis* which is consistent with a first appearance approximately contemporaneous with peak 5p in Siberia, as previously suggested.	(Grazhdankin et al., 2019; Kaufman et al., 2012)
533 Ma	Zircon U-Pb ID-TIMS age from bed 5 of Meishucun section (Zhongyicun Member). Age in abstract form only and no information pertaining to uncertainty or procedural laboratory techniques (including number of single grain analyses, air vs chemical abrasion, tracer etc.) exist in published form to our knowledge. Likely CA-ID-TIMS. Whilst we do not include this age in our model, we note that the age model remains entirely consistent with this age. Unfortunately, the phosphorite interval of the Zhongyicun Member at	Age provided in (Maloof et al., 2010) citing (Brooks et al., 2006)

	Meishucun does not afford any useful, detailed chemostratigraphic correlation potential at present.	
534.6 ± 0.5	Zircon air-abrasion ID-TIMS age for ultra-potassic trachyrhyolite porphyry cobbles in a fluvial conglomerate of the lower Tyuser Formation in the Kharaulakh ranges, lower Lena River. Age not adjusted for updated U decay constant.	(Bowring et al., 1993)
538.58 ± 0.19 (0.24) [0.62]	Zircon U-Pb CA-ID-TIMS age of a tuff bed in the lower Nomtsas Formation exposed on Farm Swartkloofberg, west of Swartpunt (sample 17SWART7, ash 6, equivalent to 92-N-1 of Grotzinger et al. (1995). Three single grain analyses (MSWD = 0.10, n = 3)	(Grotzinger et al., 1995; Linnemann et al., 2019)
538.99 ± 0.21 (0.25) [0.63]	Zircon U-Pb CA-ID-TIMS age of the highest ash bed exposed in the upper Spitskop Member of the section on Farm Swartpunt (sample 15UNA20, ash 5). Three single grain analyses (MSWD = 2.2, n = 3). This age appears too young when considering the lack of observed hiatus (or facies change) above the preceding 3 dated tuff deposits (15UNA17-19, see below) in this section, all of which give ages of ca. 539.6 Ma. The ages of 15UNA22 and 15UNA19 yield a depositional rate of 94.41m/Myrs, whereas the ages of 15UNA19 and 15UNA20 yield a depositional rate for identical lithofacies of 11.86m/Myrs. MSWD for 15UNA20 is also high. For these reasons, this age is not included in our correlation.	(Linnemann et al., 2019)
539.40 ± 0.23 (0.35) [0.66]	Zircon U-Pb CA-ID-TIMS age of a 10cm-thick bed of sandy, hematite-rich	(Hodgin et al., 2020)

	dolostone interpreted as a diagenetically altered tuffaceous horizon in the upper La Ciénega Formation (top of Unit 3 at Cerro Clemente), above a laterally reproducible negative excursion correlated with the global BACE (sample CC1801-138). Interpreted conservatively as a maximum depositional age. Six single grain zircon fragments (of 10) (MSWD = 1.05, n = 6). We consider this level to be slightly younger than the age itself, to maintain consistency with ages and carbon isotope profile of the Swartpunt section.	
539.4 ± 2.9	SHRIMP U-Pb age of bentonites, Zhongyicun Member of the Zhujiaqing Formation, bed 5 at Meishucun section, Yunnan Province, South China. Note, age updated by ID-TIMS (Brooks et al., 2006, see above), but data in abstract form only. We prefer the younger age provided by Brooks et al. (2006) for this age model in agreement with Maloof et al. (2010), however uncertainty in this age (noted above) precludes inclusion in age model figures.	(Compston et al., 2008)
539.64 ± 0.19 (0.23) [0.62]	Zircon U-Pb CA-ID-TIMS age of tuff bed in upper Spitskop Member in middle of section on Farm Swartpunt (sample 15UNA19, ash 4). Four single grain analyses (MSWD = 0.46, n = 4).	(Linnemann et al., 2019)
539.52 ± 0.14 (0.20) [0.61]	Zircon U-Pb CA-ID-TIMS age of tuff bed in upper Spitskop Member in middle of section on Farm Swartpunt (sample 15UNA18, ash 3). Five single grain analyses (MSWD = 1.4, n = 5).	(Linnemann et al., 2019)
539.58 ± 0.34 (0.37) [0.68]	Zircon U-Pb CA-ID-TIMS age of tuff bed in upper Spitskop Member in middle of section on Farm Swartpunt	(Linnemann et al., 2019)

	(sample 15UNA17, ash 2). Six single grain analyses (MSWD = 0.44, n = 6)	
540.095 ± 0.099 (0.17) [0.60]	Zircon U-Pb CA-ID-TIMS age of an ash bed in the upper Spitskop Member at the base of the section on Farm Swartpunt (sample 15UNA22, ash 1, equivalent to 94-N-11 of (Grotzinger et al., 1995)). Five single grain analyses (MSWD = 1.7, n = 5).	(Grotzinger et al., 1995; Linnemann et al., 2019)
541.00 ± 0.13 (0.21) [0.81]	Zircon U-Pb CA-ID-TIMS age from Ara Group (A4 Member, 3045m depth in Birba-5 well, SOSB), Oman (sample BB-5). 8 concordant single grain analyses of 18 total (MSWD = 1.0, n = 8)	(Bowring et al., 2007)
541.85 ± 0.75 (0.77) [0.97]	Zircon U-Pb age for ash bed at top of Tamengo Formation, Brazil. Dated via U-Pb CA-ID-TIMS using the ET535 tracer. Cluster of the five youngest concordant analyses (MSWD = 3.3, n = 5 out of 11)	(Parry et al., 2017)
542.33 ± 0.11 (0.19) [0.79]	Zircon U-Pb CA-ID-TIMS age from Ara Group (A3 Member, 9m below top of A3 carbonate unit, 2194.4m depth in Mukhaizna-11 well), Oman (sample MKZ-11B). 8 concordant single grain analyses of 16 total (MSWD = 0.50, n = 8)	(Bowring et al., 2007)
542.37 ± 0.28 (0.32) [0.68]	Zircon U-Pb age for ash bed at top of Tamengo Formation, Brazil. Dated via U-Pb CA-ID-TIMS using the ET535 tracer. Cluster of four concordant analyses (MSWD = 0.68, n = 4 out of 8)	(Parry et al., 2017)
542.54 ± 0.45 (0.53) [1.13]	Zircon U-Pb CA-ID-TIMS age from top of Fara Formation (Ara A2-A3 equivalent), Oman (sample WB.01.1). 4 concordant single grain analyses of 10 total (MSWD = 2.6, n = 4)	(Bowring et al., 2007)
542.68 ± 1.25 (2.80)	Zircon Pb-Pb ID-TIMS age of an ash bed in the lower Spitskop Member on Farm Witputs (sample 91-N-1 or,	(Grotzinger et al., 1995), recalculated in (Schmitz, 2012)

	alternatively, BZS-7). Air abrasion age of eight single grain and small multigrain fractions. Grotzinger et al. (1995) originally reported a weighted mean ^{207}Pb/^{206}Pb crystallization age of 545.1 ± 0.70 Ma (MSWD = 0.22, n = 8).	
542.90 ± 0.12 (0.20) [0.80]	Zircon U-Pb CA-ID-TIMS age from Ara Group (A3 Member, 3m above base of A3 carbonate unit, 3988.3m depth in Minha-1 well), Oman (sample Minha-1A). 8 concordant single grain analyses of 17 total (MSWD = 0.62, n = 8)	(Bowring et al., 2007)
543.40 ± 3.5	SIMS zircon U-Pb age from an ash bed 45m above the base of the Baimatuo Member, Zhoujiaao section, southern margin of the Huangling anticline, 3 Gorges Area. Age constrains plateau in $\delta^{13}C_{carb}$ at ~3‰.	(Huang et al., 2020)
543.9 ± 0.24 Recalculated to 542.8 ± 1.30 Ma by Maloof et al. (2010) and interpreted as the maximum age of the unit by Maloof et al. (2010)	Zircon U-Pb ID-TIMS (air abrasion), Kessyusa Group (Syhargalakh Formation) volcanic breccia of the Tas-Yuryakh volcanic complex (Khorbusuonka River). We stress that these zircons have not been re-analysed using the updated chemical abrasion methodology and, as stated in Maloof et al. (2010), have lost Pb. We anticipate substantial modification to this age after future re-analysis. If taken as a minimum age for the top of the Turkut Formation, this may imply correlation of the negative excursion at the top of the Turkut Formation (e.g. at the Olenek River section) with the either the A0 excursion, or the more minor negative excursion in the lowermost part of the upper Dengying Fm (Beiwan and equivalent members). We prefer to correlate the Turkut negative excursion with the A4 onset, which is also	(Bowring et al., 1993)

	consistent with the interpretation of Maloof et al. (2010) for a maximum age of 542.8 ± 1.30 Ma for the Tas-Yuryakh volcanic complex, and a minimal hiatus separating the Syhargalakh Fm from the underlying Turkut Formation.	
546.25 ± 0.19 (0.27) [0.64]	Ash bed in the Jiucheng Member, 471m above the base of the Dengying Formation at Yinchangpo section (sample 14YCP02). Zircon U-Pb CA-ID-TIMS age (n = 5 of 12). Originally dated via SIMS with weighted mean ^{207}Pb/^{206}Pb age of 546.3 ± 2.70 (3.80) (MSWD = 0.58, n = 44 of 50). Constrains a maximum depositional age for the base of the overlying Baiyanshao Member at Yinchangpo section.	CA-ID-TIMS age (Yang et al., 2021) updated from (Yang et al., 2017)
546.72 ± 0.21 (0.29) [0.89]	Zircon U-Pb CA-ID-TIMS age of tuff bed from Ara Group (middle of A0 Member, 3847m depth in Asala-1 well), Oman (sample Asala-1 c21). 8 concordant single grain analyses of 12 total (MSWD = 0.92, n = 8).	(Bowring et al., 2007)
547.23 ± 0.28 (0.36) [0.96]	Zircon U-Pb CA-ID-TIMS age of tuff bed from the Fara Formation (200m above the base of the formation), Oman (sample WB.01.2). Considered to predate A0 Member. 8 concordant single grain analyses of 17 total (MSWD = 1.3, n = 8)	(Bowring et al., 2007)
547.36 ± 0.23 (0.31) [0.91]	Zircon U-Pb CA-ID-TIMS age from 8 single grain analyses (sample 94-N-10B). Lower Hoogland Member, Zaris Formation, Kuibis Subgroup, Nama Group, Namibia. 8 single grain analyses (MSWD = 1.4, n = 8).	(Bowring et al., 2007). (Schmitz, 2012) report age of 547.32 ± 0.31 (0.65) Ma.
550.14 ± 0.16 (0.24) [0.63]	Zircon U-Pb CA-ID-TIMS age of an ash in Doushantuo Member IV (Miaohe Member) at Jijiawan section, Hubei Province (Yangtze	Age updated in (Yang et al., 2021) from initial age of (Condon et al., 2005).

	Gorges area), South China (sample 16JJW-3). Ash bed is 85cm below base of Dengying Formation (Hamajing Member). Six concordant (of 14) single grain analyses (MSWD = 1.9). Original ages in (Condon et al., 2005) for same ash bed (sample JIN04-2): U-Pb concordia age of 551.07 ± 0.61 Ma (MSWD = 0.48), and weighted mean $^{207}Pb/^{206}Pb$ 550.55 ± 0.75 Ma (MSWD = 0.48). Age recalculated in (Schmitz, 2012) using two concordant (of ten total) single grain analyses. All ten zircons yield weighted mean $^{207}Pb/^{206}Pb$ age of 548.09 ± 2.61 Ma.	
552.96 ± 0.19 (0.30) [0.66]	Zircon U-Pb CA-ID-TIMS age of a tuff bed in the lower part of the Zimnegory Formation, Valdai Group, White Sea area (sample WhiteSeaAsh). Five concordant (of 11) single grain analyses. Sample previously dated at 555.3 ± 0.3 Ma (Martin et al., 2000), recalculated to 552.85 ± 0.77 (2.62) ($^{207}Pb/^{206}Pb$) by (Schmitz, 2012).	(Yang et al., 2021)
554.29 ± 0.14 (0.22) [0.63]	Zircon U-Pb CA-ID-TIMS age for an ash bed 3.8m above the phosphorite layer at the base of the Jiucheng Member at Xiaolantian section, eastern Yunnan (sample 14CJ07, MSWD = 0.8, n = 7 of 10). Age implies highly condensed sedimentation, cryptic hiatus within lower Jiucheng member, reworking during deposition, or incorporation of xenocrystic materials in the magmatic environment (see age of sample 14YCP02). See discussion in (Yang et al., 2021).	Updated from original SIMS age of (Yang et al., 2017) by (Yang et al., 2021)

555.18 ± 0.3 (0.34) [0.70]	Zircon U-Pb age for ash bed in the upper Bocaina Formation, Brazil. Dated via U-Pb CA-ID-TIMS using the ET535 tracer. (MSWD = 1.6, n = 8 out of 8)	(Parry et al., 2017)
556.26 ± 0.21 (0.25) [0.65]	Zircon U-Pb CA-ID-TIMS age of the dolostone/chert boundary of the basal Liuchapo Formation, Nangao section (samples 17WA05). Five concordant (of 9 total) single grain analyses (MSWD = 0.2, n = 9).	(Yang et al., 2021)
556.38 ± 0.14 (0.27) [0.65]	Zircon U-Pb CA-ID-TIMS age of the dolostone/chert boundary of the basal Liuchapo Formation, Wengxiu section (samples 17GZWX01). Eight concordant (of 10 total) single grain analyses (MSWD = 1.8, n = 8).	(Yang et al., 2021)
556.6 ± 6.4	Zircon U-Pb CA-ID-TIMS age from 4 single grain analyses (sample 846). Hanging Rocks Formation (Maplewell Group, Charnian Supergroup).	(Noble et al., 2015)
556.78 ± 0.10 (0.18) [0.62]	Zircon U-Pb CA-ID-TIMS age from bentonite bed in middle Mohylivska Formation, Podolia, Ukraine (sample B1b). All five zircons from bentonite B1 are concordant, yielding a statistically equivalent weighted mean age (MSWD = 2.2, n = 5)	(Soldatenko et al., 2019)
557 ± 3	SHRIMP zircon U-Pb age for ash bed in dolostone of the Liuchapo Fm at Fanglong section, Guizhou province. Immediately above recovery from a negative $\delta^{13}C_{carb}$ excursion.	(Zhou et al., 2018)
557.28 ± 0.14 (0.22) [0.63]	Zircon U-Pb CA-ID-TIMS age of tuff bed at the base of the Verkhovka Formation, Valdai Group, White Sea area (sample 9607-1601). Six concordant (of 9 total) single grain analyses (MSWD = 1.6).	(Yang et al., 2021)

561.85 ± 0.34 (0.66) [0.89]	Zircon U-Pb CA-ID-TIMS age from 7 concordant (of 12) single grain analyses (sample 912). Bradgate Formation (Maplewell Group, Charnian Supergroup). (MSWD = 1.2)	(Noble et al., 2015)
562.5 ± 1.1	Zircon U-Pb CA-ID-TIMS age from 7 concordant single grain analyses (MSWD = 0.34). 27m below the top of the Trepassey Formation, Shingle Head, Mistaken Point ecological reserve, Newfoundland (sample N10-SH6B). Detailed stratigraphic mapping and reassessment by (Matthews et al., 2020) places this ash bed in the lower Fermeuse Formation. See (Matthews et al., 2020) for discussion of additional uncertainties associated with the age of sample N10-SH6B. The maximum age of the lower Fermeuse Formation suggested by sample SH-2 of (Matthews et al., 2020) (see below) is 564.13 ± 0.20 Ma.	(Canfield et al., 2020)
562.7 ± 3.8	Re-Os age lower Buah Fm, Well M. Initial $^{187}\mathrm{Os}/^{188}\mathrm{Os}$ = 0.68 ± 0.01. (2σ age, MSWD = 1.40, n = 7)	(Rooney et al., 2020)
564.13 ± 0.20 (0.25) [0.65]	Zircon U-Pb CA-ID-TIMS age of tuff bed in the lower Fermeuse Formation (Shingle Head surface), Mistaken Point Ecological Reserve, Newfoundland (sample SH-2). Six single grain analyses (MSWD = 1.5, n = 6)	(Matthews et al., 2020)
564.71 ± 0.63 (0.65) [0.88]	Zircon U-Pb CA-ID-TIMS age of tuff bed immediately atop the ‘Pizzeria’ in the Trepassey Formation, Long Cove, Mistaken Point Ecological Reserve, Newfoundland (sample LC-1). Two single grain analyses (MSWD = 0.69, n = 2 of 11)	(Matthews et al., 2020)
565.00 ± 0.16 (0.22) [0.64]	Zircon U-Pb CA-ID-TIMS age of tuff deposit immediately above ‘E’ surface of upper Mistaken Point Formation (~60m	(Matthews et al., 2020)

	below top of Formation), Mistaken Point Ecological Reserve, Newfoundland (sample MP-14). Four concordant single grain analyses (MSWD = 1.2, n = 4)	
565.22 ± 0.33 (0.65) [0.89]	Zircon U-Pb CA-ID-TIMS age from 2 concordant (of 5) single grain analyses (sample 907). Beacon Hill Formation (Maplewell Group, Charnian Supergroup). (MSWD = 0.42, n = 2)	(Noble et al., 2015)
566.25 ± 0.35 (0.48) [0.77]	Zircon U-Pb CA-ID-TIMS age of Mistaken Point Formation, Newfoundland (sample MPMP33.56). Five single grain analyses (MSWD = 1.3, n = 5). Analyses show degree of discordance, and the age of the same ash horizon has been updated in (Matthews et al., 2020) (their sample MP-14, see above). We favour the concordant age of (Matthews et al., 2020) sample MP-14.	(Pu et al., 2016)
567 ± 3.9	Zircon U-Pb age of volcanic tuff from Sylvitsa Group (Perevalok Formation), Krutaya Gora section, Us'va River, central Urals (sample 09-03-15). (MSWD = 1.14, n = 16). Age shown in figures but lack of detailed analytical methods provided in original publication.	(Grazhdankin et al., 2011)
567.3 ± 3.0	Re-Os age upper Unit PH4, inferred equivalent to Blueflower Fm (sample A1707). 16m above contact with Gametrail Fm, Coal Creek Section, Ogilvie Mountains. Initial ^{187}Os/^{188}Os = 0.61 ± 0.04. (2σ age, MSWD = 0.81, n = 6)	(Rooney et al., 2020)
567.63 ± 0.21 (0.26) [0.66]	Zircon U-Pb CA-ID-TIMS age of tuff bed in the middle Briscal Formation (~110m above the base of the Formation) overlying the 'Brasier Surface', Mistaken Point Ecological Reserve, Newfoundland (sample BRS-	(Matthews et al., 2020)

	1). Five single grain analyses (MSWD = 2.1, n = 5)	
569.08 ± 0.45 (0.73) [0.94]	Zircon U-Pb CA-ID-TIMS age from 2 concordant (of 12) single grain analyses (sample 918). Bennscliffe Breccia between Blackbrook Reservoir Formation and Beacon Hill Formation (Charnian Supergroup). (MSWD = 0.8, n = 2).	(Noble et al., 2015)
570.94 ± 0.38 (0.46) [0.77]	Zircon U-Pb CA-ID-TIMS age of tuff bed in upper Drook Formation, Newfoundland (sample Drook-2). Five single grain analyses (MSWD = 0.33, n = 5). Despite ongoing uncertainty in the age of this ash layer, we favour the model of (Matthews et al., 2020) based on maintenance of stratigraphic superposition using new ages from the upper Drook Formation (their sample DRK-10) and overlying lower Briscal Formation (their sample DRK-1). Accordingly, the age of sample Drook-2 is not included in our age model despite concordant single grain analyses and low uncertainty.	(Pu et al., 2016)
571.38 ± 0.16 (0.25) [0.66]	Zircon U-Pb CA-ID-TIMS age of tuff bed in the basal Briscal Formation (~20m above top of Drook Formation), Daley’s Cove, Mistaken Point Ecological Reserve, Newfoundland (sample DRK-1). Eight single grain analyses (MSWD = 2.0, n = 8)	(Matthews et al., 2020)
574.0 ± 4.7	Re-Os age upper Nadaleen Fm, J1719. Initial ^{187}Os/^{188}Os = 0.60 ± 0.01. (2σ age, MSWD = 0.75, n = 8)	(Rooney et al., 2020)
574.17 ± 0.19 (0.24) [0.66]	Zircon U-Pb CA-ID-TIMS age of Drook Formation (~25m below top of Formation), ‘Pizza Disc Bed’, Pigeon Cove, Mistaken Point Ecological Reserve, Newfoundland (sample DRK-10). Nine single grain	(Matthews et al., 2020)

	analyses (MSWD = 2.8, n = 9)	
575.0 ± 5.1	Re-Os age Nadaleen Fm, J1443. Initial ^{187}Os/^{188}Os = 0.60 ± 0.01. (2σ age, MSWD = 1.20, n = 5)	(Rooney et al., 2020)
578.2 ± 5.9	Re-Os age middle Khufai Fm, Well L. Initial ^{187}Os/^{188}Os = 1.15 ± 0.05. (2σ age, MSWD = 0.97, n = 7)	(Rooney et al., 2020)
579.88 ± 0.44 Ma (0.52) [0.81]	Zircon U-Pb CA-ID-TIMS age of lower Drook Formation (sample NoP-0.9). Five single grain analyses (MSWD = 0.82, n = 5)	(Pu et al., 2016)
580.90 ± 0.40 (0.53) [0.82]	Zircon U-Pb CA-ID-TIMS age of Upper Mall Bay Formation (sample GCI-neg6.55). Nine single grain analyses (MSWD = 1.1, n = 9)	(Pu et al., 2016)
585.7 ± 2.6 [2.8]	Re-Os age on sample (A1606) 1m below 'Carbonate B' of the Doushantuo Formation at Wenghui section, Yangtze Gorges, South China (sample A1606). Initial ^{187}Os/^{186}Os = 1.81 ± 0.02. (n = 9)	(Yang et al., 2021)
587.2 ± 3.3 [3.6]	Re-Os age on sample (F1404) 58m above the base of the Doushantuo Formation at Jiulongwan section, Yangtze Gorges, South China (sample F1404). Initial ^{187}Os/^{186}Os = 0.90 ± 0.02. (2σ age, MSWD = 1.1, n = 6)	(Yang et al., 2021)
612.46 ± 0.62 (0.67) [0.94]	Zircon U-Pb CA-ID-TIMS age (re-interpreted as a maximum deposition age for detrital zircons in a mudstone layer) at the Unit 4/5 contact of the Doushantuo Fm at Zhangcunping section, Hubei. Carbonate below the dated horizon records a negative $\delta^{13}C_{carb}$ excursion.	Original SIMS age of (Zhou et al., 2017a) updated by (Yang et al., 2021)
614 ± 7.6	Zircon U-Pb SHRIMP age of a tuff bed in the Doushantuo Formation at Wangjiagou section, Zhangcunping, Hubei (sample 7527). Tuff bed occurs between beds 3 and 4, below an erosional unconformity in the middle	(Liu et al., 2009), updated by (Schmitz, 2012)

	Doushantuo Fm (Member II). Eighteen single grain analyses. Liu et al. (2009) initially reported an age of 614 ± 7.6 Ma (MSWD = 2.3, n = 18).	
632.48 ± 1.02	Zircon U-Pb CA-ID-TIMS age of a tuff bed in the lower Doushantuo Formation (at top of black shale unit, ~9m above the Nantuo-Doushantuo contact) at Jijiawan (Jiuqunao) section (sample YG-04-2). Three concordant (of 9 total) single grain analyses. Condon et al. (2005) initially reported an age of 632.50 ± 0.48 Ma (MSWD = 0.38, n = 3).	(Condon et al., 2005) updated by (Schmitz, 2012)
634.57 ± 0.88 (0.90) [1.61]	Zircon U-Pb CA-ID-TIMS of an ~20cm thick grey tuffaceous mudstone within the top of the Nantuo diamictite at Eshan section, eastern Yunnan (sample ES-1). Four concordant analyses (MSWD = 1.4, n = 4 of 7).	(Zhou et al., 2019)
635.21 ± 0.59 (0.61) [0.92]	Zircon U-Pb CA-ID-TIMS age of a tuff deposit (~30m below the contact with the Keilberg cap dolostone) interbedded with the basinal equivalent of the Ghaub Formation glacial diamictite, Navachab section, norther Namibia (sample NAV-00-2B). Five single grain analyses (MSWD = 3.4, n = 5).	(Prave et al., 2016)
635.26 ± 1.07	Zircon U-b CA-ID-TIMS age of a tuff bed at the contact surface between the lower and upper part of the cap dolomite, overlying the Nantuo glacial diamictite at the Wuhe-Gaojiaxi section, Yangtze Gorges (sample YG-04-15). Three concordant (of 18) single grain analyses. (Condon et al., 2005) initially reported an age of 635.23 ± 0.57 Ma (MSWD = 0.28, n = 3).	(Condon et al., 2005) recalculated by (Schmitz, 2012)
639.29 ± 0.26 (0.31) [0.75]	Zircon U-Pb CA-ID-TIMS age of tuff deposit interbedded with the Ghaub	(Prave et al., 2016)

	glacial diamictite (~15m below the base of the Keilberg cap carbonate), Duurwater section, northern Namibia (sample DW-1). Middle of three ash beds. Nine single grain analyses (MSWD = 2.6, n = 9)	

Table S3.

Key fossil First Appearance Datums (FADs) and stratigraphic distributions [including FADs and Last Appearance Datums (LADs)].

Entries highlighted in grey indicate siliciclastic units that lack $\delta^{13}C_{carb}$ chemostratigraphic control.

Region	**Formation**	**Details**	**Reference**
Palaeopascichnus spp. stratigraphic distribution			
Siberia, Yudoma-Maya Confluence	Aim Fm	middle siliciclastic part	(Ivantsov, 2017)
Siberia, Khorbusuonka River	Khatyspyt Fm	upper Mb3, Mb 4	(Kolesnikov et al., 2018)
Gondwana, South Australia	Wonoka Fm	50m below the top, Unit 8	(Haines, 2000)
Gondwana, South Australia	Pound sGr, Rawnsley Quartzite, Ediacara Mb		(Droser et al., 2019)
Gondwana, Namibia	Schwarzrand sGr	middle part	(Darroch et al., 2016) (*Shaanxilithes*) but see (Darroch et al., 2021) for alternative interpretation.
Gondwana, Namibia	Upper Omkyk Mb	middle part	(Macdonald et al., 2014) (*Zoophycos*) but see (Darroch et al., 2021) for alternative interpretation.
Gondwana, Brazil, Itajaí Basin	Depositional sequence 1	about level 563±0.3 Ma	(Becker-Kerber et al., 2020)
Avalonia, Newfoundland, Burin Peninsula	Chapel Island Fm	lower Mb 2A	(Gehling et al., 2001)
Avalonia, Newfoundland, Avalon Peninsula	Fermeuse Fm	upper part	(Gehling et al., 2000)
Avalonia, Newfoundland, Bonavista Peninsula	Rocky Harbour Fm	Pre-date Gaskiers-equivalent Trinity 'facies' diamictite	(Liu and Tindal, 2021)
Avalonia, UK, South Wales, Dyfed	Coomb Volcanic Fm		(Cope, 1983)
South China, Anhui, Xiuning & Yixian counties	Lantian Fm	Mb 2	(Wan et al., 2014; Yuan et al., 2011)
Baltica, Central Urals, Sylvitsa River	Sylvitsa Gr (Perevalok & Chernyi Kamen fms)		(Kolesnikov et al., 2018)
Baltica, South Urals	Basa & Zigan fms		(Becker, 2010; Kolesnikov et al., 2015)
Baltica, White Sea	Valday Gr (Lyamtsa, Verkhovka, Zimnie Gory & Erga fms)	uppermost Lyamtsa Fm; above 559 Ma	(Fedonkin, 1990, 1976; Fedonkin et al., 2007; Grazhdankin, 2014)
Baltica, Ukraine, Podolia	Mogiliv-Podilsky Gr (Mogiliv Fm)		(Fedonkin, 1990; Palij, 1976)
Baltica, Moldova	Kanilovka Gr	Komarovo beds	(Ivantsov et al., 2015; Palij, 1976)

Baltica, Norway, Finnmark, Digermulen Peninsula	Stáhpogieddi Fm	Indreelva & Manndrapselva mbs	(Jensen et al., 2018; McIlroy and Brasier, 2017)
? Baltica, Poland, Lublin	Lublin Fm		(Pacześna, 1986)

Nenoxites (=*Shaanxilithes*) spp. stratigraphic distribution			
Siberia, Yudoma River, Nuuchchalakh	Aim Fm	middle calcareous siltstone part	(Zhuravlev et al., 2009) (*Gaojiashania*)
Siberia, Khorbusuonka River	Khatyspyt Fm	upper part	(Rogov et al., 2012)
South China, Shaanxi (Gaojiashan & Lijiagou sections)	Dengying Fm	Gaojiashan Mb, lower part	(Cai et al., 2011) (*Shaanxilithes*)
South China, Yunnan, Chengjiang & Jinning counties	Yuhucun Fm	basal Yuhucun Fm, Jiucheng Mb	(Zhang et al., 2015) (*Shaanxilithes*); AZ field 2018
South China, Guizhou	Taozichong Fm		(Cai et al., 2011) (*Shaanxilithes*)
South China, Hunan (Ganziping & Liujiata sections), Guizhou (Jiumen & Sifangjing sections)	Liuchapo Fm		(Luo and Miao, 2020)
South China, Guangxi (Silikou section)	Laobao Fm	lower part	(Luo and Miao, 2020)
South China, Anhui (southern)	Piyuancun Fm	upper part	(Luo and Miao, 2020)
North China, Ningxia Hui AR (Helanshan area, Suyukou section)	Zhengmuguan Fm	Slate Mb, upper part	(Shen et al., 2007) (*Shaanxilithes, Palaeopascichnus*)
North China, Qinghai (Chaidam Basin, Quanjishan section)	Zhoujieshan Fm	middle part	(Shen et al., 2007) (*Shaanxilithes*)
India, Lesser Himalaya, Nigali Dhar Syncline	Krol Gr, Earthy Dolomite Mb & Tal Gr, Shaliyan Fm, Earthy Siltstone Mb	basal Tal Gr	(Tarhan et al., 2014) (*Shaanxilithes*)
Baltica, White Sea	Valday Gr (Lyamtsa, Verkhovka, Zimnie Gory & Erga fms)	uppermost Lyamtsa Fm, basal Erga Fm; 559-550 Ma	(Fedonkin, 1990, 1976; Grazhdankin, 2014; Grazhdankin and Krayushkin, 2007)

Pteridinium spp. stratigraphic distribution			
Baltica, White Sea	Upper Erga Fm	upper part, above 550.2±4.6 Ma. Radiometric age not incorporated into model due to large uncertainty.	(Ivantsov, 2011)
Laurentia, North Carolina, Carolina Slate Belt	Lower Floyd Church Fm	above ash bed dated at 540.6 ± 1.2 Ma (multigrain fraction air abrasion Pb/Pb age) (Ingle et al., 2003). This age is not included in our age model as it has not been corrected for the updated U decay constant or updated laboratory and analytical methodology. Analysis of an andesite at the base of the underlying Flat Swamp Member (immediately overlying the unnamed mudstone Member of the upper Cid Fm)	(Weaver et al., 2006)

		yields a zircon U-Pb ID-TIMS age of 547 ± 2 Ma (sample #00CT-03, MSWD = 0.55, n = 6) (Hibbard et al., 2009). Temporal placement of this fossil occurrence is poorly constrained.	
Laurentia, Mackenzie Mountains, Northwest Territories	Blueflower Formation	Sekwi Brook section. Age range poorly constrained due to sparse distribution of carbonate beds for chemostratigraphy (see Macdonald et al., 2013). Age constrained by lower Blueflower Re-Os age of 567.3 ± 3.0 Ma (Rooney et al., 2020) and unconformably overlying terminal Ediacaran Risky Fm, which records the BACE.	(Narbonne and Aitken, 1990; Sperling et al., 2016)
Gondwana, Namibia, Witputs Subbasin	Spitskop Member, Vingerbreek Member, Niederhagen Member, Upper Kliphoek (Aar) Member.	Farm Swartpunt, 25km north of Farm Helmeringhausen (Kosos?), Farm Aar. Temporal range spans >547.32 Ma (Bowring et al., 2007), to fossiliferous horizon in upper Spitskop Member at Swartpunt constrained between ca. 539.6 and 538.58 Ma (Linnemann et al., 2019), within interval interpreted as coincident with the BACE nadir.	(Darroch et al., 2021; Gürich, 1933, 1930), full reference list in SI of (Bowyer et al., 2020)
South China, 3 Gorges area, Hubei	Dengying Fm, Shibantan Mb	$\delta^{13}C$ positive excursion	(Chen et al., 2014)
Gondwana, South Australia, Flinders Ranges	Ediacara Member, Rawnsley Quartzite	Poor temporal constraint on Rawnsley Quartzite. However, mixed Nama/White Sea assemblage may indicate pre-550 Ma age.	(Gehling and Droser, 2013)

Rangea spp. stratigraphic distribution			
Baltica, White Sea	Upper Erga Fm	upper part, above 550.2±4.6 Ma. Radiometric age not incorporated into model due to large uncertainty.	(Ivantsov, 2011)
Gondwana, Namibia, Witputs subbasin	Niederhagen Member, Kliphoek Member.	Farms Kuibis, Vrede, Aar and Chamis. >547.32 Ma (Bowring et al., 2007), to >542.68 ± 2.8 (*59*).	(full reference list in SI of (Bowyer et al., 2020)
South China, 3 Gorges area, Hubei	Dengying Fm, Shibantan Member	$\delta^{13}C$ positive excursion	(Chen et al., 2014)
Gondwana, South Australia, Flinders Ranges	Ediacara Member, Rawnsley Quartzite	Poor temporal constraint on Rawnsley Quartzite. However, mixed Nama/White Sea assemblage may support pre-550 Ma age.	(Gehling and Droser, 2013)

Ernietta spp. stratigraphic distribution			
Gondwana, Namibia, Witputs subbasin	Upper Kliphoek (Aar) Member (reassignment of Farm Hansburg samples to Kliphoek Member after (Gibson et al., 2019; Maloney et al., 2020), Spitskop Member	Farms Plateau, Aar, Wegkruip, Hansburg and Swartpunt >547.32 Ma (Bowring et al., 2007), potentially to fossiliferous horizon in Spitskop Member constrained between ca. 539.6 Ma and 538.58 Ma (Linnemann et al., 2019). Putative *Ernietta* sample at Farm Swartpunt	(Darroch et al., 2021, 2015; Elliott et al., 2016; Gibson et al., 2019; Maloney et al., 2020; Pflug, 1966), full reference list in SI of (Bowyer et al., 2020)

		(Darroch et al., 2015) tentatively defines LAD of this form.	
Laurentia, Montgomery Mountains, near Johnnie townsite	Lower Wood Canyon Formation	Erniettomorph fossils recovered from sandstones that underly and are interbedded with ooidal dolostone unit that records the onset of the BACE (Smith et al., 2017).	(Smith et al., 2017)

Swartpuntia spp. stratigraphic distribution			
Laurentia, North Carolina	Cid Fm, unnamed mudstone member.	Putative (?) *Swartpuntia* occurrence below ash bed dated at 540.6 ± 1.2 Ma (multigrain fraction air abrasion Pb/Pb age) (Ingle et al., 2003). This age is not included in our age model as it has not been corrected for the updated U decay constant or updated laboratory and analytical methodology. Furthermore, analysis of an andesite at the base of the Flat Swamp Member (immediately overlying the unnamed mudstone Member of the Cid Fm) yields a zircon U-Pb ID-TIMS age of 547 ± 2 Ma (sample #00CT-03, MSWD = 0.55, n = 6) (Hibbard et al., 2009). Temporal placement of this fossil occurrence is poorly constrained.	(Weaver et al., 2006)
Laurentia, Kelso Mountains, California	Upper Member of Lower Wood Canyon Fm	LACMIP 12726. Uncertain precise temporal placement within the Wood Canyon Fm. Approximately coeval with or immediately preceding BACE, based on $\delta^{13}C_{carb}$ chemostratigraphy of (Smith et al., 2017). Putative *Swartpuntia* affinity questioned by (Smith et al., 2017) based on lack of preserved stalk or figured full specimens.	(Hagadorn et al., 2000; Hagadorn and Waggoner, 2000)
Laurentia, White Mountains, California	Middle Member of Poleta Fm	UCMP 37450. Uncertain precise temporal placement relative to the Wood Canyon Fm. Approximately coeval with or immediately preceding BACE, based on $\delta^{13}C_{carb}$ chemostratigraphy of (Smith et al., 2017). Putative *Swartpuntia* affinity questioned by (Smith et al., 2017) based on lack of preserved stalk or figured full specimens.	(Hagadorn et al., 2000)
Laurentia, Montgomery Mountains, Nevada	Wood Canyon Fm	lower member, above cloudinids occurring in the Stirling Quartzite	(Hall et al., 2020)
Gondwana, Namibia, Witputs subbasin	Spitskop Member, Feldschuhhorn Member.	Farm Swartpunt. Occurrence in Feldschuhhorn Member (Jensen et al., 2000) suggests range > ca. 540.095 Ma extending to fossiliferous horizon in Spitskop Member constrained between ca. 539.6 Ma and 538.58 Ma (Linnemann et al., 2019).	(Darroch et al., 2015; Jensen et al., 2000; Narbonne et al., 1997)

Cloudina spp. and other cloudinid stratigraphic distribution			
Siberia, Yudoma River, Kyra-Ytyga River mouth	Yudoma Gr, Ust'-Yudoma Fm	upper part /upper $\delta^{13}C$ plateau/inferred to be below BACE excursion	*Cloudina* ex gr. *C. riemkeae* (Zhu et al., 2017; Zhuravlev et al., 2012)

West Siberian Plate	Kotodzha and Raiga fms	uppermost Katadzha Fm to middle Raiga Fm. Uncertain temporal placement due to lack of associated δ^{13}C data.	*Cloudina hartmanae* (Kontorovich et al., 2008)
Altay Sayan Foldbelt, Eastern Sayan	Anastas'ino Fm	Upper part of mb 3. Uncertain temporal placement due to lack of associated δ^{13}C data.	*Cloudina* sp. (Kheraskova and Samygin, 1992; Terleev et al., 2011)
Altay Sayan Foldbelt, Mountain Shoria	West Siberia & Belka fms	Uncertain temporal placement due to lack of associated δ^{13}C data.	*Cloudina* sp. (Bagmet, 1994; Terleev et al., 2011)
Altay Sayan Foldbelt, Kuznetsk Alatau	Tarzhul' Fm	Middle part. Uncertain temporal placement due to lack of associated δ^{13}C data.	*Cloudina* sp. (Terleev et al., 2011)
Mongolia, Zavkhan Terrane	Zuun-Arts Fm	Basal part. Uncertain temporal placement due to lack of associated δ^{13}C data, but within interval ca. 540 – 539 Ma according to Model C.	*Zuunia chimidtsereni* (Yang et al., 2020)
Kazakhstan, Karatau-Naryn Terrane	Chulaktau Fm	Aksai & Karatau mbs with *Anabarites* and *Protohertzina*. May post-date the BACE, however this is difficult to confirm due to the unsuitable lithology of the Chulukatau Fm for robust use in δ^{13}C chemostratigraphy.	*Rajatubus costatus* (B. Yang et al., 2016)
Gondwana, Namibia, Zaris & Witputs subbasins	Nama Gr, Kuibus & Schwarzrand sgrs	Zaris Fm, upper Omkyk & lower Hoogland mbs, Urusis Fm, Feldschuhhorn & Spitskop mbs, Dabis Fm, Mara Mb />547.32 Ma –538.58±0.19 Ma/	*Cloudina hartmanae, C. riemkeae* (Bowring et al., 2007; Bowyer et al., 2017; Grotzinger et al., 2005, 1995; Linnemann et al., 2019; Wood et al., 2017; Wood and Curtis, 2015); full references in SI of (Bowyer et al., 2020)
Gondwana, Brazil, Mato Grosso do Sul	Corumbá Gr	middle & upper Tamengo Fm	*Cloudina lucianoi, C. carinata* (Adôrno et al., 2019, 2017; Becker-Kerber et al., 2017)
Gondwana, Paraguay	Itapucumí Gr, Tagatiya Guazú Fm	Available low-resolution δ^{13}C data suggest placement in interval between 547 and 543 Ma.	*Cloudina* sp. (Warren et al., 2017)
Gondwana, Uruguay, Rio de la Plata Craton	Arroyo del Soldado Gr	upper Yerbal Fm. Note ongoing uncertainties in the age of the Arroyo del Soldado Group (e.g. Pecoits et al., 2016)	*Cloudina* sp.? (Gaucher, 2000; Gaucher et al., 2003). Ongoing uncertainty in affinity due to a dearth of figured material at high resolution.
Gondwana, Oman	Huqf Supergr, Ara Gr	A1-A3, 546.72±0.21 Ma – 542.33±0.12 Ma	*Cloudina* cf. *C. hartmanae* (Amthor et al., 2003; Bowring et al., 2007; Conway Morris et al., 1990)
Gondwana, South China, southern Shaanxi, Ningqiang County	Dengying Fm	upper part of the middle Gaojiashan Mb / δ^{13}C positive excursion/ – Beiwan Mb /at plateau, below δ^{13}C BACE negative excursion/ above 548±8 Ma (detrital) – 538.8 Ma	*Cloudina hartmanae, C. ningqiangensis, C. xuanjiangpingensis* (Cai et al., 2010; Cui et al., 2019; Hua et al., 2005)

Gondwana, South China, Hubei, Yichang County	Kuanchuanpu Fm	basal part with *Anabarites* and *Protohertzina*. Occurs below a large negative $\delta^{13}C$ excursion thought to postdate the BACE. No raw $\delta^{13}C$ data have been published to incorporate into our age model but see $\delta^{13}C$ profile in (Steiner et al., 2020) (their figure 11). According to the model of (Steiner et al., 2020) and (B. Yang et al., 2016), cloudinids occur coincident with, or slightly above the BACE in the lowermost Kuanchuanpu Fm, with a minimum age LAD equivalent to the upper Spitskop Member, Swartpunt section (Nama Group, Namibia). Alternatively, the negative excursion at the top of the Kuanchuanpu Fm may represent the BACE, with SSFs of the *Anabarites trisulcatus – Protohertzina anabarica* Zone extending down into the late Ediacaran, similar to the record from SE Siberia. To be confirmed.	*Cloudina hartmanae* (Steiner et al., 2020; B. Yang et al., 2016)
Gondwana, Spain, East Galician-Castilian Zone, Valdelacasa Anticline	Río Huso Gr	Membrillar olistostrome (mostly siliciclastic with a few carbonate olistoliths and silicified *Cloudina*)	*Cloudina carinata* (Cortijo et al., 2010; Vidal et al., 1994)
Gondwana, Spain East Lusitanian-Alcudian Zone, Abenójar & Navalpino anticlines	Ibor Gr	Villarta Formation	*Cloudina hartmanae, C. carinata* (Álvaro et al., 2019; Zhuravlev et al., 2012)
Laurentia, W Canada, British Columbia, Rocky Mts	Windermere Supergr, Miette Gr, Byng Fm	Uppermost part	*Cloudina* sp. (Hofmann and Mountjoy, 2001)
Laurentia, Nevada & California	Deep Spring Fm	Lower part	*Cloudina dunfeei* (Signor et al., 1987)
Laurentia, Nevada	Wood Canyon & Deep Spring fms	Esmeralda Mb (Deep Spring Fm), lower mb (Wood Canyon Fm)	*Saarina hagadorni* (Selly et al., 2020)
Laurentia, Mexico, Sonora	La Ciénega Fm	Unit 1 contains both *Cloudina* and *Sinotubulites* below the level dated at 539.40 ± 0.23 (0.35) Ma (Hodgin et al., 2020) (maximum depositional age)	*Cloudina* sp. (McMenamin, 1985; Sour-Tovar et al., 2007)
Baltica, White Sea area	Erga Fm	upper part, above 550.2±4.6 Ma. Radiometric age not incorporated into model due to large uncertainty.	*Saarina* sp. (Grazhdankin and Maslov, 2015; Ivantsov, 2011)
Baltica, Leningrad region		Rovno Horizon, lowermost Cambrian?	*Saarina tenera* (Sokolov, 1967)

Namacalathus hermanastes stratigraphic distribution			
Gondwana, Namibia, Zaris & Witputs subbasins	Nama Gr, Kuibus & Schwarzrand sgrs	Zaris Fm, upper Omkyk & lower Hoogland mbs, Urusis Fm, Feldschuhhorn & Spitskop mbs />547.32 Ma – 538.58±0.19 Ma/	(Bowring et al., 2007; Bowyer et al., 2017; Grotzinger et al., 2000, 1995; Linnemann et al., 2019; Penny et al., 2017; Wood et al., 2015); see SI of (Bowyer et al., 2020) for full references. FB field observation *in situ* at summit of Swartpunt section (image available upon request).
Gondwana, Oman	Huqf Supergr, Ara Gr	A2-A3, above 546.72±0.21 Ma – 542.33±0.12 Ma /δ^{13}C positive excursion/	(Amthor et al., 2003; Bowring et al., 2007)
Gondwana, Paraguay	Itapucumí Gr, Tagatiya Guazú Fm	Available low-resolution δ^{13}C data suggest placement in interval between 547 and 543 Ma.	(Warren et al., 2017)
Laurentia, W Canada, British Columbia, Rocky Mts	Windermere Supergr, Miette Gr, Byng Fm	Uppermost part	(Hofmann and Mountjoy, 2001)

Treptichnus pedum FADs			
Mongolia, Zavkhan Terrane	Bayan-Gol Fm, contact between members BG3 and BG4	~275m above the nadir of the BACE. ~250m above the FAD of Anabaritids. Approximately coincident with peak 4p.	(Smith et al., 2015)
Avalonia, Burin Peninsula, Newfoundland	Lowest occurrence: 2m below lithofacies association (/'member') 2 of the Chapel Island Formation at Fortune Head.	Largely unconstrained by δ^{13}C chemostratigraphy due to dominance of siliciclastic deposits (see Brasier et al. (1992) for available data). >>530.02 ± 1.2 Ma (Isachsen et al., 1994, recalculated in Schmitz, 2012) based on approximate age of Chapel Island Formation lithofacies association (Member) 5 (Mystery Lake Member) after regional litho- and biostratigraphic correlation (Landing, 1994, 1991) with sections in Saint John, New Brunswick.	(Brasier et al., 1994; Gehling et al., 2001; Geyer and Landing, 2017; Landing, 1991; Landing et al., 1988)
Gondwana, Namibia, Witputs subbasin	Nama Group, Schwarzrand Subgroup, Farm Sonntagsbrunn, Farm Vergelee (bordering	Nomtsas Fm. ≤538.58 ± 0.19 (0.24) [0.62] Ma. Maximum age based on radiometric dating of tuff bed in presumed-correlative lower Nomtsas deposits on Farm	(Germs, 1972; Geyer and Uchman, 1995; Grotzinger et al., 1995; Wilson et al., 2012), see updated ichnofossil biostratigraphy of (Darroch et al., 2021)

	Sonntagsbrunn to SE)	Swartkloofberg (Linnemann et al., 2019)	
South China, NE Yunnan	Meishucun section, near Jinning	Lower Zhongyicun Mbr (Zhujiaqing Fm). Above the nadir of the BACE, within interval of highly variable $\delta^{13}C$ and widespread phosphorite deposition across the platform.	(Zhu et al., 2001)
Siberia, Northwestern slope of Olenek Uplift, Khorbusuonka River	Upper Syhargalakh Fm.	Upper Syhargalakh Fm. Above maximum age of 542.8 ± 1.30 Ma from volcanic breccia of the Tas-Yuryakh volcanic complex (Bowring et al., 1993; Maloof et al., 2010). Uncertainty in this age is noted in Table S1.	(Rogov et al., 2015)
Laurentia, California	Immediately above second dolomite marker bed in the lower member of the Wood Canyon Fm	Above nadir of the BACE recorded in the second dolomite marker bed of the lower member, Wood Canyon Fm.	(Smith et al., 2017)
Laurentia, Mexico, Sonora	Lowermost Cerro Rajón Formation.	Above sandy, hematite-rich dolostone bed dated at 539.40 ± 0.23 (0.35) Ma (interpreted as maximum depositional age). Above recovery from the BACE (Model A), within BACE interval (Model B), or eruption of tuffaceous material pre-BACE followed by bed re-deposition coincident with BACE at ~536.25 Ma (Model C).	(Hodgin et al., 2020)

Anabarites trisulcatus FADs			
Mongolia, Zavkhan Terrane	Lowermost Bayan-Gol Fm, BG2 Member	Lowermost phosphorite unit of Bayan-Gol Fm, positive $\delta^{13}C$ excursion 2p. Base of transitional recovery interval following BACE/'1n'.	(Smith et al., 2015)
Avalonia, Burin Peninsula	Chapel Island Fm, Lithofacies association (/'Member') 4	Largely unconstrained by $\delta^{13}C$ chemostratigraphy due to dominance of siliciclastic deposits (see ((Brasier et al., 1992)) for available data). >>530.02 ± 1.2 Ma (Isachsen et al., 1994, recalculated in Schmitz, 2012) based on approximate age of Chapel Island Formation lithofacies association (Member) 5 (Mystery Lake Member) after regional litho- and biostratigraphic correlation (Landing, 1994, 1991) with sections in Saint John, New Brunswick.	*Tiksitheca korobovi* in (Landing, 1988)
Laurentia, Yukon	Uppermost Ingta Fm	Below FAD *T. pedum* in basal Vampire Fm, above recovery from BACE? Temporal position poorly constrained.	(Nowlan et al., 1985; Pyle et al., 2006)

Gondwana, South China, Hubei, Yichang County	Kuanchuanpu Fm	Basal part with *Protohertzina* and cloudinids. Occurs below a large negative $\delta^{13}C$ excursion thought to postdate the BACE. No raw $\delta^{13}C$ data have been published to incorporate into our age model but see $\delta^{13}C$ profile in (Steiner et al., 2020) (their figure 11). According to the model of (Steiner et al., 2020) and (B. Yang et al., 2016), cloudinids occur coincident with, or slightly above the BACE in the lowermost Kuanchuanpu Fm, with a minimum age LAD equivalent to the upper Spitskop Member, Swartpunt section (Nama Group, Namibia). Alternatively, the negative excursion at the top of the Kuanchuanpu Fm may represent the BACE, with SSFs of the *Anabarites trisulcatus – Protohertzina anabarica* zone extending down into the late Ediacaran, similar to the record from SE Siberia. To be confirmed.	(Steiner et al., 2020; B. Yang et al., 2016)
Gondwana, South China, Hubei	Middle – upper Yanjiahe Formation, Gunziao section	*Anabarites* occurs above nadir of BACE, but *Anabarites trisulcatus – Protohertzina anabarica* Zone begins below nadir of BACE.	(Steiner et al., 2020)
Gondwana, South China, Yunnan	Daibu Member	*Anabarites trisulcatus – Protohertzina anabarica* Zone begins below nadir of BACE	(Steiner et al., 2020; B. Yang et al., 2016)
Gondwana, South China, southern Shaanxi, Ningqiang County	Dengying Formation	Beiwan Mb /at plateau, below $\delta^{13}C$ BACE negative excursion/ above 548±8 Ma (detrital) – 538.8 Ma	(Cai et al., 2019)
Kazakhstan, Karatau-Naryn Terrane	Chulaktau Fm	Aksai & Karatau mbs	(B. Yang et al., 2016)
Siberia, Yudoma River, Kyyra-Ytyga River mouth	Yudoma Gr, Ust’-Yudoma Fm	upper part below BACE	(Zhu et al., 2017)
Siberia, western Anabar Uplift, Kotuykan River	Manykai Fm, Bed III	lower part /$\delta^{13}C$ positive excursion 2p	(Kaufman et al., 1996)

Protohertzina anabarica FAD			
Siberia, Yudoma River, Kyyra-Ytyga River mouth	Yudoma Gr, Ust’-Yudoma Fm	upper part below BACE	(Zhu et al., 2017)
Siberia, Uchur-Maya region, Dzhanda River	Yudoma Gr, Ust’-Yudoma Fm	25-30 m below the top	(Khomentovskiy et al., 1990)
Siberia, Uchur-Maya region, Nimnekey River	Yudoma Gr, Ust’-Yudoma Fm	80 m below the top	(Khomentovskiy and Karlova, 1991)
Siberia, western Anabar Uplift, Kotuykan River	Manykai/Nemakit-Daldyn Fm	lower part /$\delta^{13}C$ positive excursion 2p peak/	(Kaufman et al., 1996; Kouchinsky et al., 2017)
Siberia, eastern Anabar Uplift, Bol’shay and Malaya Kuonamka rivers	Manykay Fm	lower part /below $\delta^{13}C$ excursion 2p bottom ???/	(Kouchinsky et al., 2017)

Siberia, Olenek Uplift	Syhargalakh Fm (Kessyuse Gr)	upper part, above 543.9±0.24 Ma level. Uncertainty in this radiometric constraint noted in Table S1.	(Nagovitsin et al., 2015)
West Siberian Plate, Tomsk region	Churbiga Fm	lower part	(Novozhilova and Korovnikov, 2019)
Mongolia, Zavkhan Terrane	Bayan-Gol Fm	lower part /$\delta^{13}C$ positive excursion 2p peak ???/	(Esakova and Zhegallo, 1996; Smith et al., 2015)
Kazakhstan, Karatau-Naryn Terrane	Chulaktau Fm	Aksai & lower Karatau mbs with cloudinid *Rajatubus*	(Missarzhevsky, 1973; B. Yang et al., 2016)
Gondwana, South China, Yunnan, Huize County	Zhujiaqing Fm	basal Zhongyicun Mb /$\delta^{13}C$ P2-P3 interval/	(Li et al., 2013; Yang et al., 2014)
Gondwana, South China, Shaanxi	Kuanchuanpu Fm	lower & middle part	(Steiner et al., 2007)
Gondwana, South China, Hubei, Yichang County, Yangtze Gorges	Yanjiahe Fm	Dolostone Unit 2 & Tianzhushan Mb /$\delta^{13}C$ positive excursion/	(Steiner et al., 2020)
Gondwana, South China, Sichuan	Maidiping Fm	lower part	(Steiner et al., 2020)
Gondwana, South China, Hunan	Hetang Fm	basal chert unit	(Yang et al., 2014)
Gondwana, South China, Anhui	Hetang Fm	basal part	(Steiner et al., 2003)
Gondwana, Tarim, Xinjiang	Yurtusu Fm		(Zhang et al., 2020)
Gondwana, India, Lesser Himalaia, Mussoorie Syncline	Tal Gr	Lower Tal Gr, basal part	(Brasier and Singh, 1987; Hughes, 2016)
Iran, Alborz Mts	Soltanieh Fm	Lower Shale Mb, lower part /$\delta^{13}C$ negaitive excursion above EPIP/	(Hamdi, 1995; Kimura et al., 1997)
Gondwana, Spain East Lusitanian-Alcudian Zone, Abenójar Anticline	Ibor Gr	Villarta Fm, with *Cloudina*	*Protohertzina* sp. (Simón, 2018)
Avalonia, Newfoundland, Burin Peninsula	Chapel Island Fm	mb 4	(Landing et al., 1989)
Baltica, Estonia	Lontova & coeval Voosi fms	Kestla Mb	*Protohertzina compressa* in (Slater et al., 2018) /organic compression/
Laurentia, W Canada, Mackenzie Mts	Backbone Ranges Fm	(former Map Unit 11) /above $\delta^{13}C$ negative excursion/	(Conway Morris and Fritz, 1980; Narbonne et al., 1994)
Laurentia, W Canada, Wernecke Mts	Ingta Fm	upper part	(Pyle et al., 2006)

Aldanella attleborensis FADs [including its junior synonyms *A. kunda* (Öpik, 1926); *A. yanjiaheensis* (Chen, 1984); *A. costata* (Missarzhevsky, 1989); *A. patelliformis* (Bokova, 1990; B. Yang et al., 2016)].			
Siberia, Aldan River, Dvortsy section	Pestrotsvet Fm	Bed 15, basal part of the formation /beginning of $\delta^{13}C$ Cycle II = -1‰/	(Brasier et al., 1994; Parkhaev and Karlova, 2011; Semikhatov et al., 1970)

Siberia, Selinde River	Pestrotsvet Fm	basal part /$\delta^{13}C$ excursion I'/	(Kouchinsky et al., 2005; Parkhaev and Karlova, 2011; Repina et al., 1988)
Siberia, Igarka region, Sukharikha River	Sukharikha Fm	uppermost part (occurs above in the lower Krasny Porog Fm) /$\delta^{13}C$ excursion 7p/	(Kouchinsky et al., 2007; Parkhaev and Karlova, 2011)
Siberia, western Anabar Uplift, Kotuy River	Medvezh'ya Fm	lower part /$\delta^{13}C$ excursion I'/	(Kouchinsky et al., 2017; Parkhaev and Karlova, 2011)
Siberia, eastern Anabar Uplift, Bol'shay and Malaya Kuonamka rivers	Manykay Fm	upper part (occurs above in the lower Emyaksin Fm) /below $\delta^{13}C$ excursion I'/	(Kouchinsky et al., 2017; Parkhaev and Karlova, 2011)
Siberia, Olenek Uplift	Mattaia Fm (Kessyuse Gr)	middle mb, below 529.7±0.3 Ma level	(Sarsembaev and Marusin, 2019)
Siberia, Noril'sk area	Polba Fm	uppermost part	(Parkhaev, 2014)
Siberia, Kolyma Uplift	Kirpichnaya Fm	lower part	(Tkachenko et al., 1987)
Siberia, Taimyr Peninsula	Graviinorechenskaya Gr		(Parkhaev and Karlova, 2011)
Mongolia, Zavkhan Terrane	Khairkhan Fm	reworked material	(Missarzhevsky, 1973)
Gondwana, South China, Yunnan, Huize County	Zhujiaqing Fm	Dahai Mb	(Parkhaev and Karlova, 2011)
Gondwana, South China, Hubei, Yichang County, Yangtze Gorges	Yanjiahe Fm	Unit 4 /$\delta^{13}C$ positive excursion/	(Steiner et al., 2020)
Gondwana, South China, Sichuan, Emei County	Maidiping Fm	upper part	(Parkhaev and Karlova, 2011)
Gondwana, Tarim, Xinjiang	Yurtusu Fm		(Parkhaev, 2019b)
Avalonia, Newfoundland, Burin Peninsula	Chapel Island Fm	upper mb 3 /and mb 4/	(Landing et al., 1989)
Avalonia, Massachusetts	Weymouth Fm	lower mb, below 530.7±0.9 Ma level	(Landing, 1989, 1988; Landing et al., 1998)
Baltica, Estonia	Lontova Fm	Kestla Mb	*Aldanella kunda* (Öpik, 1926) in (Isakar and Peel, 2007)
Baltica, Norway, Troms	Dividal Gr	Mb D (*Platysolenites antiquissimus* Zone)	(Føyn and Glaessner, 1979)

Watsonella crosbyi FADs			
Siberia, Aldan River, Dvortsy section	Pestrotsvet Fm	Bed 15, basal part of the formation /beginning of $\delta^{13}C$ Cycle II = -1‰/ (occurs up to Bed 16, 34 m above the base)	(Brasier et al., 1994; Semikhatov et al., 1970)
Siberia, Selinde River	Pestrotsvet Fm	basal part /$\delta^{13}C$ excursion I'/	(Kouchinsky et al., 2005; Repina et al., 1988)
Siberia, Igarka region, Sukharikha River	Krasny Porog Fm	lower part /beginning of $\delta^{13}C$ Cycle II = -1‰/	(Kouchinsky et al., 2007; Rowland et al., 1998)

Siberia, western Anabar Uplift, Kotuy River	Medvezh’ya Fm	lower part /δ^{13}C excursion I’/	(Landing and Kouchinsky, 2016)
Siberia, Olenek Uplift	Mattaia Fm (Kessyuse Gr)	upper mb, right above 529.7±0.3 Ma level	(Sarsembaev and Marusin, 2019)
Mongolia, Zavkhan Terrane	Bayan-Gol Fm	uppermost part /approximately δ^{13}C positive excursion 5p?/	(Esakova and Zhegallo, 1996; Smith et al., 2015)
Gondwana, South China, Yunnan, Yongshan, Xundian, Jinning & Huize counties	Zhujiaqing Fm	upper Dahai Mb, above 536.7±3.9 Ma level /δ^{13}C Cycle P or ZHUCE/	(Chen et al., 2015; Li et al., 2011; Steiner et al., 2020)
Gondwana, South China, Hubei, Yichang County, Yangtze Gorges	Yanjiahe Fm	bed 5 /δ^{13}C positive excursion/	(Guo et al., 2020; Steiner et al., 2020)
Gondwana, South China, Sichuan, Emei & Ganlu counties	Maidiping Fm	upper part /δ^{13}C positive excursion/	(Steiner et al., 2020, 2007)
Gondwana, North China, northern Shaanxi	Xinji Fm	Mb B, *Estangia* trilobite zone, Canglangpuan Stage /=lower Stage 4/	(Parkhaev, 2019b)
Gondwana, South Australia, Stansbury Basin, Fleurieu Peninsula	Mount Terrible Fm	upper part of middle mb (occurs up to the Wangkonda and lower Selick Hill fms) /suggested below δ^{13}C ZHUCE/	(Bengtson et al., 1990; Betts et al., 2018; Jacquet et al., 2017)
Gondwana, France, Montagne Noir, Avène-Mendic parautochthon	Marcou Fm	Heraultia Mb	(Devaere et al., 2013)
Avalonia, Newfoundland, Burin Peninsula	Chapel Island Fm	upper mb 3 /and above including the Bonavista Gr/	(Landing et al., 2017)
Avalonia, Massachusetts	Weymouth Fm	lower mb, below 530.7±0.9 Ma level	(Landing, 1989, 1988; Landing et al., 1998)

Cruziana ichnospp. FADs			
Siberia, Olenek Uplift	Kessyuse Gr, Mattaia Fm	about 529.7±0.3 Ma level	(Marusin et al., 2015; Nagovitsin et al., 2015)
Gondwana, South China, Yunnan, Jinning County	Zhujiaqing Fm	Zhongyicun Mb, Upper Phosphorite bed	(Weber et al., 2007)
Iran, Alborz Mts	Soltanieh Fm	Lower Shale Mb, uppermost part	(Shahkarami et al., 2017)
Gondwana, Spain, Cantabrian Zone, Cadenas Ibéricas	Embid Fm	upper part	(Gámez Vintaned et al., 2009)
Laurentia, Canada, Wernecke Mts	Vampire Fm	basal part (above Ingta Fm with *Protohertzina*)	(Narbonne and Aitken, 1995)
Laurentia, USA, Great Basin	Deep Spring Fm	upper part (Gold Point Mb)	(Ahn et al., 2011; Corsetti and Hagadorn, 2003)
Laurentia, Mexico, Sonora (Cerro Rajón section)	Puerto Blanco Fm	Unit 2, basal part (with trilobite cf. *Fallotaspis* sp.)	(Stewart et al., 1984)
Avalonia, Newfoundland, Burin Peninsula	Chapel Island Fm	upper Member 2	(Landing et al., 2017)

Baltica, Norway, Finnmark	Breidvika & Duolbasgaissa fms	Lower Breidvika Mb to Lower Duolbasgaissa Mb (below trilobite *Kijerulfia*)	(Crimes and McIlroy, 1999; McIlroy and Brasier, 2017)
Baltica, South Sweden	Mickwitzia Sandstone Mb	upper part, Interval D (with *Volborthella* and below trilobite *Holmiella*; Stage 4 ?)	(Jensen, 1997)

Archaeocyatha FADs			
(A1–B1) – archaeocyath zones equated with the Siberian lower Cambrian zonation. (? Cycle IV) – carbon-isotope cycles following the Siberian record.			
Siberia, Aldan River (Ulakan-Sulugur section)	Pestrotsvet Fm	basal Bed 12, δ^{13}C = 0‰ pre-dating negative nadir at the beginning of Cycle II (T1); *Archaeolynthus polaris, Nochoroicyathus sunnaginicus, N. virgatus, N. belvederi, N. tkatschenkoi, Cryptoporocyathus junicanensis, Cambrocyathellus tschuranicus*	(Magaritz et al., 1991; Riding and Zhuravlev, 1995)
Siberia, Selinde River	Pestrotsvet Fm	2.7 m above the base of the formation, δ^{13}C positive excursion pre-dating I'n (?ND); *Nochoroicyathus* sp., *Cambrocyathellus* sp.	(Khomentovsky and Karlova, 2002; Kouchinsky et al., 2005)
Siberia, Sukharikha River	Sukharikha Fm	uppermost part, δ^{13}C positive excursion 7p (?ND); *Archaeolynthus polaris, Nochoroicyathus sunnaginicus, N. virgatus, N. dragunovi, N. igarcaensis, Cryptoporocyathus junicanensis*	(Kouchinsky et al., 2007; Rowland et al., 1998)
Mongolia, Zavkhan Terrane (Salaany-Gol section)	Salaany-Gol Fm	45 m above the base, δ^{13}C positive excursion (? Cycle IV), Mongolian archaeocyath zone 1 (A1); *Archaeolynthus solidimurus, Tumuliolynthus musatovi, Dokidocyathus bogradiensis, Nochoroicyathus howelli, N. misertumulus, Rotundocyathus floris, Urcyathus batenensis, Sclerocyathus floridus, Tumulocyathus exiguus, Plicocyathus stellatus, Pretiosocyathus subtilis, Agyrekocyathus shoriensis, Capsulocyathus irregularis, Alataucyathus jaroschevitschi, Cambrocyathellus minutus, C. tuberculatus, Okulitchicyathus communis, Dictyocyathus confertus, Archaeopharetra smolianinovae, Spinosocyathus mongolicus, Tabulacyathellus bidzhaensis, Usloncyathus bipartita*	(Smith et al., 2015; Voronin et al., 1982)
Mongolia, Tuva-Mongolia Terrane, southern Khubsugul area	Egyin-Gol Fm	lower member (300-500 m thick), Mongolian archaeocyath zone 2 (A2); *Archaeolynthus solidimurus, Dokidocyathus bogradiensis, Nochoroicyathus howelli, Orbicyathellus bogradi, Gordonicyathus annulispinosus, Inessocyathus heterospinosus, Formosocyathus spinosus, Capsulocyathus irregularis, Loculicyathus cibus, Ardrossacyathus ornatus, Archaeopharetra smolianinovae, Usloncyathus serus*	AZ own observations
Gondwana, South China, Shaanxi (Fucheng section)	Xiannudong Fm	at the base, with trilobites of the upper *Wutingaspis-Eoredlichia* Zone (*Yunnanocephalus* Subzone) (A1);	(B. Yang et al., 2016)

		Dailycyathus xiuqiensis, Conannulofungia annuliformis, Erismacoscinus zhuyuanensis, Archaeopharetra? chengkouensis, Metacyathellus lepidus, Uslonc yathus jindingshanensis	
Gondwana, South Australia, Arrowie Basin, Wilkawillina Gorge	Wilkawillina Lm	c. 40 m above the base (A1); *Inessocyathus clarus, Erugatocyathus krusei, Archaeopharetra insculpta, Copleicyathus cymosus, Warriootacyathus wilkawillinensis, Uslonc yathus obtusus*	(Gravestock, 1984)
Gondwana, South Australia, Arrowie Basin, Mount Scott Range	Ajax Lm	c. 80 m above the base, below δ^{13}C positive excursion (? Cycle IV) (A1); *Copleicyathus cymosus, Warriootacyathus wilkawillinensis*	(Betts et al., 2018; Gravestock, 1984)
Gondwana, Morocco, Anti-Atlas Mts	Igoudine Fm	Tiout Mb (15 m above the base), 519.71±0.26 Ma, δ^{13}C peak (? Cycle IV) (A1); *Nochoroicyathus cribratus, N. crassus, Rotundocyathus* sp., *Sibirecyathus compositus, Tumulifungia marocana, Retecoscinus minutus, Erismacoscinus fasciola, E. primus, Geyericoscinus equiporus, Neoloculicyathus magnus, Dictyocyathus stipatus, D. circulus, Protopharetra taissensis, Agastrocyathus gregarius*	(Debrenne and Debrenne, 1995; Landing et al., 2020)
Gondwana, Spain, Ossa-Morena Zone, Sierra de Córdoba (Las Ermitas section)	Pedroche Fm	Mb I, basal part, archaeocyath zone I (A1); *Archaeolynthus* sp., *Cordobicyathus deserti, Nochoroicyathus cabanasi, Urcyathus* sp., *Taylorcyathus carbonelli, Morenicyathus arruzafai, Retecoscinus guadalquivirensis, Neoloculicyathus magnus, Okulitchicyathus andalusicus*	(Perejón, 1994; Perejón et al., 2014; Perejón and Moreno-Eiris, 2006)
Gondwana, France, Montagne Noir, Minervois Nappe	Pardailhan Fm	basal HI interval (A4); *Inessocyathus levis, Retecoscinus boyeri, Anthomorpha margarita, Dictyocyathus circulus, Protopharetra* cf. *polymorpha*	(Debrenne et al., 2002)
Laurentia, Canada, Mackenzie Mts	Sekwi Fm	c. 200 m above the base, S0, post-dating δ^{13}C Cycle B peak (? = Cycle VI) (B1); *Robertiolynthus handfieldi, Sekwicyathus nahanniensis, Sanarkocyathus plurimus, Cordilleracyathus blussoni, Stephenicyathus rowlandi, Protopharetra junensis, Williamicyathus colvillensis*	(Dilliard et al., 2007; Voronova et al., 1987)
Laurentia, USA, Great Basin, Nevada	Campito Fm	Montenegro Mb (upper 50 m) (A4); *Robustocyathellus? weeksi, Cordilleracyathus blussoni, Ethmophyllum whitney, Metaldetes fischeri, Metacyathellus argentus*	(Mansy et al., 1993)
Laurentia, Mexico, Sonora (Cerro Rajón section)	Puerto Blanco Fm	middle Unit 2, poorly preserved. Basal Unit 3 (B1); *Robustocyathellus? pusillus, Palmericyathus americanus, Loculicyathus polycladus, Graphoscyphia ramosa, Spirocyathella spinosa, Metaldetes* cf. *meeki*	(Debrenne et al., 1989)

Trilobita FADs

Siberia, Lena River, Zhurinsky Mys sections	Pestrotsvet Fm	47 m above the base of the section (Bed 4), beginning of $\delta^{13}C$ Cycle IV = 0‰; *Profallotaspis* sp. 54 m above the base of the section (Bed 5), beginning of $\delta^{13}C$ Cycle IV = 0.5‰; *Profallotaspis jakutensis.* 57 m above the base of the section (Bed 6), beginning of $\delta^{13}C$ Cycle IV = 1‰; *Profallotaspis jakutensis.* 73 m above the base of the section (Bed 7), $\delta^{13}C$ Cycle IV peak = 1.5‰; *Repinaella explicata.*	(Astashkin et al., 1984; Kirschvink et al., 1991)
Siberia, Selinde River	Pestrotsvet Fm	Bed 37 (95 m above the base of the formation), $\delta^{13}C$ = 0.5‰ pre-dating Cycle IV peak; *Profallotaspis privica*. Beds 38–40 within the same cycle: *P. jakutensis, Repinaella sibirica, R. explicata, Bigotinella malycanica, Nevadella* aff. *effusa*	(Kouchinsky et al., 2005; Repina et al., 1988)
Mongolia, Tuva-Mongolia Terrane, southern Khubsugul area	Egyin-Gol Fm	lower member (300-500 m thick), Mongolian archaeocyath zone 2; *Elganellus pensus, Bigotinella malycanica, Malykania murenica*	(Korobov, 1989, 1980)
Gondwana, South China, Yunnan, Jinning County (Maotianshan & Xiaolantian sections)	Yu'anshan Fm	basal "black shale member", at the beginning of $\delta^{13}C$ MICE (? Cycle IV), below the Chengjiang Biota of 518.03±0.69/0.71 Ma; *Parabadiella huoi*	(Yang et al., 2018; Zhang et al., 2001; Zhu et al., 2001)
Gondwana, South Australia, Arrowie Basin, Wilkawillina Gorge	Wilkawillina Lm	uppermost part; *Eoredlichia* sp.	(Bengtson et al., 1990)
Gondwana, South Australia, Arrowie Basin, Mount Scott Range	Ajax Lm	140 m above the base, $\delta^{13}C$ positive excursions (? Cycle IV); *Parabadiella huoi.* 200 m above the base, between $\delta^{13}C$ positive excursions (? Cycles IV and V); *Pararaia tatei, Eoredlichia shensiensis*	(Bengtson et al., 1990; Betts et al., 2018)
Gondwana, Morocco, Anti-Atlas Mts	Igoudine Fm	Tiout Mb, 519.95±0.43, trilobite fragments. 519.78±0.78 – 518.99±0.14 Ma, $\delta^{13}C$ peak (? Cycle IV); *Hupetina antiqua – /Eofallotaspis prima, Bigotina kelleri, Eladiolinania castor/ – Bigotina monningeri – Eofallotaspis tioutensis – Fallotaspis antecedens*	(Landing et al., 2020)
Gondwana, Spain, Galician-Castilian Zone, Salamanca (La Rinconada section)	Tamanes Ss	lower part; *Lunagraulos tamamensis*	(Liñán et al., 2015)
Gondwana, Spain, Ossa-Morena Zone, Sierra de Córdoba (Arroyo de Pedroche 1 section)	Pedroche Fm	Mb I, base, archaeocyath zone I; cf. *Bigotinella.* Mb I, 140-160 m above the base, archaeocyath zone III; *Bigotina bivallata, Lemdadella* aff. *linaresae.*	(Liñán et al., 2005)

		Mb I, 180-190 m above the base, archaeocyath zone III; *Eoredlichia* cf. *ovetiensis, Lemdadella perejoni*	
Laurentia, Canada, Mackenzie Mts	Sekwi Fm	basal part, S0, δ^{13}C Cycle A peak (? = Cycle IV); *Parafallotaspis grata*	(Dilliard et al., 2007; Fritz, 1972)
Laurentia, USA, Great Basin	Campito Fm	Gold Coin Mb; *Fritzaspis* sp. – *Profallotaspis?* sp. – *Fritzaspis generalis* – *F. ovalis* – *Amplifallotaspis keni* – *Repinaella* sp.	(Hollingsworth, 2011)
Laurentia, Mexico, Sonora (Cerro Rajón section)	Puerto Blanco Fm	Unit 2, basal part; cf. *Fallotaspis* sp.	(Stewart et al., 1984)
Avalonia, Newfoundland, Avalon Peninsula	Brigus Fm	St. Mary's Mb, middle part /cf. 517.22 ± 0.31(0.40) [0.66] Ma (Williams et al., 2013) by correlation with Purley Sh, England/; *Callavia broeggeri*	(Landing et al., 2017, 2013; Williams et al., 2013)
Avalonia, Cwm Bach, South Wales	Caerfai Bay Fm	Zircon U-Pb age of 519.30 ± 0.23 (0.57) [0.77] Ma (Harvey et al., 2011) for the lowest Caerfai Bay Fm (see table S1), which contains the oldest unidentified trilobite fragments in Avalonia (Landing et al., 2020).	(Harvey et al., 2011; Landing et al., 2020)
Baltica, Sweden, Scåne	Læså Fm	Norretorp Mb, middle part; *Schmidtiellus mickwitzi, Holmia mobergi*	(Nielsen and Schovsbo, 2011)

Table S2.

(separate xlsx data file 'TableS2_AgeModels.xlsx'). Alternative age models for the Ediacaran and lower Cambrian interval ca. 635-517 Ma. Includes new $\delta^{13}C_{carb}$ data from sections of the Nama Group, Namibia, and compiled published data from globally-distributed sections, in addition to biostratigraphic information (Tab1_Global_Data_550-517), published age model of Yang et al. (2021) (Tab2_Yang_635-550), output of lower Cambrian fossil first appearances within each stratigraphic section subdivided by family (Tab3_CambrianFADs), biostratigraphic reference table (Tab4_Biostratigraphy), full (and screened) $^{87}Sr/^{86}Sr$ database (Tab5_8786Sr), output of $\delta^{13}C_{carb}$ and $^{87}Sr/^{86}Sr$ data by region (Tab6_Figured_Correlations), output of block averaged sedimentation rates for interval 635-517 Ma (Tab7_BlockAverageSedRate), and associated references (Tab8_References).

References

Adôrno, R.R., do Carmo, D.A., Germs, G., Walde, D.H.G., Denezine, M., Boggiani, P.C., Sousa e Silva, S.C., Vasconcelos, J.R., Tobias, T.C., Guimarães, E.M., Vieira, L.C., Figueiredo, M.F., Moraes, R., Caminha, S.A., Suarez, P.A.Z., Rodrigues, C. V., Caixeta, G.M., Pinho, D., Schneider, G., Muyambag, R., 2017. *Cloudina lucianoi* (Beurlen and Sommer, 1957), Tamengo Formation, Ediacaran, Brazil: Taxonomy, analysis of stratigraphic distribution and biostratigraphy. Precambrian Res. 301, 19–35.

Adôrno, R.R., Walde, D.H.G., Erdtmann, B.D., Denezine, M., Cortijo, I., Do Carmo, D.A., Giorgioni, M., Ramos, M.E.A.F., Fazio, A., 2019. First occurrence of *Cloudina carinata* Cortijo et al., 2010 in South America, Tamengo Formation, Corumbá Group, upper Ediacaran of Midwestern. Estud. Geológicos 75, e095.

Ahm, A.-S.C., Bjerrum, C.J., Hoffman, P.F., Macdonald, F.A., Maloof, A.C., Rose, C. V., Strauss, J. V., Higgins, J.A., 2021. The Ca and Mg isotope record of the Cryogenian Trezona carbon isotope excursion. Earth Planet. Sci. Lett. 568, 117002.

Ahn, S.Y., Babcock, L.E., Hollingsworth, J.S., 2011. Revised stratigraphic nomenclature for parts of the Ediacaran-Cambrian Series 2 succession in the southern Great Basin, USA. Mem. Assoc. Australas. Palaeontols. 42, 105–114.

Álvaro, J.J., Cortijo, I., Jensen, S., Lorenzo, S., Palacios, T., Pieren, A.P., 2019. Updated stratigraphic framework and biota of the Ediacaran and Terreneuvian in the Alcudia-Toledo Mountains of the Central Iberian Zone, Spain. Estud. Geológicos 75, e093.

Amthor, J.E., Grotzinger, J.P., Schröder, S., Bowring, S.A., Ramezani, J., Martin, M.W., Matter, A., 2003. Extinction of *Cloudina* and *Namacalathus* at the Precambrian-Cambrian boundary in Oman. Geology 31, 431–434.

An, Z., Jiang, G., Tong, J., Tian, L., Ye, Q., Song, Huyue, Song, Haijun, 2015. Stratigraphic position of the Ediacaran Miaohe biota and its constrains on the age of the upper Doushantuo $\delta^{13}C$ anomaly in the Yangtze Gorges area, South China. Precambrian Res. 271, 243–253. https://doi.org/10.1016/j.precamres.2015.10.007

Astashkin, V.A., Pegel, T. V., Repina, L.N., Rozanov, A.Y., Shabanov, Y.Y., Zhuravlev, A.Y., Sukhov, S.S., Sundukov, V.M., 1995. The Cambrian System of the foldbelts of Russia and Mongolia. Correlation chart and explanatory notes. Int. Union Geol. Sci. Publ. 32, 1–132.

Astashkin, V.A., Varlamov, A.I., Grigorieva, N. V., Egorova, L.I., Zhuravlev, A.Y., Zhuravleva, I.T., Missarzhevsky, V. V., Osadchaya, D. V., Repina, L.N., Rozanov, A.Y., Shabanov, Y.Y., 1984. (Early Cambrian Stage Subdivision. Stratigraphy). Nauka, Moscow, 184p.

Babcock, L.E., Peng, S., Zhu, M., Xiao, S., Ahlberg, P., 2014. Proposed reassessment of the Cambrian GSSP. J. African Earth Sci. 98, 3–10.

Bagmet, G.N., 1994. On finds of *Cloudina* in Mountain Shoria, in: Podobina, V.M., Rodygin, S.A. (Eds.), Problems of Geology in Siberia. Tomsk State University, Tomsk, p. 60.

Becker-Kerber, B., Pacheco, M.L.A.F., Rudnitzki, I.D., Galante, D., Rodrigues, F., de Moraes Leme, J., 2017. Ecological interactions in *Cloudina* from the Ediacaran of Brazil: implications for the rise of animal biomineralization. Sci. Rep. 7, 1–11.

Becker-Kerber, B., Paim, P.S.G., Chemale Jr., F., Girelli, T.J., Zucatti da Rosa, A.L., El Albani, A., Osés, G.L., Prado, G.M.E.M., Figueiredo, M., Simões, L.S.A., Pacheco, M.L.A.F., 2020. The oldest record of Ediacaran macrofossils in Gondwana (~563 Ma, Itajaí Basin, Brazil). Precambrian Res. 84, 211–228.

Becker, Y.R., 2010. Geological potential of the ancient ichnofossils in the Late Precambrian stratotype of the South Urals. Reg. Geol. i Metallog. 43, 18–35.

Bengtson, S., Conway Morris, S., Cooper, B.J., Jell, P.A., Runnegar, B.N., 1990. Early Cambrian fossils from South Australia. Mem. Assoc. Australas. Palaeontols. 9, 1–364.

Betts, M.J., Claybourn, T.M., Brock, G.A., Jago, J.B., Skovsted, C.B., Paterson, J.R., 2019. Shelly fossils from the lower Cambrian White Point Conglomerate, Kangaroo Island, South Australia. Acta Palaeontol. Pol. 64, 489–522.

Betts, M.J., Paterson, J., Jago, J., Jacquet, S., Skovsted, C., Topper, T., Brock, G., 2017a. A new lower Cambrian shelly fossil biostratigraphy for South Australia, Reply. Gondwana Res. 44, 262–264.

Betts, M.J., Paterson, J.R., Jacquet, S.M., Andrew, A.S., Hall, P.A., Jago, J.B., Jagodzinski, E.A., Preiss, W. V., Crowley, J.L., Brougham, T., Mathewson, C.P., García-Bellido, D.C., Topper, T.P., Skovsted, C.B., Brock, G.A., 2018. Early Cambrian chronostratigraphy and geochronology of South Australia. Earth-Science Rev. 185, 498–543.

Betts, M.J., Paterson, J.R., Jago, J.B., Jacquet, S.M., Skovsted, C.B., Topper, T.P., Brock, G.A., 2017b. Global correlation for the early Cambrian of South Australia: Shelly fauna of the *Dailyatia odyssei* Zone. Gondwana Res. 46, 240–279.

Betts, M.J., Paterson, J.R., Jago, J.B., Jacquet, S.M., Skovsted, C.B., Topper, T.P., Brock, G.A., 2016. A new lower Cambrian shelly fossil biostratigraphy for South Australia. Gondwana Res. 36, 176–208.

Boag, T.H., Darroch, S.A.F., Laflamme, M., 2016. Ediacaran distributions in space and time: testing assemblage concepts of earliest macroscopic body fossils. Paleobiology 42, 574–594.

Boggiani, P.C., Gaucher, C., Sial, A.N., Babinski, M., Simon, C.M., Riccomini, C., Ferreira, V.P., Faurchild, T.R., 2010. Chemostratigraphy of the Tamengo Formation (Corumbá Group, Brazil): A contribution to the calibration of the Ediacaran carbon-isotope curve. Precambrian Res. 182, 382–401.

Bokova, A.R., 1990. New Lower Cambrian gastropods of the Siberian Platform. Paleontol. Zhurnal 2, 123–126.

Bold, U., Crüger Ahm, A.S., Schrag, D.P., Higgins, J.A., Jamsran, E., Macdonald, F.A., 2020. Effect of dolomitization on isotopic records from Neoproterozoic carbonates in southwestern Mongolia. Precambrian Res. 350, 105902.

Bowring, S.A., Grotzinger, J.P., Condon, D.J., Ramezani, J., Newall, M.J., Allen, P.A., 2007. Geochronologic constraints on the chronostratigraphic framework of the Neoproterozoic Huqf Supergroup, Sultanate of Oman. Am. J. Sci. 307, 1097–1145.

Bowring, S.A., Grotzinger, J.P., Isachsen, C.E., Knoll, A.H., Pelechaty, S.M., Kolosov, P., 1993. Calibrating rates of Early Cambrian evolution. Science. 261, 1293–1298.

Bowyer, F., Wood, R.A., Poulton, S.W., 2017. Controls on the evolution of Ediacaran metazoan ecosystems: A redox perspective. Geobiology 15, 516–551. https://doi.org/10.1111/gbi.12232

Bowyer, F.T., Shore, A.J., Wood, R.A., Alcott, L.J., Thomas, A.L., Butler, I.B., Curtis, A., Hainanan, S., Curtis-Walcott, S., Penny, A.M., Poulton, S.W., 2020. Regional nutrient decrease drove redox stabilisation and metazoan diversification in the late Ediacaran Nama

Group, Namibia. Sci. Rep. 10, 1–11. https://doi.org/10.1038/s41598-020-59335-2

Brand, U., Azmy, K., Tazawa, J.I., Sano, H., Buhl, D., 2010. Hydrothermal diagenesis of Paleozoic seamount carbonate components. Chem. Geol. 278, 173–185.

Brasier, M., Cowie, J., Taylor, M., 1994. Decision on the Precambrian-Cambrian boundary stratotype. Episodes 17, 3–8.

Brasier, M.D., Anderson, M.M., Corfield, R.M., 1992. Oxygen and carbon isotope stratigraphy of early Cambrian carbonates in southeastern Newfoundland and England. Geol. Mag. 129, 265–279.

Brasier, M.D., Magaritz, M., Corfield, R., Luo, H., Wu, X., Ouyang, L., Jiang, Z., Hamdi, B., He, T., Fraser, A.G., 1990. The carbon- and oxygen-isotope record of the Precambrian-Cambrian boundary interval in China and Iran and their correlation. Geol. Mag. 127, 319–332.

Brasier, M.D., Rozanov, A.Y., Zhuravlev, A.Y., Corfield, R.M., Derry, L.A., 1994. A carbon isotope reference scale for the Lower Cambrian Series in Siberia (Report of IGCP Project 303). Geol. Mag. 131, 767–783.

Brasier, M.D., Shields, G., Kuleshov, V.N., Zhegallo, E.A., 1996. Integrated chemo- and biostratigraphic calibration of early animal evolution: Neoproterozoic-early Cambrian of southwest Mongolia. Geol. Mag. 133, 445–485.

Brasier, M.D., Singh, P., 1987. Microfossils and Precambrian-Cambrian boundary stratigraphy at Maldeota, Lesser Himalaya. Geol. Mag. 124, 323–345.

Brass, G.W., 1976. The variation of the marine $^{87}Sr/^{86}Sr$ ratio during Phanerozoic time: interpretation using a flux model. Geochim. Cosmochim. Acta 40, 721–730.

Brock, G.A., Engelbretsen, M.J., Jago, J.B., Kruse, P.D., Laurie, J.R., Shergold, J.H., Shi, G.R., Sorauf, J.E., 2000. Palaeobiogeographic affinities of Australian Cambrian faunas. Mem. Assoc. Australas. Palaeontols. 23, 1–61.

Brooks, B.J., Crowley, J.L., Bowring, S.A., Cervato, C., Jin, Y., 2006. A new U/Pb date for the basal Meishucun section and implications for the age of the Cambrian explosion. Am. Geophys. Union, Fall Meet. Abstr. V21A-0568.

Bykova, N., LoDuca, S.T., Ye, Q., Marusin, V., Grazhdankin, D., Xiao, S., 2020. Seaweeds through time: Morphological and ecological analysis of Proterozoic and early Paleozoic benthic macroalgae. Precambrian Res. 350, 105875.

Cai, Y., Hua, H., Xiao, S., Schiffbauer, J.D., Li, P., 2010. Biostratinomy of the late Ediacaran pyritized Gaojiashan Lagerstätte from southern Shaanxi, South China: Importance of event deposits. Palaios 25, 487–506.

Cai, Y., Sciffbauer, J.D., Hua, H., Xiao, S., 2011. Morphology and paleoecology of the late Ediacaran tubular fossil *Conotubus hemiannulatus* from the Gaojiashan Lagerstätte of southern Shaanxi Province, South China. Precambrian Res. 191, 46–57.

Cai, Y., Xiao, S., Li, G., Hua, H., 2019. Diverse biomineralizing animals in the terminal Ediacaran Period herald the Cambrian explosion. Geology 47, 380–384. https://doi.org/10.1130/G45949.1

Canfield, D.E., Knoll, A.H., Poulton, S.W., Narbonne, G.M., Dunning, G.R., 2020. Carbon isotopes in clastic rocks and the Neoproterozoic carbon cycle. Am. J. Sci. 320, 97–124. https://doi.org/10.2475/02.2020.01

Chen, D., Zhou, X., Fu, Y., Wang, J., Yan, D., 2015. New U-Pb zircon ages of the Ediacaran-Cambrian strata in South China. Terra Nov. 27, 62–68.

Chen, P., 1984. Discovery of Lower Cambrian small shelly fossils from Jijiapo, Yichang, West Hubei and its significance. Prof. Pap. Stratigr. Palaeontol. 13, 49–64.

Chen, Z., Zhou, C., Xiao, S., Wang, W., Guan, C., Hua, H., Yuan, X., 2014. New Ediacaran fossils preserved in marine limestone and their ecological implications. Sci. Rep. 4, 4180.

Chen, Z., Zhou, C., Yuan, X., Xiao, S., 2019. Death march of a segmented and trilobate bilaterian elucidates early animal evolution. Nature 573, 412–415. https://doi.org/10.1038/s41586-019-

1522-7

Compston, W., Zhang, Z., Cooper, J.A., Ma, G., Jenkins, R.J.F., 2008. Further SHRIMP geochronology on the early Cambrian of South China. Am. J. Sci. 308, 299–420.

Condon, D., Zhu, M., Bowring, S., Wang, W., Yang, A., Jin, Y., 2005. U-Pb ages from the neoproterozoic Doushantuo Formation, China. Science. 308, 95–98. https://doi.org/10.1126/science.1107765

Conway Morris, S., Fritz, W.H., 1980. Shelly microfossils near the Precambrian-Cambrian boundary, Mackenzie Mountains, northwestern Canada. Nature 286, 381–384.

Conway Morris, S., Mattes, B.W., Chen, M., 1990. The early skeletal organism *Cloudina*: New occurrences from Oman and possibly China. Am. J. Sci. 290-A, 245–260.

Cope, J.C.W., 1983. Precambrian faunas from the Carmanthen district. Nat. Wales, New Ser. 1, 11–16.

Cordie, D.R., Dornbos, S.Q., Marenco, P.J., Oji, T., Gonchigdorj, S., 2019. Depauperate skeletonized reef-dwelling fauna of the early Cambrian: insights from archaeocyathan reef ecosystems of western Mongolia. Palaeogeogr. Palaeoclimatol. Palaeoecol. 514, 206–221.

Corsetti, F.A., Hagadorn, J.W., 2003. The Precambrian-Cambrian transition in the southern Great Basin, USA. Sediment. Rec. 1, 4–8.

Cortijo, I., Martí Mus, M., Jensen, S., Palacios, T., 2010. A new species of *Cloudina* from the terminal Edicaran of Spain. Precambrian Res. 176, 1–10.

Crimes, T.P., McIlroy, D., 1999. A biota of Ediacaran aspect from lower Cambrian strata on the Digermul Peninsula, Arctic Norway. Geol. Mag. 136, 633–642.

Cui, H., Grazhdankin, D.V., Xiao, S., Peek, S., Rogov, V.I., Bykova, N.V., Sievers, N.E., Liu, X.M., Kaufman, A.J., 2016a. Redox-dependent distribution of early macro-organisms: Evidence from the terminal Ediacaran Khatyspyt Formation in Arctic Siberia. Palaeogeogr. Palaeoclimatol. Palaeoecol. 461, 122–139. https://doi.org/10.1016/j.palaeo.2016.08.015

Cui, H., Kaufman, A.J., Xiao, S., Peek, S., Cao, H., Min, X., Cai, Y., Siegel, Z., Liu, X.M., Peng, Y., Schiffbauer, J.D., Martin, A.J., 2016b. Environmental context for the terminal Ediacaran biomineralization of animals. Geobiology 14, 344–363. https://doi.org/10.1111/gbi.12178

Cui, H., Kaufman, A.J., Zou, H., Kattan, F.H., Trusler, P., Smith, J., Ivantsov, A.Y., Rich, T.H., Al Qubsani, A., Yazedi, A., Lui, X.M., 2020a. Primary or secondary? A dichotomy of the strontium isotope anomalies in the Ediacaran carbonates of Saudi Arabia. Precambrian Res. 105720.

Cui, H., Warren, L. V., Uhlein, G.J., Okubo, J., Liu, X.M., Plummer, R.E., Baele, J., Goderis, S., Claeys, P., Li, F., 2020b. Global or regional? Constraining the origins of the middle Bambuí carbon cycle anomaly in Brazil. Precambrian Res. 348, 105861.

Cui, H., Xiao, S., Cai, Y., Peek, S., Plummer, R.E., Kaufman, A.J., 2019. Sedimentology and chemostratigraphy of the terminal Ediacaran Dengying Formation at the Gaojiashan section, South China. Geol. Mag. 156, 1924–1948.

Daily, B., 1990. Cambrian stratigraphy of Yorke Peninsula. Geol. Soc. Aust. Spec. Publ. 16, 215–229.

Daily, B., 1972. The base of the Cambrian and the first Cambrian faunas, in: Jones, J.B., McGowran, B. (Eds.), Stratigraphic Problems of the Late Precambrian and Early Cambrian. University of Adelaide Centre for Precambrian Research Special Paper 1, pp. 13–42.

Darroch, S.A.F., Boag, T.H., Racicot, R.A., Tweedt, S., Mason, S.J., Erwin, D.H., Laflamme, M., 2016. A mixed Ediacaran-metazoan assemblage from the Zaris Subbasin, Namibia. Palaeogeogr. Palaeoclimatol. Palaeoecol. 459, 198–208.

Darroch, S.A.F., Cribb, A.T., Buatois, L.A., Germs, G.J.B., Kenchington, C.G., Smith, E.F., Mocke, H., O'Neil, G.R., Schiffbauer, J.D., Maloney, K.M., Racicot, R.A., Turk, K.A., Gibson, B.M., Almond, J., Koester, B., Boag, T.H., Tweedt, S.M., Laflamme, M., 2021. The trace fossil record of the Nama Group, Namibia: Exploring the terminal Ediacaran roots of the Cambrian explosion. Earth-Science Rev. 212, 103435.

Darroch, S.A.F., Smith, E.F., Laflamme, M., Erwin, D.H., 2018. Ediacaran Extinction and Cambrian Explosion. Trends Ecol. Evol. 33, 653–663. https://doi.org/10.1016/j.tree.2018.06.003

Darroch, S.A.F., Sperling, E.A., Boag, T.H., Racicot, R.A., Mason, S.J., Morgan, A.S., Tweedt, S., Myrow, P., Johnston, D.T., Erwin, D.H., Laflamme, M., 2015. Biotic replacement and mass extinction of the Ediacara biota. Proc. R. Soc. B Biol. Sci. 282, 20151003.

Debrenne, F., Debrenne, M., 1995. Archaeocyaths of the Lower Cambrian of Morocco. Beringeria Spec. Issue 2, 121–145.

Debrenne, F., Gandin, A., Courjault-Radé, P., 2002. Facies and depositional setting of the Lower Cambrian archaeocyath-bearing limestones of southern Montagne Noire (Massif Central, France). Bull. Soc. géol. Fr. 173, 533–546.

Debrenne, F., Gandin, A., Rowland, S.M., 1989. Lower Cambrian bioconstructions in northwestern Mexico (Sonora). Depositional setting, paleoecology and systematics of archaeocyaths. Géobios 22, 137–195.

Debrenne, F., Zhuravlev, A.Y., Kruse, P.D., 2015. General features of the Archaeocyatha. Systematic descriptions: Archaeocyatha, in: Treatise on Invertebrate Paleontology, Pt. E Porifera Revised (Hypercalcified Porifera). Univ. Kansas Paleontol. Inst., Lawrence, KA, pp. 845–1084.

Devaere, L., Clausen, S., Steiner, M., Álvaro, J.J., Vachard, D., 2013. Chronostratigraphic and palaeogeographic significance of an early Cambrian microfauna from the Heraultia Limestone, Montagne Noire, France. Palaeontol. Electron. 16, 17A – 91.

Dilliard, K.A., Pope, M.C., Coniglio, M., Hasiotis, S.T., Lieberman, B.S., 2007. Stable isotope geochemistry of the lower Cambrian Sekwi Formation, Northwest Territories, Canada: Implications for ocean chemistry and secular curve generation. Palaeogeogr. Palaeoclimatol. Palaeoecol. 256, 174–194. https://doi.org/10.1016/j.palaeo.2007.02.031

Droser, M.L., Gehling, J.G., Tarhan, L.G., Evans, S.D., Hall, C.M.S., Hughes, I. V., Hughes, E.B., Dzaugis, M.E., Dzaugis, M.P., Dzaugis, P.W., Rice, D., 2019. Piecing together the puzzle of the Ediacaran biota: Excavation and reconstruction at the Ediacara National Heritage site Nilpena (South Australia). Palaeogeogr. Palaeoclimatol. Palaeoecol. 513, 132–145.

Duda, J.P., Zhu, M., Reitner, J., 2016. Depositional dynamics of a bituminous carbonate facies in a tectonically induced intra-platform basin: the Shibantan Member (Dengying Formation, Ediacaran Period). Carbonates and Evaporites 31, 87–99. https://doi.org/10.1007/s13146-015-0243-8

Dyatlova, I.N., Sycheva, R.F., 1999. New data on Lower Cambrian biostratigraphy of Eastern Sayan. Stratigr. Geol. Korrelyatsiya 7, 3–13.

Elderfield, H., 1986. Strontium isotope stratigraphy. Palaeogeogr. Palaeoclimatol. Palaeoecol. 57, 71–90.

Elliott, D.A., Trusler, P.W., Narbonne, G.M., Vickers-Rich, P., Morton, N., Hall, M., Hoffmann, K.-H., Schneider, G.I.C., 2016. Ernietta from the late Ediacaran Nama Group, Namibia. J. Paleontol. 90, 1017–1026.

Esakova, N. V., Zhegallo, E.A., 1996. Lower Cambrian biostratigraphy and fauna of Mongolia. Sovmest. Ross.-Mongol. Paleontol. Ekspeditsiya 46, 214.

Fedonkin, M.A., 1990. Palaeoichnology of the Vendian Metazoa, in: Sokolov, B.S., Ivanovskiy, B.A. (Eds.), The Vendian System, Vol. 1: Paleontology. Berlin, Heidelberg: Springer, pp. 112–117.

Fedonkin, M.A., 1976. Trace fossils of metazoans from the Valdai Group. Izv. Akad. Nauk SSSR, Seriya Geol. 4, 129–132.

Fedonkin, M.A., Gehling, J.G., Grey, K., Narbonne, G., Vickers-Rich, P., Clarke, A.C., 2007. The

Rise of Animals: Evolution and Diversification of the Kingdom Animalia. Johns Hopkins University Press, Baltimore.

Føyn, N.S., Glaessner, M.F., 1979. *Platysolenites*, other animal fossils, and the Precambrian-Cambrian transition in Norway. Nork Geol. Tidsskr. 59, 25–46.

Fritz, W.H., 1972. Lower Cambrian trilobites from the Sekwi Formation type section, Mackenzie Mountains, northwestern Canada. Geol. Surv. Canada Bull. 212, 1–90.

Gámez Vintaned, J., Schmitz, U., Liñán, E., 2009. Upper Vendian-lowest Ordovician sequence of the western Gondwana margin, NE Spain, in: Craig, J., Thurow, J., Thusu, B., Whitham, A., Abutarruma, Y. (Eds.), Global Neoproterozoic Petroleum Systems: The Emerging Potential in North Africa. The Geological Society of London Special Publication 326, pp. 229–242.

Gaucher, C., 2000. Sedimentology, palaeontology and stratigraphy of the Arroyo del Sodado Group (Vendian to Cambria, Uruguay). Beringeria 26, 1–120.

Gaucher, C., Boggiani, P.C., Sprechmann, P., Sial, A.N., Fairchild, T., 2003. Integrated correlation of the Vendian to Cambrian Arroyo del Sodado and Corumbá groups (Uruguay and Brazil): palaeogeographic, palaeoclimatic and palaeobiologic implications. Precambrian Res. 120, 241–278.

Gehling, J., Droser, M.L., 2013. How well do fossil assemblages of the Ediacara Biota tell time? Geology 41, 447–450.

Gehling, J.G., Jensen, S., Droser, M.L., Myrow, P.M., Narbonne, G.M., 2001. Burrowing below the basal Cambrian GSSP, Fortune Head, Newfoundland. Geol. Mag. 138, 213–218.

Gehling, J.G., Narbonne, G.M., Anderson, M.M., 2000. The first named Ediacaran body fossil, *Aspidella terranovica*. Palaeontology 43, 427–456.

Germs, G.J., 1972. New shelly fossils from the Nama Group, South-West Africa. Am. J. Sci. 272, 752–761.

Germs, G.J.B., 1983. Implications of a sedimentary facies and depositional environmental analysis of the Nama Group in South West Africa/Namibia. Spec. Publ. Geol. Soc. South Africa 11, 89-114.

Germs, G.J.B., Gresse, P.G., 1991. The foreland basin of the Damara and Gariep orogens in Namaqualand and southern Namibia: stratigraphic correlations and basin dynamics. South African J. Geol. 94(2/3), 159-169.

Geyer, G., Landing, E., 2017. The Precambrian-Phanerozoic and Ediacaran-Cambrian boundaries: a historical approach to a dilemma, in: Brasier, A.T., McIlroy, D., McLoughlin, N. (Eds.), Earth System Evolution and Early Life: A Celebration of the Work of Martin Brasier. The Geological Society of London Special Publication 448, pp. 311–349.

Geyer, G., Uchman, A., 1995. Ichnofossil assemblages from the Nama Group (Neoproterozoic-Lower Cambrian) in Namibia and the Proterozoic-Cambrian boundary problem revisited. Beringeria Spec. Issue 2, 175–202.

Geyman, E.C., Maloof, A.C., 2019. A diurnal carbon cycle engine explains ^{13}C-enriched carbonates without increasing the global production of oxygen. Proc. Natl. Acad. Sci. U. S. A. 116, 24433–24439.

Gibson, B.M., Rahman, I.A., Maloney, K.M., Racicot, R.A., Mocke, H., Laflamme, M., Darroch, S.A.F., 2019. Gregarious suspension feeding in a modular Ediacaran organism. Sci. Adv. 5, eaaw0260.

Gozalo, R., Linán, E., Palacios, T., Gámez Vintaned, J.A., Mayoral, E., 2003. The Cambrian of the Iberian Peninsula: An overview. Geol. Acta 1, 103–112. https://doi.org/10.1344/105.000001596

Gravestock, D.I., 1984. Archaeocyatha from lower parts of the Lower Cambrian carbonate sequence in South Australia. Mem. Assoc. Australas. Palaeontols. 2, 1–139.

Gravestock, D.I., Alexander, E.M., Demidenko, Y.E., Esakova, N. V., Holmer, L.E., Jago, J.B., Lin, T.-R., Melnikova, L.M., Parkhaev, P.Y., Rozanov, A.Y., Ushatinskaya, G.T., Zang, W.-

I., Zhegallo, E.A., Zhuravlev, A.Y., 2001. The Cambrian Biostratigraphy of the Stansbury Basin, South Australia. Moscow: Nauka. 344p.

Grazhdankin, D., 2014. Patterns of evolution of the Ediacaran Soft-Bodied Biota. J. Paleontol. 88, 269–283. https://doi.org/10.1666/13-072

Grazhdankin, D., 2004. Patterns of distribution in the Ediacaran biotas: facies versus biogeography and evolution. Paleobiology 30, 203–221. https://doi.org/10.1666/0094-8373(2004)030<0203:podite>2.0.co;2

Grazhdankin, D. V., Krayushkin, A. V., 2007. Trace fossils and the Upper Vendian boundary in the southeastern White Sea region. Dokl. Earth Sci. 416, 1027–1031.

Grazhdankin, D. V., Marusin, V. V., Izokh, O.P., Karlova, G.A., Kochnev, B.B., Markov, G.E., Nagovitsin, K.E., Sarsembaev, Z., Peek, S., Cui, H., Kaufman, A.J., 2019. Quo vadis, Tommotian? Geol. Mag. 157, 22–34.

Grazhdankin, D. V., Marusin, V. V., Meert, J., Krupenin, M.T., Maslov, A. V., 2011. Kotlin Regional Stage in the South Urals. Dokl. Earth Sci. 440, 1222–1226.

Grazhdankin, D. V., Maslov, A. V., 2015. The room for the Vendian in the International Chronostratigraphic Chart. Russ. Geol. Geophys. 56, 549–559.

Gresse, P.G., Germs, G.J.B., 1993. The Nama foreland basin: sedimentation, major unconformity bounded sequences and multisided active margin advance. Precambrian Res. 63, 247-272. https://doi.org/10.1016/0301-9268(93)90036-2

Grotzinger, J.P., Adams, E.W., Schröder, S., 2005. Microbial-metazoan reefs of the terminal Proterozoic Nama Group (c. 550–543 Ma), Namibia. Geol. Mag. 142, 499–517.

Grotzinger, J.P., Bowring, S.A., Saylor, B.Z., Kaufman, A.J., 1995. Biostratigraphic and geochronological constraints on early animal evolution. Science. 13, 229–272. https://doi.org/10.1126/science.270.5236.598

Grotzinger, J.P., Watters, W.A., Knoll, A.H., 2000. Calcified metazoans in thrombolite-stromatolite reefs of the terminal Proterozoic Nama Group, Namibia. Paleobiology 26, 334–359.

Guo, J., Li, G., Qiang, Y., Song, Z., Zhang, Z., Han, J., Wang, W., 2020. *Watsonella crosbyi* from the lower Cambrian (Terreneuvian, Stage 2) Yanjiahe Formation in Three Gorges Area, South China. Palaeoworld 30, 1–19.

Gürich, G., 1933. Die Kuibis-Fossillien der Nama-Formation von Südwestafrika. Paläontol. Z. 15, 137–154.

Gürich, G., 1930. Die bislang ältesten Spuren von Organismen in Südafrika. C. R., XV Int. Geol. Congr. 1929, Pretoria, Union South Africa 2, 670–680.

Hagadorn, J.W., Fedo, C.M., Waggoner, B.M., 2000. Early Cambrian Ediacaran-type fossils from California. J. Paleontol. 74, 731–740.

Hagadorn, J.W., Waggoner, B.M., 2000. Ediacaran fossils from the southwestern Great Basin, United States. J. Paleontol. 74, 349–359.

Hahn, G., Pflug, H.D., 1985. Polypenartige Organismen aus dem Jung-Präkambrium (Nama-Gruppe) von Namibia. Geol. Palaeontol. 19, 1–13.

Haines, P.W., 2000. Problematic fossils in the late Neoproterozoic Wonoka Formation, South Australia. Precambrian Res. 100, 97–108.

Hall, J.G., Smith, E.F., Tamura, N., Fakra, S.C., Bosak, T., 2020. Preservation of erniettomorph fossils in clay-rich siliciclastic deposits from the Ediacaran Wood Canyon Formation, Nevada. Interface Focus 10, 20200012.

Halverson, G.P., Dudás, F.Ö., Maloof, A.C., Bowring, S.A., 2007. Evolution of the $^{87}Sr/^{86}Sr$ composition of Neoproterozoic seawater. Palaeogeogr. Palaeoclimatol. Palaeoecol. 256, 103–129.

Halverson, G.P., Wade, B.P., Hurtgen, M.T., Barovich, K.M., 2010. Neoproterozoic chemostratigraphy. Precambrian Res. 182, 337–350.

https://doi.org/10.1016/j.precamres.2010.04.007

Hamdi, B., 1995. Precambrian-Cambrian deposits in Iran, in: Hushmandzadeh, A. (Ed.), Treatise on the Geology of Iran, Volume 20. Geological Survey of Iran, Tehran, p. 353.

Harvey, T.H.P., Williams, M., Condon, D.J., Wilby, P.R., Siveter, D.J., Rushton, A.W.A., Leng, M.J., Gabbott, S.E., 2011. A refined chronology for the Cambrian succession of southern Britain. J. Geol. Soc. London. 168, 705–716.

Hay, C.C., Creveling, J.R., Hagen, C.J., Maloof, A.C., Huybers, P., 2019. A library of early Cambrian chemostratigraphic correlations from a reproducible algorithm. Geology 47, 457–460.

He, T., Zhu, M., Mills, B.J.W., Wynn, P.M., Zhuravlev, A.Y., Tostevin, R., Pogge von Strandmann, P.A.E., Yang, A., Poulton, S.W., Shields, G.A., 2019. Possible links between extreme oxygen perturbations and the Cambrian radiation of animals. Nat. Geosci. 12, 468–474. https://doi.org/10.1038/s41561-019-0357-z

Hibbard, J.P., Pollack, J.C., Brennan, M., Samson, S.D., Secor, D., 2009. Significance of new Ediacaran fossils and U-Pb zircon ages from the Albermarle Group, Carolina Terrane of North Carolina. J. Geol. 117, 487–498.

Hodgin, E.B., Nelson, L.L., Wall, C.J., Barrón-Díaz, A.J., Webb, L.C., Schmitz, M.D., Fike, D.A., Hagadorn, J.W., Smith, E.F., 2020. A link between rift-related volcanism and end-Ediacaran extinction? Integrated chemostratigraphy, biostratigraphy, and U-Pb geochronology from Sonora, Mexico. Geology 49, 115–119.

Hoffman, P.F., Lamothe, K.G., 2019. Seawater-buffered diagenesis, destruction of carbon isotope excursions, and the composition of DIC in Neoproterozoic oceans. Proc. Natl. Acad. Sci. U. S. A. 116, 18874–18879.

Hofmann, H.J., Mountjoy, E.W., 2001. *Namacalathus-Cloudina* assemblage in Neoproterozoic Miette Group (Byng Formation), British Columbia: Canada's oldest shelly fossils. Geology 29, 1091–1094. https://doi.org/10.1130/0091-7613(2001)029<1091:NCAINM>2.0.CO;2

Hollingsworth, J.S., 2011. Lithostratigraphy and biostratigraphy of Cambrian Stage 3 in western Nevada and eastern California, in: Hollingsworth, J.S., Sundberg, F.A., Foster, J.R. (Eds.), Cambrian Stratigraphy and Paleontology of Northern Arizona and Southern Nevada. Mus. N. Arizona Bull. 67, pp. 26–42.

Hua, H., Chen, Z., Yuan, X., Zhang, L., Xiao, S., 2005. Skeletogenesis and asexual reproduction in the earliest biomineralizing animal *Cloudina*. Geology 33, 277–280.

Huang, T., Chen, D., Ding, Y., Zhou, X., Zhang, G., 2020. SIMS U-Pb zircon geochronological and carbon isotope chemostratigraphic constraints on the Ediacaran-Cambrian boundary succession in the Three Gorges Area, South China. J. Earth Sci. 31, 69–78.

Hughes, N.C., 2016. The Cambrian palaeontological record of the Indian subcontinent. Earth-Science Rev. 159, 428–461.

Ingle, S., Mueller, P.A., Heatherington, A.L., Kozuch, M., 2003. Isotopic evidence for the magmatic and tectonic histories of the Carolina terrane: implications for stratigraphy and terrane affiliation. Tectonophysics 371, 187–211.

Isachsen, C.E., Bowring, S.A., Landing, E., Samson, S.D., 1994. New constraint on the division of Cambrian time. Geology 22, 496–498. https://doi.org/10.1130/0091-7613(1994)022<0496:NCOTDO>2.3.CO;2

Isakar, M., Peel, J.S., 2007. Lower Cambrian helcionelloid molluscs from Estonia. GFF 129, 255–262.

Ishikawa, T., Ueno, Y., Komiya, T., Sawaki, Y., Han, J., Shu, D., Li, Y., Maruyama, S., Yoshida, N., 2008. Carbon isotope chemostratigraphy of a Precambrian/Cambrian boundary section in the Three Gorge area, South China: Prominent global-scale isotope excursions just before the Cambrian Explosion. Gondwana Res. 14, 193–208. https://doi.org/10.1016/j.gr.2007.10.008

Ivantsov, A., 2011. A unique natural object of global significance—the Zimnie Gory locality of moulds of Vendian multicellular animals. Geol. Ukr. 3–4, 89–98.

Ivantsov, A.Y., 2017. Finds of Ediacaran-type fossils in Vendian deposits of the Yudoma Group, Eastern Siberia. Dokl. Earth Sci. 472, 143–146. https://doi.org/10.1134/S1028334X17020131

Ivantsov, A.Y., Gritsenko, V.M., Paliy, V.M., Velikanov, V.A., Konstantinenko, L.I., Menasova, A.S., Fedonkin, M.A., Zakrevskaya, M.A., Serezhnikova, E.A., 2015. Upper Vendian macrofossils of Eastern Europe. Middle Dniester area and Volhynia. Moscow: PIN RAS.

Jablonski, D., Roy, K., Valentine, J.W., 2006. Out of the Tropics: Evolutionary Dynamics of the Latitudinal Diversity Gradient. Science. 314, 102–106.

Jacquet, S.M., Brougham, T., Skovsted, C.B., Jago, J.B., Laurie, J.R., Betts, M.J., Topper, T.P., Brock, G.A., 2017. *Watsonella crosbyi* from the lower Cambrian (Terreneuvian, Stage 2) Normanville Group in South Australia. Geol. Mag. 154, 1088–1104.

Jago, J.B., Gehling, J.G., Betts, M.J., Brock, G.A., Dalgarno, C.R., García-Bellido, D.C., Haslett, P.G., Jacquet, S.M., Kruse, P.D., Langsford, N.R., Mount, T.J., 2020. The Cambrian System in the Arrowie Basin, Flinders Ranges, South Australia. Aust. J. Earth Sci. 67, 923–948.

Jensen, S., 1997. Trace fossils from the Lower Cambrian Mickwitzia sandstone, south-central Sweden. Foss. Strat. 42, 1–110.

Jensen, S., Högström, A.E.S., Høyberget, M., Meihold, G., McIlroy, D., Ebbestad, J.O.R., Taylor, W.L., Agic, H., Palacios, T., 2018. New occurrences of *Palaeopascichnus* from the Stáhpogieddi Formation, Arctic Norway, and their bearing on the age of the Varanger Ice Age. Can. J. Earth Sci. 55, 1253–1261.

Jensen, S., Saylor, B.Z., Gehling, J.G., Germs, G.J.B., 2000. Complex trace fossils from the terminal Proterozoic of Namibia. Geology 28, 143–146.

Jiang, G., Kaufman, A.J., Christie-Blick, N., Zhang, S., Wu, H., 2007. Carbon isotope variability across the Ediacaran Yangtze platform in South China: Implications for a large surface-to-deep ocean δ^{13}C gradient. Earth Planet. Sci. Lett. 261, 303–320. https://doi.org/10.1016/j.epsl.2007.07.009

Kaufman, A.J., Hayes, J.M., Knoll, A.H., Germs, G.J.B., 1991. Isotopic compositions of carbonates and organic carbon from upper Proterozoic successions in Namibia: stratigraphic variation and the effects of diagenesis and metamorphism. Precambrian Res. 49, 301–327. https://doi.org/10.1016/0301-9268(91)90039-D

Kaufman, A.J., Jacobsen, S.B., Knoll, A.H., 1993. The Vendian record of Sr and C isotopic variations in seawater: Implications for tectonics and paleoclimate. Earth Planet. Sci. Lett. 120, 409–430.

Kaufman, A.J., Knoll, A.H., Semikhatov, M.A., Grotzinger, J.P., Jacobsen, S.B., Adams, W., 1996. Integrated chronostratigraphy of Proterozoic–Cambrian boundary beds in the western Anabar region, northern Siberia. Geol. Mag. 133, 509–533. https://doi.org/10.1017/s0016756800007810

Kaufman, A.J., Peek, S., Martin, A.J., Cui, H., Grazhdankin, D., Rogov, V., Xiao, S., Buchwaldt, R., Bowring, S., 2012. A shorter fuse for the Cambrian Explosion? Geol. Soc. Am. Abstr. with Programs 44, 326.

Keith, M.L., Weber, J.N., 1964. Carbon and oxygen isotopic compositions of selected limestones and fossils. Geochim. Cosmochim. Acta 28, 1787–1816.

Kheraskova, T.N., Samygin, S.G., 1992. Tectonic conditions of the formation of Vendian–Middle Cambrian siliciclastic-carbonate complex in Eastern Sayan. Geotektonika 6, 18–36.

Khomentovskiy, V. V., Karlova, G.A., 1991. New data on a correlation of the Vendian-Cambrian strata in eastern and transitional facies regions of Yakutia, in: Khomentovskiy, V. V. (Ed.), Late Precambrian and Early Palaeozoic of Siberia. Siberian Platform and Its Outskirts. IGiG SO AN SSSR, Novosibirsk, pp. 3–44.

Khomentovskiy, V. V., Valkov, A.K., Karlova, G.A., 1990. New data on the biostratigraphy of transitional Vendian-Cambrian strata in the the middle Aldan River basin, in: Khomentovskiy, V. V. (Ed.), Late Precambrian and Early Palaeozoic of Siberia. Problems of the Regional Stratigraphy. IGiG SO AN SSSR, Novosibirsk, pp. 3–57.

Khomentovsky, V. V., Karlova, G.A., 2002. The boundary between Nemakit-Daldynian and Tommotian stages (Vendian-Cambrian Systems) of Siberia. Stratigr. Geol. Correl. 10, 217–238.

Kimura, H., Matsumoto, R., Kakuwa, Y., Hamdi, B., Zibaseresht, H., 1997. The Vendian-Cambrian $\delta^{13}C$ record, North Iran: evidence for overturning of the ocean before the Cambrian Explosion. Earth Planet. Sci. Lett. 147, E1–E7.

Kirschvink, J.L., Magaritz, M., Ripperdan, R.L., Zhuravlev, A.Y., Rozanov, A.Y., 1991. Precambrian-Cambrian boundary: magnetostratigraphy and carbon isotopes resolve correlation problems between Siberia, Morocco, and China. GSA Today 1, 69–71, 87, 91.

Knoll, A.H., Grotzinger, J.P., Kaufman, A.J., Kolosov, P.N., 1995. Integrated approaches to terminal Proterozoic stratigraphy: An example from the Olenek Uplift, northeastern Siberia. Precambrian Res. 73, 251–270.

Kolesnikov, A. V., Marusin, V. V., Nagovitsin, K.E., Maslov, A. V., Grazhdankin, D. V., 2015. Ediacaran biota in the aftermath of the Kotlinian Crisis: Asha Group of the South Urals. Precambrian Res. 263, 59–78.

Kolesnikov, A. V., Rogov, V.I., Bykova, N. V., Danelian, T., Clausen, S., Maslov, A. V., Grazhdankin, D. V., 2018. The oldest skeletal macroscopic organism *Palaeopascichnus linearis*. Precambrian Res. 316, 24–37.

Kontorovich, A.E., Varlamov, A.I., Grazhdankin, D. V., Karlova, G.A., Klets, A.G., Kontorovich, V.A., Saraev, S. V., Terleev, A.A., Belyaev, S.Y., Varaksina, I. V., Efimov, A.S., Kochnev, B.B., Nagovitsin, K.E., Postnikov, A.A., Filippov, Y.F., 2008. A section of Vendian in the east of West Siberian Plate (based on data from the Borehole Vostok 3). Russ. Geol. Geophys. 49, 932–939.

Korobov, M.N., 1989. Lower Cambrian biostratigraphy and polymeran trilobites of Mongolia. Sovmest. Sov.-Mongol. Geol. Ekspeditsiya, Trans. 48, 1–204.

Korobov, M.N., 1980. Lower Cambrian biostratigraphy and miomeran trilobites of Mongolia, in: Menner, V. V., Meyen, S. V. (Eds.), Lower Cambrian and Carboniferous Biostratigraphy of Mongolia. Sovmest. Sov.-Mongol. Geol. Ekspeditsiya, Trans. 26, pp. 5–108.

Kouchinsky, A., Bengtson, S., Landing, E., Steiner, M., Vendrasco, M., Ziegler, K., 2017. Terreneuvian stratigraphy and faunas from the Anabar Uplift, Siberia. Acta Palaeontol. Pol. 62. https://doi.org/10.4202/app.00289.2016

Kouchinsky, A., Bengtson, S., Pavlov, V., Runnegar, B., Torssander, P., Young, E., Ziegler, K., 2007. Carbon isotope stratigraphy of the Precambrian-Cambrian Sukharikha River section, northwestern Siberian platform. Geol. Mag. 114, 1–10. https://doi.org/10.1017/S0016756807003354

Kouchinsky, A., Bengtson, S., Pavlov, V., Runnegar, B., Val'kov, A., Young, E., 2005. Pre-Tommotian age of the lower Pestrotsvet Formation in the Selinde section on the Siberian platform: carbon isotopic evidence. Geol. Mag. 142, 319–325.

Kruse, P.D., Zhuravlev, A.Y., Parkhaev, P.Y., Zhu, M., 2017. A new lower Cambrian shelly fossil biostratigraphy for South Australia, Comment. Gondwana Res. 44, 258–261.

Landing, E., 1994. Precambrian–Cambrian global stratotype ratified and a new perspective of Cambrian time. Geology 22, 179–182.

Landing, E., 1991. Upper Precambrian through Lower Cambrian of Cape Breton Island: faunas, paleoenvironments, and stratigraphic revision. J. Paleontol. 65, 570–595.

Landing, E., 1989. Paleoecology and distribution of the Early Cambrian rostroconch *Watsonella crosbyi* Grabau. J. Paleontol. 63, 566–573.

Landing, E., 1988. Lower Cambrian of eastern Massachusetts: Stratigraphy and small shelly fossils. J. Paleontol. 62, 661–695.

Landing, E., Bowring, S.A., Davidek, K.L., Westrop, S.R., Geyer, G., Heldmaier, W., 1998. Duration of the Early Cambrian: U-Pb ages of volcanic ashes from Avalon and Gondwana. Can. J. Earth Sci. 35, 329–338. https://doi.org/10.1139/cjes-35-4-329

Landing, E., Geyer, G., Brasier, M.D., Bowring, S.A., 2013. Cambrian Evolutionary Radiation: context, correlation, and chronostratigraphy—overcoming deficiencies of the first appearance datum (FAD) concept. Earth-Science Rev. 123, 133–172.

Landing, E., Kouchinsky, A., 2016. Correlation of the Cambrian Evolutionary Radiation: geochronology, evolutionary stasis of earliest Cambrian (Terreneuvian) small shelly fossil (SSF) taxa, and chronostratigraphic significance. Geol. Mag. 153, 750–756.

Landing, E., Kruse, P.D., 2017. Integrated stratigraphic, geochemical, and paleontological late Ediacaran to early Cambrian records from southwestern Mongolia: Comment. Geol. Soc. Am. Bull. 129, 7–8.

Landing, E., Myrow, P., Benus, A.P., Narbonne, G.M., 1989. The Placentian Series: Appearance of the oldest skeletal faunas in southeastern Newfoundland. J. Paleontol. 63, 739–769.

Landing, E., Myrow, P.M., Narbonne, G.M., Geyer, G., Buatois, L.A., Mángano, G., Kaufman, A., Westrop, S.R., Kröger, B., Laing, B., Gougeon, R., 2017. Ediacaran-Cambrian of Avalonian eastern Newfoundland (Avalon, Burin, and Bonavista peninsulas): International Symposium on the Ediacaran-Cambrian transition, Field trip 4. Int. Subcomm. Ediacaran Stratigr. Int. Subcomm. Cambr. Stratigr. St. John's, Newfoundland, June 15–29, 2017. Mem. Univ. Geol. Surv. Newfoundl. Labrador Open File NFL 1–169.

Landing, E., Narbonne, G.M., Myrow, P., Benus, A.P., Anderson, M.M., 1988. Faunas and depositional environments of the Upper Precambrian through Lower Cambrian, southeastern Newfoundland, in: Landing, E., Narbonne, G.M., Myrow, P. (Eds.), Trace Fossils, Small Shelly Fossils and the Precambrian-Cambrian Boundary. Proceedings, August 8–18, 1987, Memorial University. New York State Museum, Bulletin 463, pp. 18–52.

Landing, E., Schmitz, M.D., Geyer, G., Trayler, R.B., Bowring, S.A., 2020. Precise early Cambrian U-Pb zircon dates bracket the oldest trilobites and archaeocyaths in Moroccan West Gondwana. Geol. Mag. 158, 219–238.

Laurie, J.R., 1986. Phosphatic fauna of the Early Cambrian Todd River Dolomite, Amadeus Basin, central Australia. Alcheringa 10, 431–454.

Li, D., Ling, H.F., Shields-Zhou, G.A., Chen, X., Cremonese, L., Och, L., Thirlwall, M., Manning, C.J., 2013. Carbon and strontium isotope evolution of seawater across the Ediacaran-Cambrian transition: Evidence from the Xiaotan section, NE Yunnan, South China. Precambrian Res. 225, 128–147. https://doi.org/10.1016/j.precamres.2012.01.002

Li, G.X., Zhao, X., Gubanov, A., Zhu, M.Y., Na, L., 2011. Early Cambrian mollusc *Watsonella crosbyi*: a potential GSSP index fossil for the base of Cambrian Stage 2. Acta Geol. Sin. 85, 309–319.

Liñán, E., Dies, M.E., Gámez Vintaned, J., Gozalo, R., Mayoral, E., Muñiz, F., 2005. Lower Ovetian (Lower Cambrian) trilobites and biostratigraphy of the Pedroche Formation (Sierra de Córdoba, southern Spain). Geobios 38, 365–381.

Liñán, E., Gámez Vintaned, J., Gozalo, R., 2015. The middle lower Cambrian (Ovetian) *Lunagraulos* n. gen. from Spain and the oldest trilobite records. Geol. Mag. 152, 1123–1136.

Linnemann, U., Ovtcharova, M., Schaltegger, U., Gärtner, A., Hautmann, M., Geyer, G., Vickers-Rich, P., Rich, T., Plessen, B., Hofmann, M., Zieger, J., Krause, R., Kriesfeld, L., Smith, J., 2019. New high-resolution age data from the Ediacran-Cambrian boundary indicate rapid, ecologically driven onset of the Cambrian explosion. Terra Nov. 31, 49–58. https://doi.org/10.1111/ter.12368

Liu, A.G., Tindal, B.H., 2021. Ediacaran macrofossils prior to the ~580 Ma Gaskiers glaciation in Newfoundland, Canada. Lethaia 54, 260–270.

Liu, P., Yin, C., Gao, L., Tang, F., Chen, S., 2009. New material of microfossils from the Ediacaran Doushantuo Formation in the Zhangcunping area, Yichang, Hubei Province and its zircon SHRIMP U-Pb age. Chinese Sci. Bull. 54, 1058–1064. https://doi.org/10.1007/s11434-008-0589-6

Lu, M., Zhu, M., Zhang, J., Shields-Zhou, G., Li, G., Zhao, F., Zhao, X., Zhao, M., 2013. The DOUNCE event at the top of the Ediacaran Doushantuo Formation, South China: Broad stratigraphic occurrence and non-diagenetic origin. Precambrian Res. 225, 86–109. https://doi.org/10.1016/j.precamres.2011.10.018

Luo, C., Miao, L., 2020. A *Horodyskia-Nenoxites*-dominated fossil assemblage from the Ediacaran-Cambrian transition (Liuchapo Formation, Hubei Province): Its paleontological implications and stratigraphic potential. Palaeogeogr. Palaeoclimatol. Palaeoecol. 545, 109635.

Macdonald, F.A., Pruss, S.B., Strauss, J. V., 2014. Trace fossils with spreiten from the late Ediacaran Nama Group, Namibia: complex feeding patterns five million years before the Precambrian – Cambrian boundary. J. Paleontol. 88, 299–308.

Macdonald, F.A., Strauss, J. V., Sperling, E.A., Halverson, G.P., Narbonne, G.M., Johnston, D.T., Kunmann, M., Schrag, D.P., Higgins, J.A., 2013. The stratigraphic relationship between the Shuram carbon isotope excursion, the oxygenation of Neoproterozoic oceans, and the first appearance of the Ediacara biota and bilaterian trace fossils in northwestern Canada. Chem. Geol. 362, 250–272.

Magaritz, M., Kirschvink, J.L., Latham, A.J., Zhuravlev, A.Y., Rozanov, A.Y., 1991. Precambrian-Cambrian boundary problem: carbon isotope correlations for Vendian and Tommotian time between Siberia and Morocco. Geology 19, 847–850.

Maloney, K.M., Boag, T.H., Facciol, A.J., Gibson, B.M., Cribb, A., Koester, B.E., Kenchington, C.G., Racicot, R.A., Darroch, S.A.F., Laflamme, M., 2020. Palaeoenvironmental analysis of *Ernietta*-bearing Ediacaran deposits in southern Namibia. Palaeogeogr. Palaeoclimatol. Palaeoecol. 556, 109884.

Maloof, A.C., Porter, S.M., Moore, J.L., Dudás, F.Ö., Bowring, S.A., Higgins, J.A., Fike, D.A., Eddy, M.P., 2010a. The earliest Cambrian record of animals and ocean geochemical change. Geol. Soc. Am. Bull. 122, 1731–1774. https://doi.org/10.1130/B30346.1

Maloof, A.C., Ramezani, J., Bowring, S.A., Fike, D.A., Porter, S.M., Mazouad, M., 2010b. Constraints on early Cambrian carbon cycling from the duration of the Nemakit-Daldynian–Tommotian boundary $\delta^{13}C$ shift, Morocco. Geology 38, 623–626.

Maloof, A.C., Schrag, D.P., Crowley, J.L., Bowring, S.A., 2005. An expanded record of Early Cambrian carbon cycling from the Anti-Atlas Margin, Morocco. Can. J. Earth Sci. 42, 2195–2216. https://doi.org/10.1139/e05-062

Mansy, J.L., Debrenne, F., Zhuravlev, A.Y., 1993. Calcaires a archéocyathes du Cambrien inférieur du Nord de la Colombie britannique (Canada). Implications paléogéographiques et précisions sur l'extension du continent Américano-Koryakien. Geobios 26, 643–683.

Martin, M.W., Grazhdankin, D. V., Bowring, S.A., Evans, D.A.D., Fedonkin, M.A., Kirschvink, J.L., 2000. Age of Neoproterozoic bilaterian body and trace fossils, White Sea, Russia: Implications for Metazoan evolution. Science. 288, 841–845.

Marusin, V., Karlova, G., Kaufman, A.J., Grazhdankin, D. V., 2015. The Fortunian and Cambrian Stage 2 as seen from arctic Siberia. Ber. Inst. Erdwissenschaften K.-F.-Univ. Graz 21, 241.

Marusin, V. V., Kolesnikova, A.A., Kochnev, B.B., Kuznetsov, N.B., Pokrovsky, B.G., Romanyuk, T. V., Karlova, G.A., Rud'ko, S. V., Shatsillo, A. V., Dubenskiy, A.S., Sheshukov, V.S., Lyapunov, S.M., 2020. Detrital zircon age and biostratigraphic and chemostratigraphic constraints on the Ediacaran-Cambrian transitional interval in the Irkutsk Cis-Sayans Uplift, southwestern Siberian Platform. Geol. Mag. 158, 1156–1172.

Matthews, J.J., Liu, A.G., Yang, C., McIlroy, D., Levell, B., Condon, D.J., 2020. A chronostratigraphic framework for the rise of the Ediacaran microbiota: New constraints from Mistaiken Point Ecological Reserve, Newfoundland. Geol. Soc. Am. Bull. 133, 612–624.

McIlroy, D., Brasier, M.D., 2017. Ichnological evidence for the Cambrian explosion in the Ediacaran to Cambrian succession of Tanafjord, Finmark, northern Norway, in: Brasier, A.T., McIlroy, D., McLoughlin, N. (Eds.), Earth System Evolution and Early Life: A Celebration of the Work of Martin Brasier. The Geological Society of London Special Publications 448, pp. 351–368.

McMenamin, M.A.S., 1985. Basal Cambrian small shelly fossils from the La Ciénega Formation, northwestern Sonora, Mexico. J. Paleontol. 59, 1414–1425.

Melim, L.A., Westphal, H., Swart, P.K., Eberli, G.P., Munnecke, A., 2002. Questioning carbonate diagenetic paradigms: Evidence from the Neogene of the Bahamas. Mar. Geol. 185, 27–53.

Merdith, A.S., Williams, S.E., Collins, A.S., Tetley, M.G., Mulder, J.A., Blades, M.L., Young, A., Armistead, S., Cannon, J., Zahirovic, S., Müller, R.D., 2021. Extending full-plate tectonic models into deep time: Linking the Neoproterozoic and Phanerozoic. Earth-Science Rev. 214, 103477.

Missarzhevsky, V. V., 1989. The oldest skeletal fossils and stratigraphy of Precambrian–Cambrian boundary beds. Geol. Inst. Akad. Nauk SSSR, Trans. 443, 1–237.

Missarzhevsky, V. V., 1973. Conodont-like organisms from Precambrian–Cambrian boundary beds of the Siberian Platform and Kazakhstan. Inst. Geol. Geofiz. Sib. Otd. Akad. Nauk SSSR, Trans. 49, 53–59.

Muscente, A.D., Bykova, N., Boag, T.H., Buatois, L.A., Mángano, M.G., Eleish, A., Prabhu, A., Pan, F., Meyer, M.B., Schiffbauer, J.D., Fox, P., Hazen, R.M., Knoll, A.H., 2019. Ediacaran biozones identified with network analysis provide evidence for pulsed extinctions of early complex life. Nat. Commun. 10, 1–15. https://doi.org/10.1038/s41467-019-08837-3

Nagovitsin, K.E., Rogov, V.I., Marusin, V. V., Karlova, G.A., Kolesnikov, A. V., Bykova, N. V., Grazhdankin, D. V., 2015. Revised Neoproterozoic and Terreneuvian stratigraphy of the Lena-Anabar Basin and north-western slope of the Olenek Uplift, Siberian Platform. Precambrian Res. 270, 226–245.

Narbonne, G.M., Aitken, J.D., 1995. Neoproterozoic of the Mackenzie Mountains, northwestern Canada. Precambrian Res. 73, 101–121.

Narbonne, G.M., Aitken, J.D., 1990. Ediacaran fossils from the Sekwi Brook Area, Mackenzie Mountains, northwestern Canada. Palaeontology 33, 945–980.

Narbonne, G.M., Kaufman, A.J., Knoll, A.H., 1994. Integrated chemostratigraphy and biostratigraphy of the Windermere Supergroup, northwestern Canada: Implications for Neoproterozoic correlations and the early evolution of animals. Geol. Soc. Am. Bull. 106, 1281–1292.

Narbonne, G.M., Saylor, B.Z., Grotzinger, J.P., 1997. The youngest Ediacaran fossils from Southern Africa. J. Paleontol. 71, 953–967. https://doi.org/10.1017/S0022336000035940

Nielsen, A.T., Schovsbo, N.H., 2011. The Lower Cambrian of Scandinavia: Depositional environment, sequence stratigraphy and palaeogeography. Earth-Science Rev. 107, 207–310.

Noble, S.R., Condon, D.J., Carney, J.N., Wilby, P.R., Pharaoh, T.C., Ford, T.D., 2015. U-Pb geochronology and global context of the Charnian Supergroup, UK: Constraints on the age of key Ediacaran fossil assemblages. Geol. Soc. Am. Bull. 127, 250–265.

Novozhilova, N. V., Korovnikov, I. V., 2019. Small shelly fossils in the Cambrian basement of the West Siberian Geosyneclise. Stratigr. Geol. Correl. 27, 1–8.

Nowlan, G.S., Narbonne, G.M., Fritz, W.H., 1985. Small shelly fossils and trace fossils near the Precambrian-Cambrian boundary in the Yukon Territory, Canada. Lethaia 18, 233–256.

Öpik, A., 1926. Über den estländischen Blauen Ton. Publ. Geol. Inst. Univ. Tartu 6, 39–46.

Osadchaya, D. V., Kotel'nikov, D. V., 1998. Archaeocyathids from the Atdabanian (Lower

Cambrian) of the Altay-Sayan Foldbelt, Russia. Geodiversitas 20, 5–18.

Pacześna, J., 1986. Upper Vendian and Lower Cambrian ichnocoenoses of Lublin Region. Biul. Inst. Geol. 355, 31–47.

Palij, V.M., 1976. Remains of non-skeletal fauna and trace fossils from the Upper Precambrian and Lower Cambrian strata of Podolia, in: Schulga, P.L. (Ed.), Palaeontology and Stratigraphy of the Upper Precambrian and Lower Palaeozoic on the South-West of the East European Platform. Kiev: Naukova Dumka, pp. 63–76.

Parkhaev, P.Y., 2019a. Cambrian mollusks of Australia: Taxonomy, biostratigraphy, and Paleobiogeography. Stratigr. Geol. Correl. 27, 181–206.

Parkhaev, P.Y., 2019b. A finding of mollusks *Watsonella crosbyi* Grabau (Gastropoda: Helcionelliformes) in the Botomian of China. Dokl. Earth Sci. 488, 1161–1165.

Parkhaev, P.Y., 2014. On the stratigraphy of *Aldanella attleborensis*—potential index-species for defining the base of Cambrian Stage 2, in: Zhan, R., Huang, B. (Eds.), IGCP Project 591 Field Workshop 2014. Nanjing University Press, Nanjing, pp. 102–105.

Parkhaev, P.Y., Karlova, G.A., 2011. Taxonomic revision and evolution of Cambrian molluscs of the genus *Aldanella* Vostokova, 1962 (Gastropoda: Archaeobranchia). Paleontol. J. 45, 1145–1205.

Parry, L.A., Boggiani, P.C., Condon, D.J., Garwood, R.J., Leme, J. de M., McIlroy, D., Brasier, M.D., Trindade, R., Capanha, G.A.C., Pacheco, M.L.A.F., Diniz, C.Q.C., Liu, A., 2017. Ichnological evidence for meiofaunal bilaterians from the terminal Ediacaran and earliest Cambrian of Brazil. Nat. Ecol. Evol. 1, 1455–1464.

Paterson, J.R., Edgecombe, G.D., Lee, M.S., 2019. Trilobite evolutionary rates constrain the duration of the Cambrian explosion. Proc. Natl. Acad. Sci. U. S. A. 116, 4394–4399.

Pecoits, E., Aubet, N.R., Heaman, L.M., Philippot, P., Rosière, C.A., Veroslavsky, G., Konhauser, K.O., 2016. U – Pb detrital zircon ages from some Neoproterozoic successions of Uruguay: Provenance, stratigraphy and tectonic evolution. J. South Am. Earth Sci. 71, 108–130.

Pelechaty, S.M., 1998. Integrated chronostratigraphy of the Vendian System of Siberia: implications for a global stratigraphy. Geol. Soc. London 155, 957–973.

Pelechaty, S.M., Grotzinger, J.P., Kashirtsev, V.A., Zhernovsky, V.P., 1996a. Chemostratigraphic and sequence stratigraphic constraints on Vendian-Cambrian basin dynamics, Northeast Siberian Craton. J. Geol. 104, 543–563.

Pelechaty, S.M., Kaufman, A.J., Grotzinger, J.P., 1996b. Evaluation of δ13C chemostratigraphy for intrabasinal correlation: Vendian strata of northeast Siberia. Bull. Geol. Soc. Am. 108, 992–1003. https://doi.org/10.1130/0016-7606(1996)108<0992:EOCCFI>2.3.CO;2

Penny, A.M., Wood, R.A., Zhuravlev, A.Y., Curtis, A., Bowyer, F., Tostevin, R., 2017. Intraspecific variation in an Ediacaran skeletal metazoan: *Namacalathus* from the Nama Group, Namibia. Geobiology 15, 81–93.

Perejón, A., 1994. Palaeogeographic and biostratigraphic distribution of Archaeocyatha in Spain. Cour. Forsch.-Inst. Senckenberg 172, 341–354.

Perejón, A., Menéndez, S., Rábano, I., Moreno-Eiris, E., 2014. Nuevos datos documentales sobre la colección de arqueociatos del Cerro de las Ermitas de Córdoba del Museo Geominero (Instituto Geológico y Minero de España). Bol. Geol. Min. 125, 53–63.

Perejón, A., Moreno-Eiris, E., 2006. Biostratigraphy and paleobiogeography of the archaeocyaths on the south-western margin of Gondwana. Z. Dtsch. Geol. Gess. 157, 611–627.

Pflug, H.D., 1966. Neue Fossilreste aus den Nama-Schichten in Südwest-Afrika. Paläontol. Z. 40, 14–25.

Pickford, M.H.L., 1995. Review of the Riphean, Vendian and early Cambrian palaeontology of the Otavi and Nama groups, Namibia. Commun. - Geol. Surv. Namibia 10, 57–81.

Porter, S.M., 2007. Seawater chemistry and early carbonate biomineralization. Science. 316, 1302.

Prave, A.R., Condon, D.J., Hoffmann, K.H., Tapster, S., Fallick, A.E., 2016. Duration and nature of the end-Cryogenian (Marinoan) glaciation. Geology 44, 631–634. https://doi.org/10.1130/G38089.1

Prave, A.R., Kirsimäe, K., Lepland, A., Fallick, A.E., Kreitsmann, T., Deines, Y.E., Romashkin, A.E., Rychanchik, D.V., Medvedev, P.V., Moussavou, M., Bakakas, K., 2021. The grandest of them all: the Lomagundi-Jatuli Event and Earth's oxygenation. J. Geol. Soc. London.

Pu, J.P., Bowring, S.A., Ramezani, J., Myrow, P., Raub, T.D., Landing, E., Mills, A., Hodgin, E., Macdonald, F.A., 2016. Dodging snowballs: Geochronology of the Gaskiers glaciation and the first appearance of the Ediacaran biota. Geology 44, 955–958.

Pyle, L.J., Narbonne, G.M., Nowlan, G.S., Xiao, S., James, N.P., 2006. Early Cambrian metazoan eggs, embryos, and phosphatic microfossils from northwestern Canada. J. Paleontol. 80, 811–825.

Repina, L.N., Borodaevskaya, Z. V., Ermak, V. V., 1988. Key section of the Selinde River (south-eastern margin of the Aldan Shield. Inst. Geol. i Geofoziki, Sib. Otd. Akad. Nauk SSSR, Trans. 720, 3–31.

Riding, R., Zhuravlev, A.Y., 1995. Structure and diversity of oldest sponge-microbe reefs: Lower Cambrian, Aldan River, Siberia. Geology 23, 649–652.

Rogov, V., Marusin, V., Bykova, N., Goy, Y., Nagovitsin, K., 2012. The oldest evidence of bioturbation on Earth. Geology 40, 395–398.

Rogov, V.I., Karlova, G.A., Marusin, V. V., Kochnev, B.B., Nagovitsin, K.E., Grazhdankin, D. V., 2015. Duration of the first biozone in the Siberian hypostratotype of the Vendian. Russ. Geol. Geophys. 56, 573–583.

Rooney, A.D., Cantine, M.D., Bergmann, K.D., Gómez-Pérez, I., Al Baloushi, B., Boag, T.H., Busch, J.F., Sperling, E.A., Strauss, J. V., 2020. Calibrating the coevolution of Ediacaran life and environment. Proc. Natl. Acad. Sci. U. S. A. 117, 16824–16830.

Rowland, S.M., Luchinina, V.A., Korovnikov, I. V., Sipin, D.P., Tarletskov, A.I., Fedoseev, A. V., 1998. Biostratigraphy of the Vendian-Cambrian Sukharikha River section, northwestern Siberian Platform. Can. J. Earth Sci. 35, 339–352.

Sarsembaev, Z.A., Marusin, V. V., 2019. Big guns of the Cambrian Explosion: macroskeletal benthic assemblage in the lower Cambrian Stage 2 of the Olenek Uplift, Arctic Siberia. Estud. Geol. 75, e113.

Saylor, B.Z., 2003. Sequence stratigraphy and carbonate-siliciclastic mixing in a terminal Proterozoic foreland basin, Urusis Formation, Nama Group, Namibia. J. Sediment. Res. 73, 264–279. https://doi.org/10.1306/082602730264

Saylor, B.Z., 1996. Sequence stratigtraphic and chemostratigraphic constraints on the evolution of the terminal Proterozoic to Cambrian Nama Basin, Namibia. Massachusetts Institute of Technology.

Saylor, B. Z., Grotzinger, J.P., 1996. Reconstruction of important Proterozoic-Cambrian boundary exposures through the recognition of thrust deformation in the Nama Group of southern Namibia. Commun. - Geol. Surv. Namibia 11, 1–12.

Saylor, B.Z., Grotzinger, J.P., Germs, G.J.B., 1995. Sequence stratigraphy and sedimentology of the Neoproterozoic Kuibis and Schwarzrand Subgroups (Nama Group), southwestern Namibia. Precambrian Res. 73, 153–171. https://doi.org/10.1016/0301-9268(94)00076-4

Saylor, B.Z., Kaufman, A.J., Grotzinger, J.P., Urban, F., 1998. A composite reference section for terminal Proterozoic strata of southern Namibia. J. Sediment. Res. 68, 1223–1235. https://doi.org/10.2110/jsr.68.1223

Schmitz, M.D., 2012. Radiogenic Isotope Geochronology, in: Gradstein, F.M., Ogg, J.G., Schmitz, M.D., Ogg, G.M. (Eds.), The Geological Time Scale 2012. Elsevier, pp. 115–126.

Selly, T., Schiffbauer, J.D., Jacquet, S.M., Smith, E.F., Nelson, L.L., Andreasen, B.D., Huntley, J.W., Strange, M.A., O'Neil, G.R., Thater, C.A., Bykova, N., Steiner, M., Yang, B., Cai, Y., 2020. A new cloudininid fossil assemblage from the terminal Ediacaran of Nevada, USA. J. Syst. Palaeontol. 18, 357–379.

Semikhatov, M.A., Komar, V.A., Serebryakov, S.N., 1970. The Yudoma Complex in the stratotype area. Geol. Inst. Akad. Nauk SSSR, Trans. 210, 1–207.

Shahkarami, S., Mángano, M.G., Buatois, L.A., 2017. Discriminating ecological and evolutionary controls during the Ediacaran-Cambrian transition: Trace fossils from the Soltanieh Formation of northern Iran. Palaeogeogr. Palaeoclimatol. Palaeoecol. 476, 15–27.

Shen, B., Xiao, S., Dong, L., Zhou, C., Liu, J., 2007. Problematic macrofossils from Ediacaran successions in the North China and Chaidam Blocks: Implications for their evolutionary roots and biostratigraphic significance. J. Paleontol. 81, 1396–1411.

Signor, P.W., Mount, J.F., Onken, B.R., 1987. A pre-trilobite small shelly fauna from the White-Inyo region of eastern California and western Nevada. J. Paleontol. 61, 425–438.

Simón, J., 2018. A transitional Ediacaran-Cambrian biota in the Abenóhar anticline (Iberian Massif, Spain). Estud. Geol. 74, e084.

Slater, B.J., Harvey, T.H.P., Butterfield, N.J., 2018. Small carbonaceous fossils (SCFs) from the Terreneuvian (lower Cambrian of Baltica). Palaeontology 61, 417–439.

Smith, E.F., Macdonald, F.A., Petach, T.A., Bold, U., Schrag, D.P., 2015. Integrated stratigraphic, geochemical, and paleontological late Ediacaran to early Cambrian records from southwestern Mongolia. Geol. Soc. Am. Bull. 128, 442–468. https://doi.org/10.1130/B31248.1

Smith, E.F., Nelson, L.L., Strange, M.A., Eyster, A.E., Rowland, S.M., Schrag, D.P., Macdonald, F.A., 2016. The end of the Ediacaran: Two new exceptionally preserved body fossil assemblages from Mount Dunfee, Nevada, USA. Geology 44, 911–914. https://doi.org/10.1130/G38157.1

Smith, E.F., Nelson, L.L., Tweedt, S.M., Zeng, H., Workman, J.B., 2017. A cosmopolitan late Ediacaran biotic assemblage: new fossils from Nevada and Namibia support a global biostratigraphic link. Proc. R. Soc. B Biol. Sci. 284, 20170934.

Smith, O., 1998. Terminal Proterozoic Carbonate Platform Development: Stratigraphy and Sedimentology of the Kuibis Subgroup (ca. 550 – 548 Ma), Northern Nama Basin, Namibia. Massachusetts Institute of Technology.

Sokolov, B.S., 1967. The oldest Pogonophora. Dokl. Akad. Nauk SSSR 177, 201–204.

Soldatenko, Y., El Albani, A., Ruzina, M., Fontaine, C., Nesterovsky, V., Paquette, J.L., Meunier, A., Ovtcharova, M., 2019. Precise U-Pb age constrains on the Ediacaran biota in Podolia, East European Platform, Ukraine. Sci. Rep. 9, 1–13. https://doi.org/10.1038/s41598-018-38448-9

Sour-Tovar, F., Hagadorn, J.W., Huitrón-Rubio, T., 2007. Ediacaran and Cambrian index fossils from Sonora, Mexico. Palaeontology 50, 169–175.

Sperling, E.A., Carbone, C., Strauss, J. V., Johnston, D.T., Narbonne, G.M., Macdonald, F.A., 2016. Oxygen, facies, and secular controls on the appearance of Cryogenian and Ediacaran body and trace fossils in the Mackenzie Mountains of northwestern Canada. Geol. Soc. Am. Bull. 128, 558–575.

Steiner, M., Li, G., Qian, Y., Zhu, M., Erdtmann, B.D., 2007. Neoproterozoic to early Cambrian small shelly fossil assemblages and a revised biostratigraphic correlation of the Yangtze Platform (China). Palaeogeogr. Palaeoclimatol. Palaeoecol. 254, 67–99.

Steiner, M., Li, G., Qian, Y., Zhu, M., Erdtmann, B.D., 2003. Lower Cambrian small shelly fossil faunas from Zhejiang (China) and their biostratigraphical implications. Prog. Nat. Sci. 13, 852–860.

Steiner, M., Yang, B., Hohl, S., Zhang, L., Chang, S., 2020. Cambrian small skeletal fossil and carbon isotope records of the southern Huangling Anticline, Hubei (China) and implications for chemostratigraphy of the Yangtze Platform. Palaeogeogr. Palaeoclimatol. Palaeoecol. 554, 109817.

Stewart, J.H., McMenamin, M.A.S., Morales-Ramirez, J.M., 1984. Upper Proterozoic and Cambrian rocks in the Caborca region, Sonora, Mexico. United States Geol. Surv. Prof. Pap. 1309, 1–36.

Tahata, M., Ueno, Y., Ishikawa, T., Sawaki, Y., Murakami, K., Han, J., Shu, D., Li, Y., Guo, J., Yoshida, N., Komiya, T., 2013. Carbon and oxygen isotope chemostratigraphies of the Yangtze platform, South China: Decoding temperature and environmental changes through the Ediacaran. Gondwana Res. 23, 333–353. https://doi.org/10.1016/j.gr.2012.04.005

Tarhan, L.G., Hughes, N.C., Myrow, P.M., Bhargava, O.N., Ahluwalia, A.D., Kudryavtsev, A.B., 2014. Precambrian–Cambrian boundary interval occurrence and form of the enigmatic tubular body fossil *Shaanxilithes ningqiangensis* from the Lesser Himalaya of India. Palaeontology 57, 283–298.

Terleev, A.A., Postnikov, A.A., Tokarev, D.A., Sosnovskaya, O. V., Bagmet, G.N., 2011. *Cloudina-Namacalathus-Korilophyton* association in the Vendian of the Altay-Sayan Foldbelt (Siberia). Neoproterozoic Sediment. Basins Stratigr. Geodyn. Pet. potential. Proc. Int. Conf. (Novosibirsk, 30 July - 02 August 2011) 96–98.

Tkachenko, V.I., Ushatinskaya, G.T., Zhuravlev, A.Y., Repina, L.N., 1987. Cambrian strata of the Kolyma Uplift. Izv. Akad. Nauk SSSR, Ser. Geol. 8, 55–62.

Uhlein, G.J., Uhlein, A., Periera, E., Caxito, F.A., Okubo, J., Warren, L. V., Sial, A.N., 2019. Ediacaran paleoenvironmental changes recorded in the mixed carbonate-siliciclastic Bambuí Basin, Brazil. Palaeogeogr. Palaeoclimatol. Palaeoecol. 517, 39–51.

Veizer, J., Compston, W., 1976. ^{87}Sr/^{86}Sr in Precambrian carbonates as an index of crustal evolution. Geochim. Cosmochim. Acta 40, 905–914.

Veizer, J., Hoefs, J., 1976. The nature of ^{18}O/^{16}O and ^{13}C/^{12}C secular trends in sedimentary carbonate rocks. Geochim. Cosmochim. Acta 40, 1387–1395.

Veizer, J., Holser, W.T., Wilgus, C.K., 1980. Correlation of ^{13}C/^{12}C and ^{34}S/^{32}S secular variations. Geochim. Cosmochim. Acta 44, 579–587.

Vernhet, E., 2007. Paleobathymetric influence on the development of the late Ediacaran Yangtze platform (Hubei, Hunan, and Guizhou provinces, China). Sediment. Geol. 197, 29–46.

Vidal, G., Palacios, T., Gámez-Vintaned, J.A., Díez Balda, M.A., Grant, S.W.F., 1994. Neoproterozoic-early Cambrian geology and palaeontology of Iberia. Geol. Mag. 131, 729–765.

Vishnevskaya, I.A., Kochnev, B.B., Letnikova, E.F., Kiseleva, V.Y., Pisareva, N.I., 2013. Sr isotope signatures in the Vendian Khorbusuonka Group of the Olenek Uplift (northeastern Siberian Platform). Dokl. Earth Sci. 449, 298–302.

Vishnevskaya, I.A., Letnikova, E.F., Vetrova, N.I., Kochnev, B.B., Dil, S.I., 2017. Chemostratigraphy and detrital zircon geochronology of the Neoproterozoic Khorbusuonka Group, Olenek Uplift, Northeastern Siberian platform. Gondwana Res. 51, 255–271.

Voronin, Y.I., Voronova, L.G., Grigorieva, N. V., Drozdova, N.A., Zhegallo, E.A., Zhuravlev, A.Y., Ragozina, A.L., Rozanov, A.Y., Sayutina, T.A., Sysoiev, V.A., Fonin, V.D., 1982. [The Precambrian-Cambrian boundary in the geosynclinal areas (Salaany Gol reference section, MPR)]. Sovmest. Sov.-Mongol. Paleontol. Ekspeditsiya, Trans. 18, 1–150.

Voronova, L.G., Drozdova, N.A., Esakova, N. V., Zhegallo, E.A., Zhuravlev, A.Y., Rozanov, A.Y., Sayutina, T.A., Ushatinskaya, G.T., 1987. [Lower Cambrian fossils of the Mackenzie Mountains (Canada)]. Paleontol. Institut, Akad. Nauk SSSR, Trans. 224, 1–88.

Wan, B., Xiao, S., Yuan, X., Chen, Z., Pang, K., Tang, Q., Guan, C., Maisano, J.A., 2014. *Orbisiana linearis* from the early Ediacaran Lantian Formation of South China and its taphonomic and ecological implications. Precambrian Res. 255, 266–275.

Wang, W., Guan, C., Zhou, C., Peng, Y., Pratt, L.M., Chen, X., Chen, L., Chen, Z., Yuan, X., Xiao, S., 2017. Integrated carbon, sulfur, and nitrogen isotope chemostratigraphy of the Ediacaran Lantian Formation in South China: Spatial gradient, ocean redox oscillation, and fossil distribution. Geobiology 15, 552–571. https://doi.org/10.1111/gbi.12226

Wang, W., Zhou, C., Guan, C., Yuan, X., Chen, Z., Wan, B., 2014. An integrated carbon, oxygen, and strontium isotopic studies of the Lantian Formation in South China with implications for the Shuram anomaly. Chem. Geol. 373, 10–26. https://doi.org/10.1016/j.chemgeo.2014.02.023

Warren, L.V., Buatois, L., Mangano, M.G., Simões, M.G., Santos, M.G.M., Poiré, D., Riccomini, C., Assine, M.L., 2020. Microbially induced pseudotraces from a Pantanal soda lake, Brazil: Alternative interpretations for Ediacaran simple trails and their limits. Geology 48, G472341.

Warren, L.V., Tohver, E., Inglez, L., Okubo, J., Riccomini, C., Xiao, S., 2019. Calibrating the Ediacaran-Cambrian transition in the SW Gondwana. Estud. Geol. 75, e118.

Warren, L.V., Fairchild, T.R., Gaucher, C., Boggiani, P.C., Poiré, D.G., Anelli, L.E., Inchausti, J.C.G., 2011. *Corumbella* and in situ *Cloudina* in association with thrombolites in the Ediacaran Itapucumi Group, Paraguay. Terra Nov. 23, 382–389. https://doi.org/10.1111/j.1365-3121.2011.01023.x

Warren, L.V., Quaglio, F., Simões, M.G., Gaucher, C., Riccomini, C., Poiré, D.G., Freitas, B.T., Boggiani, P.C., Sial, A.N., 2017. *Cloudina-Corumbella-Namacalathus* association from the Itapucumi Group, Paraguay: increasing ecosystem complexity and tiering at the end of the Ediacaran. Precambrian Res. 298, 79–87.

Weaver, P.G., McMenamin, M.A.S., Tacker, R.C., 2006. Paleoenvironmental and paleobiogeographic implications of a new Ediacaran body fossil from the Neoproterozoic Carolina Terrane, Stanly County, North Carolina. Precambrian Res. 150, 123–135.

Weber, B., Steiner, M., Zhu, M.Y., 2007. Precambrian-Cambrian trace fossils from the Yangtze Platform (South China) and the early evolution of bilaterian lifestyles. Palaeogeogr. Palaeoclimatol. Palaeoecol. 254, 328–349. https://doi.org/10.1016/j.palaeo.2007.03.021

Williams, M., Rushton, A.W.A., Cook, A.F., Zalasiewicz, J., Martin, A.P., Condon, D.J., Winrow, P., 2013. Dating the Cambrian Purley Shale Formation, Midland Microcraton, England. Geol. Mag. 150, 937–944.

Wilson, J.P., Grotzinger, J.P., Fischer, W.W., Hand, K.P., Jensen, S., Knoll, A.H., Abelson, J., Metz, J.M., McLoughlin, N., Cohen, P.A., Tice, M.M., 2012. Deep-water incised valley deposits at the Ediacaran – Cambrian boundary in southern Namibia contain abundant *Treptichnus pedum*. Palaios 27, 252–273.

Wood, R., Curtis, A., 2015. Extensive metazoan reefs from the Ediacaran Nama Group, Namibia: The rise of benthic suspension feeding. Geobiology 13, 112–122. https://doi.org/10.1111/gbi.12122

Wood, R., Curtis, A., Penny, A., Zhuravlev, A.Y., Curtis-Walcott, S., Iipinge, S., Bowyer, F., 2017. Flexible and responsive growth strategy of the Ediacaran skeletal metazoan *Cloudina* from the Nama Group, Namibia. Geology 45, 259–262.

Wood, R.A., Liu, A.G., Bowyer, F.T., Wilby, P.R., Dunn, F.S., Kenchington, C.G., Hoyal Cuthill, J.F., Mitchell, E.G., Penny, A.M., 2019. Integrated records of environmental change and evolution challenge the Cambrian Explosion. Nat. Ecol. Evol. 3, 528–538.

Wood, R.A., Poulton, S.W., Prave, A.R., Hoffmann, K.-H., Clarkson, M.O., Guilbaud, R., Lyne, J.W., Tostevin, R., Bowyer, F., Penny, A.M., Curtis, A., Kasemann, S.A., 2015. Dynamic redox conditions control late Ediacaran metazoan ecosystems in the Nama Group, Namibia. Precambrian Res. 261, 252–271. https://doi.org/10.1016/j.precamres.2015.02.004

Xiao, S., Chen, Z., Pang, K., Zhou, C., Yuan, X., 2020. The Shibantan Lagerstätte: insights into the Proterozoic-Phanerozoic transition. J. Geol. Soc. London. 178.

Xiao, S.H., Narbonne, G.M., 2020. The Ediacaran Period, in: Gradstein, F.M., Ogg, J.G., Schmitz, M.D., Ogg, G.M. (Eds.), Geological Time Scale 2020. Elsevier B.V., pp. 521–561.

Yang, A., Zhu, M., Zhuravlev, A.Y., Yuan, K., Zhang, J., Chen, Y., 2016. Archaeocyathan zonation of the Yangtze Platform: implications for regional and global correlation of lower Cambrian stages. Geol. Mag. 153, 388–409.

Yang, B., Steiner, M., Li, G., Keupp, H., 2014. Terreneuvian small shelly faunas of East Yunnan (South China) and their biostratigraphic implications. Palaeogeogr. Palaeoclimatol. Palaeoecol. 398, 28–58. https://doi.org/10.1016/j.palaeo.2013.07.003

Yang, B., Steiner, M., Schiffbauer, J.D., Selly, T., Wu, X., Zhang, C., Liu, P., 2020. Ultrastructure of Ediacaran cloudinids suggests diverse taphonomic histories and affinities with non-biomineralized annelids. Sci. Rep. 10, 1–12.

Yang, B., Steiner, M., Zhu, M., Li, G., Liu, J., Liu, P., 2016. Transitional Ediacaran–Cambrian small skeletal fossil assemblages from South China and Kazakhstan: Implications for chronostratigraphy and metazoan evolution. Precambrian Res. 285, 202–215.

Yang, C., Li, X.-H., Zhu, M., Condon, D.J., 2017. SIMS U–Pb zircon geochronological constraints on upper Ediacaran stratigraphic correlations, South China. Geol. Mag. 154, 1202–1216.

Yang, C., Li, X., Zhu, M., Condon, D.J., Chen, J., 2018. Geochronological constraint on the Cambrian Chengjiang biota, South China. Geol. Soc. London 175, 659–666.

Yang, C., Rooney, A.D., Condon, D.J., Li, X.-H., Grazhdankin, D. V., Bowyer, F.T., Hu, C., Macdonaldn, F., Zhu, M., 2021. The tempo of Ediacaran evolution. Sci. Adv. 7, eabi9643.

Yuan, X., Chen, Z., Xiao, S., Zhou, C., Hua, H., 2011. An early Ediacaran assemblage of macroscopic and morphologically differentiated eukaryotes. Nature 470, 390–393.

Zhang, W.-T., Babcock, L.E., Xiang, L.-W., Sun, W.-G., Luo, H.-L., Jiang, Z.-W., 2001. Lower Cambrian stratigraphy of Chengjiang, eastern Yunnan, China with special notes on Chinese *Parabadiella*, Moroccan *Abadiella* and Australian *Abadiella huoi*. Acta Palaeontol. Sin. 40, 294–309.

Zhang, Y., Du, Y., Xu, Y., Yu, W., Huang, H., Jiao, L., 2015. Geochemical characteristics of siliceous rocks during the transition from Sinian (Ediacaran) to Cambrian in central Hunan and its implication from genesis and sedimentary environment. Geol. Rev. 61, 499–510.

Zhang, Y., Yang, T., Hohl, S. V., Zhu, B., T., H., Pan, W., Chen, Y., Yao, X., Jiang, S., 2020. Seawater carbon and strontium isotope variations through the late Ediacaran to late Cambrian in the Tarim Basin. Precambrian Res. 345, 105769.

Zhou, C., Huyskens, M.H., Lang, X., Xiao, S., Yin, Q.Z., 2019. Calibrating the terminations of Cryogenian global glaciations. Geology 47, 251–254. https://doi.org/10.1130/G45719.1

Zhou, C., Li, H.-X., Xiao, S., Lan, Z., Ouyang, Q., Guan, C., Chen, Z., 2017a. A new SIMS zircon U–Pb date from the Ediacaran Doushantuo Formation: age constraint on the Weng'an biota. Geol. Mag. 154, 1193–1201. https://doi.org/10.1017/S0016756816001175

Zhou, C., Xiao, S., Wang, W., Guan, C., Ouyang, Q., Chen, Z., 2017b. The stratigraphic complexity of the middle Ediacaran carbon isotopic record in the Yangtze Gorges area, South China, and its implications for the age and chemostratigraphic significance of the Shuram excursion. Precambrian Res. 288, 23–38. https://doi.org/10.1016/j.precamres.2016.11.007

Zhou, M., Luo, T., Huff, W.D., Yang, Z., Zhou, G., Gan, T., Yang, H., Zhang, D., 2018. Timing the termination of the Doushantuo negative carbon isotope excursion: evidence from U-Pb ages from the Dengying and Liuchapo formations, South China. Sci. Bull. 63, 1431–1438.

Zhu, M., Lu, M., Zhang, J., Zhao, F., Li, G., Aihua, Y., Zhao, X., Zhao, M., 2013. Carbon isotope chemostratigraphy and sedimentary facies evolution of the Ediacaran Doushantuo Formation in western Hubei, South China. Precambrian Res. 225, 7–28. https://doi.org/10.1016/j.precamres.2011.07.019

Zhu, M., Zhang, J., Yang, A., 2007. Integrated Ediacaran (Sinian) chronostratigraphy of South China. Palaeogeogr. Palaeoclimatol. Palaeoecol. 254, 7–61.

https://doi.org/10.1016/j.palaeo.2007.03.025

Zhu, M., Zhuravlev, A.Y., Wood, R.A., Zhao, F., Sukhov, S.S., 2017. A deep root for the Cambrian explosion: Implications of new bio- and chemostratigraphy from the Siberian Platform. Geology 45, 459–462.

Zhu, M.Y., Li, G.X., Zhang, J.M., Steiner, M., Qian, Y., Jiang, Z.W., 2001. Early Cambrian stratigraphy of East Yunnan, Southwestern China: A synthesis. Acta Palaeontol. Sin. 40, 4–39.

Zhuravlev, A.Y., 1998. Early Cambrian archaeocyathan assemblages of Mongolia. Lund Publ. Geol. 142, 24–25.

Zhuravlev, A.Y., Gámez Vintaned, J.A., Ivantsov, A.Y., 2009. First finds of problematic Ediacaran fossil *Gaojiashania* in Siberia and its origin. Geol. Mag. 146, 775–780.

Zhuravlev, A.Y., Gravestock, D.I., 1994. Archaeocyaths from Yorke Peninsula, South Australia and archaeocyathan Early Cambrian zonation. Alcheringa 18, 1–54.

Zhuravlev, A.Y., Liñán, E., Gámez Vintaned, J.A., Debrenne, F., Fedorov, A.B., 2012. New finds of skeletal fossils in the terminal Neoproterozoic of the Siberian Platform and Spain. Acta Palaeontol. Pol. 57, 205–224.

Zhuravlev, A.Y., Naimark, E.B., 2005. Alpha, beta, or gamma: Numerical view on the Early Cambrian world. Palaeogeogr. Palaeoclimatol. Palaeoecol. 220, 207–225.

Zhuravleva, I.T., Konyaeva, I.A., Osadchaya, D. V., Boyarinov, A.S., 1997. Biostratigraphy of the Kiya River section. Early Cambrian archaeocyaths and spicular sponges from the Kiya River section (Kuznetsk Alatau). Ann. Paleontol. 83, 115–200.